

THE SPACE DENSITY, ENVIRONMENTS, AND PHYSICAL PROPERTIES
OF LARGE Ly α NEBULAE

by

Moire Kathleen Murphy Prescott

A Dissertation Submitted to the Faculty of the
DEPARTMENT OF ASTRONOMY
In Partial Fulfillment of the Requirements
For the Degree of
DOCTOR OF PHILOSOPHY
In the Graduate College
THE UNIVERSITY OF ARIZONA

2009

THE UNIVERSITY OF ARIZONA
GRADUATE COLLEGE

As members of the Dissertation Committee, we certify that we have read the dissertation prepared by Moire Kathleen Murphy Prescott entitled The Space Density, Environments, and Physical Properties of Large Ly α Nebulae and recommend that it be accepted as fulfilling the dissertation requirement for the Degree of Doctor of Philosophy.

_____ Date: 25 August 2009
Romeel Davé

_____ Date: 25 August 2009
Arjun Dey

_____ Date: 25 August 2009
Chris Impey

_____ Date: 25 August 2009
Rodger Thompson

_____ Date: 25 August 2009
Richard Green

Final approval and acceptance of this dissertation is contingent upon the candidate's submission of the final copies of the dissertation to the Graduate College.

I hereby certify that I have read this dissertation prepared under my direction and recommend that it be accepted as fulfilling the dissertation requirement.

_____ Date: 25 August 2009
Dissertation Director: Romeel Davé

_____ Date: 25 August 2009
Dissertation Director: Arjun Dey

STATEMENT BY AUTHOR

This dissertation has been submitted in partial fulfillment of requirements for an advanced degree at The University of Arizona and is deposited in the University Library to be made available to borrowers under rules of the Library.

Brief quotations from this dissertation are allowable without special permission, provided that accurate acknowledgment of source is made. Requests for permission for extended quotation from or reproduction of this manuscript in whole or in part may be granted by the head of the major department or the Dean of the Graduate College when in his or her judgment the proposed use of the material is in the interests of scholarship. In all other instances, however, permission must be obtained from the author.

SIGNED: Moire Kathleen Murphy Prescott

ACKNOWLEDGMENTS

I wish to acknowledge first and foremost my advisor Arjun Dey for his infectious enthusiasm and the endless opportunities. I also want to thank my Tucson collaborators Buell Jannuzi and Naveen Reddy, my previous advisors Rob Kennicutt, Chris Impey, and Eric Wilcots, and those who have supported me as part of my thesis committee: Christy Tremonti, Romeel Davé, Mark Dickinson, Richard Green, and Rodger Thompson. I am grateful for the financial support provided by an NSF Graduate Fellowship, a P.E.O. Scholar Award, and HST Grant GO10591. Many thanks to Michelle Cournoyer, Erin Carlson, Catalina Diaz-Silva, and all the staff at Steward and NOAO who have skillfully guided me through bureaucratic mazes time and time again. A heartfelt *arigato gozaimasu* to Nobunari Kaskikawa and Yuichi Matsuda for hospitality I will never be able to adequately repay. Thanks to the staff and telescope operators at the MMT, Kitt Peak, Keck, Gemini, and Subaru Observatories for their commitment and hard work running these facilities. I have great respect for the cultural significance of Kitt Peak to the Tohono O’odham Nation and the summit of Mauna Kea to the indigenous Hawaiian community, and I am enormously grateful to have been given the opportunity to conduct observations from these mountains.

The friends I have made in Tucson have kept me sane and kept me going. Thanks to Chien Peng for the thesis monkey, Janice Lee for her wisdom, Christy Tremonti for being a role model to so many of us, Andy Marble the inspirational A⁺ astronomer dad, Karen Knierman and Jackie Monkewicz for their courage, and Jane Rigby and Andrea Leistra for being older and wiser grad students we’d turn to for advice. I will miss all the people I got to know here in Tucson, including Lei Bai, Beth Biller, Shane Bussman, Steph Cortes, Jenn Donley, Kris Eriksen, Pablo Espinoza, Julia Greissl, Abby Hedden, Joannah Hinz, Steph Juneau, Jenna Kloosterman, Wilson Liu, John Moustakas, Joan Najita, Sabrina Pakzad, Kyle Penner, Wayne Schlingman, Suresh Sivanandam, Hee-Jong Seo, Amy Stutz, Krystal Tyler, Paula White, Lei Xu, Ben Weiner, Ken Wong, Yujin Yang, Patrick Young, and the Women’s Science Forum. A special word of thanks to Kate Brutlag, Amanda Ford, Megan Reiter, and Johanna Teske for making Steward a better and more supportive place. Thanks to Michael Mueller, Sasha Kuchuk, and Rob Dietz for the foreign language fun and the Murder Mysteries.

Grad school quite simply would not have been the same without Eric Nielsen, who kept me informed, entertained, Animated, Housed, and Battlestarred. Plus who could forget that stuff we did with those people that one time.

Finally, to Iva Momcheva, my roommate from day one, and Kristian Finlator, my partner in all things — thanks for all the support, the cupcakes, the bread-baking, the skiing, and the fun.

DEDICATION

This thesis is dedicated

To my parents, Elizabeth and Richard, who gave me a childhood full of the love of learning and a powerful belief in kindness, honesty, equality, and compassion, and who inspired in me the strength and determination to never let shyness hold me back.

To my sisters, Liana and Sarah, who are as dear to me as sisters ever could be and who inspire me every day with their thoughtfulness, humor, curiosity, and resilience.

To Grammy and Grampa Murphy, Grandmom and Grandad Prescott who continue to teach me about resourcefulness, hard work, and courage.

To my Aunt Karen, who as a child wished she could look through her grandfather's telescope with her brothers rather than do the dishes, and rightfully so.

To my entire family, for all the interest, the support, and the questions about "blobs" and " $\text{Ly}\alpha$ bodies."

To Ray LaPoint, Art Camosy, and all the wonderful teachers I had in the Madison Metropolitan School District who made me want to make them proud.

To Henrietta Swan Leavitt, Cecilia Payne-Gaposchkin, Annie Jump Cannon, and Maria Mitchell for steadfastly being themselves.

And to Kristian, my partner in all things, my cheering section, my best friend, and the love of my life, who is the only one who truly knows the joys and the tears that went into this thesis. We did it, my friend.

TABLE OF CONTENTS

LIST OF FIGURES	9
LIST OF TABLES	11
ABSTRACT	12
CHAPTER 1 INTRODUCTION	14
1.1 Tracing Galaxy Evolution	14
1.2 The Power and the Perils of $\text{Ly}\alpha$ Emission	16
1.3 The History of $\text{Ly}\alpha$ Surveys	19
1.4 $\text{Ly}\alpha$ and Massive Galaxy Formation	20
1.5 $\text{Ly}\alpha$ Nebulae	22
1.6 The Work of this Thesis	27
CHAPTER 2 A SYSTEMATIC SEARCH FOR LARGE $\text{Ly}\alpha$ NEBULAE IN THE NOAO	
DEEP WIDE-FIELD SURVEY BOÖTES FIELD	28
2.1 Introduction	29
2.2 Search Design	31
2.2.1 NDWFS Broad-band Data	33
2.2.2 The Search Algorithm	33
2.2.3 Candidate Sample	37
2.2.4 Potential Contaminants	47
2.3 Spectroscopic Follow-up	51
2.3.1 Observations & Reductions	51
2.4 Individual Sources	55
2.4.1 Confirmed $\text{Ly}\alpha$ Sources	57
2.4.2 PRG1 — “The $\text{Ly}\alpha$ +HeII Blob”	57
2.4.3 PRG2 — “The Diamond Blob”	59
2.4.4 PRG3 — “The Horseshoe Blob”	59
2.4.5 PRG4	63
2.4.6 LABd05	63
2.4.7 Survey Contaminants	63
2.5 The Selection Function	67
2.5.1 The Simulations	68
2.5.2 Angular Size and B_W Surface Brightness Selection Function	69
2.5.3 Redshift Selection Function	70
2.5.4 Known $\text{Ly}\alpha$ Nebulae as Test Cases	73
2.6 Results	83
2.6.1 The Space Density of Large $\text{Ly}\alpha$ Nebulae	83

TABLE OF CONTENTS — *Continued*

2.6.2	Sources of Uncertainty	84
2.7	Discussion	85
2.7.1	A Broad-band Ly α Nebula Survey	85
2.7.2	Comparisons to Other Surveys	86
2.7.3	Host Dark Matter Halos	90
2.8	Conclusions	92
CHAPTER 3 THE OVERDENSE ENVIRONMENT OF A LARGE Ly α NEBULA AT $z \approx 2.7$		
	$z \approx 2.7$	93
3.1	Introduction	93
3.2	Observations & Reductions	96
3.3	Ly α -Emitting Galaxy Candidate Selection	97
3.4	Results & Discussion	103
3.5	Conclusions	106
CHAPTER 4 DISSECTING A LARGE Ly α NEBULA AT $z \approx 2.7$		
4.1	Introduction	107
4.2	Observations & Reductions	110
4.2.1	HST ACS Data	112
4.2.2	HST NICMOS Data	113
4.2.3	Image Registration	114
4.3	The Components of the Nebula	114
4.3.1	Compact Sources	115
4.3.2	Diffuse Ly α Emission	116
4.3.3	Diffuse He II Emission	122
4.3.4	Diffuse Continuum Emission	125
4.4	Discussion	125
4.4.1	The Location of the Obscured AGN	125
4.4.2	Sources of Ionization	126
4.4.3	The Energy Budget of LABd05	128
4.5	Conclusions	130
CHAPTER 5 THE DISCOVERY OF A LARGE Ly α +HeII NEBULA AT $z \approx 1.67$: A CANDIDATE LOW METALLICITY REGION?		
5.1	Introduction	132
5.2	Observations & Reductions	135
5.2.1	The Search	135
5.2.2	Spectroscopic Follow-up	137

TABLE OF CONTENTS — *Continued*

5.3	Results	139
5.3.1	Ly α and He II Emission	139
5.3.2	C IV, C III], and Ne IV] Emission	145
5.4	Discussion	151
5.4.1	Physical Properties of the Nebula	151
5.4.2	Photoionization Modeling	155
5.4.3	Metallicity of the Gas	157
5.4.4	Source of Ionization	160
5.5	Implications	171
5.6	Conclusions	172
CHAPTER 6 CONCLUSIONS AND FUTURE DIRECTIONS		174
6.1	The Space Density of Large Ly α Nebulae	174
6.2	The Environments of Large Ly α Nebulae	177
6.3	The Anatomy of Large Ly α Nebulae	178
6.4	The Physical Conditions within Large Ly α Nebulae	181
6.5	Ly α Nebulae and Galaxy Formation	183
A WAVELET DECOMPOSITION		184
REFERENCES		186

LIST OF FIGURES

2.1	A Large $\text{Ly}\alpha$ Nebula Found with Broad-band Data.	32
2.2	Systematic Broad-band Search for Finding $\text{Ly}\alpha$ Nebulae.	38
2.3	Systematic Broad-band Search for Finding $\text{Ly}\alpha$ Nebulae.	39
2.4	Wavelet Decomposition Step of the Broad-band $\text{Ly}\alpha$ Nebula Search.	40
2.5	Expected $B_W - R$ Colors for $\text{Ly}\alpha$ Nebulae.	42
2.6	Expected $B_W - R$ Colors for $\text{Ly}\alpha$ Nebulae.	43
2.7	Size vs. $B_W - R$ of $\text{Ly}\alpha$ Nebula Candidates	49
2.8	Size vs. $B_W - R$ of $\text{Ly}\alpha$ Nebula Candidates	50
2.9	PRG1	60
2.10	PRG2	61
2.11	PRG3	62
2.12	PRG4	64
2.13	Dey et al. (2005) $\text{Ly}\alpha$ Nebula	65
2.14	$\text{Ly}\alpha$ Nebula Search Selection Function.	71
2.15	PRG1 Redshift Selection Function.	74
2.16	PRG2 Redshift Selection Function.	75
2.17	PRG3 Redshift Selection Function.	76
2.18	PRG4 Redshift Selection Function.	77
2.19	LABd05 Redshift Selection Function.	78
2.20	The Dependence of the Redshift Selection Function on Assumed Continuum Age.	79
2.21	$\text{Ly}\alpha$ Halo.	81
2.22	The Number Density of $\text{Ly}\alpha$ Nebulae.	88
3.1	$I4445 - B_W$ Color-Magnitude Diagram of Intermediate-Band Se- lected Sources.	99
3.2	$B_W - R$ vs. $R - I$ Color-Color Diagram of Line-Emitting Candidates.	100
3.3	Spatial Distribution of LAE Candidates in the Vicinity of A Large $\text{Ly}\alpha$ Nebula.	101
3.4	Radial Density Profile of LAE Candidates in the Vicinity of A Large $\text{Ly}\alpha$ Nebula.	102
4.1	Multiwavelength Imaging of a $\text{Ly}\alpha$ Nebula at $z \approx 2.7$	111
4.2	GALFIT Fit to V_{606} Data.	117
4.3	GALFIT Sizes and Morphologies of Galaxies Near a $\text{Ly}\alpha$ Nebula.	119
4.4	Compact Sources within LABd05	120
4.5	J-H vs. V-J color of compact sources.	121
4.6	$\text{Ly}\alpha$ Imaging of LABd05	123

LIST OF FIGURES — *Continued*

4.7	Ly α and HeII Imaging	124
5.1	Multiwavelength Images of a Ly α +HeII Nebula at $z \approx 1.67$	138
5.2	Night 1 Spectra of a Ly α +HeII Nebula at $z \approx 1.67$	140
5.3	Night 2 Spectra of a Ly α +HeII Nebula at $z \approx 1.67$	143
5.4	Ly α and HeII Spatial Profiles of a Ly α +HeII Nebula at $z \approx 1.67$. . .	146
5.5	Ly α and HeII Line Profiles of a Ly α +HeII Nebula at $z \approx 1.67$	147
5.6	Velocity and Velocity Dispersion Spatial Profiles of a Ly α +HeII Nebula at $z \approx 1.67$	148
5.7	Cloudy Line Ratio Predictions for a Ly α +HeII Nebula.	158

LIST OF TABLES

1.1	Large Ly α Nebulae	22
2.1	Ly α Nebula Candidates	45
2.1	Ly α Nebula Candidates	46
2.1	Ly α Nebula Candidates	48
2.2	Observing Log	53
2.3	Spectroscopic Observations	54
2.3	Spectroscopic Observations	56
2.4	Ly α Nebula Measurements	58
2.5	Other Known Ly α Nebulae in the Boötes Field	82
4.1	Multiwavelength Observations of a Large Ly α Nebula at $z \approx 2.656$	110
4.2	Astrometric Uncertainty	115
4.3	Compact Sources within a Large Ly α Nebula at $z \approx 2.656$	118
5.1	Spectroscopic Measurements of a Ly α +HeII Nebula at $z \approx 1.67$. .	141
5.2	Photometric Measurements of a Ly α +HeII Nebula at $z \approx 1.67$. . .	142
5.3	Emission Line Ratio Comparison	156

ABSTRACT

Powerful forces are at work in giant Ly α nebulae, a rare and mysterious population in the high redshift universe. Much like the spatially extended emission line halos around high redshift radio galaxies — but without the strong radio emission — Ly α nebulae (or Ly α ‘blobs’) boast copious Ly α emission (10^{44} erg s $^{-1}$), large sizes (~ 100 kpc), complex gas morphologies, and the company of numerous compact, star-forming galaxies, and may offer a window into dramatic episodes of massive galaxy formation. The small sample sizes and complex inner workings of Ly α nebulae have limited progress on understanding their space density, environments, and physical conditions. This thesis strives to answer fundamental questions about Ly α nebulae and pave the way for understanding their role in the build up of massive galaxy systems. To address the frequency of collapse of these massive structures, we carried out the largest systematic Ly α nebula survey to date and measured the Ly α nebula space density. As an unbiased test of the environment of Ly α nebulae, we studied the surroundings of a Ly α nebula and confirmed that Ly α nebulae reside preferentially in overdense regions. To disentangle the sources of ionization, we took a census of all the compact ionization sources within a large Ly α nebula using high resolution imaging. Finally, we used photoionization modeling to put constraints on the physical conditions, the metallicity, and the sources of ionization within Ly α nebulae. Future work will be able to build on this thesis by expanding the systematic search for Ly α nebulae to other existing deep broad-band datasets, mapping the three-dimensional overdense structures in which Ly α nebulae live out to ≥ 50 (comoving) Mpc scales, and disentangling multiple sources of ionization within

a larger sample of individual systems using deep optical and near-infrared spectroscopy and detailed photoionization modeling.

CHAPTER 1

INTRODUCTION

1.1 Tracing Galaxy Evolution

The discovery that spiral nebulae were in fact “island universes” of their own paved the way for addressing the origin of our own Milky Way (Curtis, 1917; Opik, 1922; Hubble, 1926, 1929). Much of the progress in observational extragalactic astronomy since that time has focused on using galaxies in different environments, of different properties, and from different epochs as snapshots of how galaxies evolved into the examples we see in the present day universe. After nearly a century of work, we have made great strides in building up a coherent picture of galaxy formation and the growth of structure ¹.

A crucial foundation for much of the progress on understanding the details of galaxy formation and evolution was the development of new techniques for identifying robust samples of galaxies and AGN at high redshift. The earliest efforts naturally focused on the brightest sources, as astronomers began identifying samples of quasars starting in the 1960’s (e.g., Schmidt, 1963). However, it took several decades before we gained a clear understanding for how the entire zoo of AGN phenomena related to one underlying physical model (the Unified Model of AGN; Antonucci, 1993, and references therein), and it wasn’t until recently that we had the capability to overcome the extreme luminosities of quasars in order to study the properties of their host galaxies (Boroson & Oke, 1982). Instead, the

¹In this sense we are doing much better than the sperm whale but have yet to achieve the wisdom of the pot of petunias (Adams, D. 1986, *The Hitchhiker’s Guide to the Galaxy* (U.S. audiocassette edition of the double LP adaptation ed.), Simon & Schuster Audioworks, ISBN 0-671-62964-6.)

first studies of high redshift galaxies focused on radio galaxies, ultimately understood to be part of the AGN family but one for which the AGN is obscured due to the inclination of the sources away from the line of sight. Thanks to strong radio emission from jets emanating from the central engine and the steep radio spectral energy distribution (SED), radio galaxies can be detected out to very high redshifts (McCarthy, 1993, and references therein). At the same time, it became clear that radio galaxies are a very massive and rare population, very far from representative of the typical galaxy at any redshift.

Finding normal galaxies over a range of redshifts and environments required improved technology and new selection techniques. The groundwork for galaxy selection based on continuum was laid in the late 1960's (Partridge & Peebles, 1967a,b). This method leverages the fact that galaxy continua can have strong spectral breaks in the UV continuum (e.g., the Lyman break, due to the stellar atmospheres of massive stars and absorption by neutral hydrogen in the interstellar medium) in order to select high redshift sources. After some initial unsuccessful surveys (Davis & Wilkinson, 1974; Partridge, 1974; Koo & Kron, 1980), it was not until the 1990's that the technique of selecting galaxies using broad-band colors that key off of the Lyman break began to mature (e.g., Guhathakurta et al., 1990; Steidel et al., 1995, 1996, for a review see Giavalisco 2002). Lyman break galaxy (LBG) surveys began to produce some of the first large samples of roughly L^* galaxies at $z \approx 3$, and continuum-selection techniques have since been applied to both lower and higher redshifts (e.g., Shimasaku et al., 2005; Henry et al., 2008; Reddy et al., 2008; Stark et al., 2009; Ly et al., 2009). Similar methods have used extreme galaxy colors to select well-defined galaxies samples, e.g., BzK galaxies and ERO selection based on looking for galaxies with very red colors consistent

with being passive or dusty galaxies at redshifts $z \approx 1.4 - 2.5$ (e.g., Elston et al., 1988; Daddi et al., 2004). Samples of galaxies selected using infrared and submillimeter data provide an additional window into populations of dust-obscured galaxies (e.g., Smail et al., 1997; Hughes & Dunlop, 1998; Dey et al., 2008).

It was also recognized early on that searching for star-forming galaxies via their strong emission lines (e.g., $\text{Ly}\alpha$) held the promise of finding lower mass, young, forming galaxies (e.g., Partridge & Peebles, 1967a,b). This approach was proposed at the same time as the continuum selection method but took longer to reach its full potential due to the faint fluxes involved, the complexities inherent in interpreting the $\text{Ly}\alpha$ emission line, and the limitations of observational technology.

1.2 The Power and the Perils of $\text{Ly}\alpha$ Emission

In the absence of dust and resonant scattering effects, $\text{Ly}\alpha$ should be the strongest emission line observed in the regions of ongoing star formation. In star-forming regions where the gas surrounding young, hot stars is heated to $\sim 10^4$ K, the resulting bubble of ionized H (i.e., HII region) emits a characteristic spectrum of H, O, and N emission lines. The relative ratio of the two most prominent H lines in the ultraviolet and optical — $\text{Ly}\alpha\lambda 1640$ ($H2 - 1$) and $\text{H}\alpha\lambda 6563$ ($H3 - 2$) — is predicted from quantum mechanics to be ~ 10 at temperatures of 10^4 K and densities of 100 cm^{-3} (Osterbrock, 1989). However, the fact that $\text{Ly}\alpha$ is a resonance line, produced by a transition into the ground state, has important consequences when predicting the observable $\text{Ly}\alpha$ emission in a cosmological setting. In regions of sufficient neutral H density, a $\text{Ly}\alpha$ photon will be continuously reabsorbed and reemitted as it tries to escape the system unless it scatters sufficiently in frequency

to shift it out of the core of the line. This *resonant scattering* combined with kinematic effects can dramatically alter the shape of the $\text{Ly}\alpha$ emission line profile (e.g., multiple asymmetric peaks; Verhamme et al., 2006; Dijkstra et al., 2006a,b).

The utility of $\text{Ly}\alpha$ as a tracer of star formation is compromised in actual cosmological sources by a number of additional factors. Since the $\text{Ly}\alpha$ emission line is in the far-ultraviolet, it is impossible to observe from the ground at $z \lesssim 1.7$ and is highly susceptible to absorption by dust. Assuming a Calzetti extinction curve and $E(B - V) = 0.3$, the extinction at $\text{Ly}\alpha$ is ~ 10 times that at $\text{H}\alpha$ (Calzetti et al., 1994). The unknown morphology of dust in high redshift galaxies poses an additional problem. In the case of a smooth dust screen, the susceptibility of $\text{Ly}\alpha$ to destruction by dust is heightened by the effects of resonant scattering, since with every scattering event, additional $\text{Ly}\alpha$ photons will be absorbed. On the other hand, a multi-phase interstellar medium (i.e., clumpy dust morphologies) may cause higher absorption of continuum photons, as continuum photons penetrate the dusty gas clouds while $\text{Ly}\alpha$ photons scatter off the surface. The net effect of the clumpy dust scenario is to boost the observed $\text{Ly}\alpha$ equivalent width (e.g., Neufeld, 1991; Hansen & Oh, 2006; Finkelstein et al., 2007, 2008). Studies of $\text{Ly}\alpha$ in the local universe have revealed an almost hopelessly complex situation in which the three best tracers of young star formation — ultraviolet continuum, $\text{H}\alpha$, and $\text{Ly}\alpha$ — show very different morphologies (e.g., Hayes et al., 2005, 2007). The $\text{Ly}\alpha$ escape does not consistently follow a simple relationship with dust content of the galaxy; instead, the kinematics of the surrounding interstellar medium (ISM) in many cases plays a more central role (Mas-Hesse et al., 2003; Atek et al., 2008, 2009). It has become clear that if the problem of using $\text{Ly}\alpha$ emission to understand star formation in the local universe is this unwieldy, the situation at

higher redshift must be even more uncertain.

Unlike $\text{Ly}\alpha$, $\text{H}\alpha$ is optically thin under normal conditions and unaffected by the complexities of resonant scattering. For this reason, $\text{H}\alpha$ became the tracer of choice for studying star formation in the local and low redshift universe (Kennicutt, 1998). An excellent tracer of young star formation, $\text{H}\alpha$ is also safely located at the red end of the optical range where it is much less susceptible to dust extinction and easily accessible by ground-based observations with photographic plates and optical CCDs. At higher redshift, however, using $\text{H}\alpha$ encounters observational problems of its own. Beyond $z \gtrsim 0.5$, $\text{H}\alpha$ is impossible to observe from the ground unless it falls within discrete atmospheric transmission windows in the near-infrared (J , H , and K). Observations in the infrared are subject to high sky backgrounds and less sensitive detector technology. While other Balmer and forbidden lines at shorter wavelengths (e.g., $[\text{OII}]\lambda 3727$, $\text{H}\beta\lambda 4861$, $[\text{OIII}]\lambda\lambda 4959, 5007$) are accessible in the optical range out to somewhat higher redshifts ($z \lesssim 1.0 - 1.7$), the weaker fluxes and the complications of metallicity, density, temperature, and stellar absorption make it challenging to use direct comparisons between star formation tracers measured at different redshifts (e.g., Kennicutt, 1998; Kewley et al., 2004; Moustakas et al., 2006).

At even higher redshifts ($z \gtrsim 1.7$ to 7) however, $\text{Ly}\alpha$ enters the optical window and is the only accessible strong emission line. Thus, despite the well-known complications, $\text{Ly}\alpha$ was quickly seized upon as a method for finding galaxies at high redshift, and according to early predictions, for specifically targeting the youngest, lowest mass galaxies in the process of forming.

1.3 The History of Ly α Surveys

In the 1960's Partridge & Peebles (1967a,b) predicted that star-forming galaxies could be identified at high redshifts using features in the far-UV spectral energy distribution — namely the Ly α emission line and the 912Å Lyman limit. After early attempts to use the continuum selection to find primeval galaxies using photoelectric photometry and photographic plates came up empty-handed (Davis & Wilkinson, 1974; Partridge, 1974), much of the efforts over the ensuing decade focused on searching for Ly α emission.

Ly α emission was successfully used first in the search for high redshift radio galaxies ($z \approx 1.5 - 1.8$; e.g., Spinrad et al., 1985; McCarthy, 1993, and references therein). Although these sources were initially found due to strong radio emission, the redshift identification required optical spectroscopy and at $z > 1.8$ was based on strong emission lines such as Ly α . This technique, as well as serendipitous discoveries, allowed astronomers to push out to redshifts beyond 5 (e.g., Dey et al., 1998; van Breugel et al., 1999; Stern & Spinrad, 1999, and references therein).

The first successful Ly α imaging surveys using narrow-band filters targeted fields around QSOs and in regions of known QSO absorbers, uncovering small samples of Ly α -emitting galaxies (e.g., Djorgovski et al., 1985; Schneider et al., 1986; Hu & Cowie, 1987; Steidel et al., 1991; Lowenthal et al., 1991). Many other surveys reported null results (e.g., Hu & Cowie, 1987; Lowenthal et al., 1990), however, making it clear that the technique was only sensitive to the most luminous Ly α -emitting galaxies. The advent of large format CCD imagers and 8-10m class telescopes in the 1990s and early 2000s has led to enormous progress in the last decade. Ly α surveys began to uncover samples of Ly α -emitting galaxies in

the field (e.g., Hu & McMahon, 1996; Cowie & Hu, 1998; Thommes et al., 1998; Hu et al., 1998; Malhotra & Rhoads, 2002; Rhoads et al., 2003). These surveys provide a means of selecting galaxies at fainter continuum luminosities and out to higher redshifts than are possible with continuum selection methods. Ly α -emitting galaxy sample sizes quickly evolved from handfuls to hundreds turning Ly α -emitting galaxy science from a curiosity into a full-fledged field. Ly α searches are now pushing the edge of known universe (e.g., Shimasaku et al., 2006; Dawson et al., 2007; Ouchi et al., 2008; Stark et al., 2009) and informing our understanding of galaxy formation on both low and high mass scales.

1.4 Ly α and Massive Galaxy Formation

While the significant attention has been paid to lower mass Ly α -emitting galaxies — due to the prospect of finding young, forming galaxies and putting observational constraints on reionization — the study of strong Ly α emission in the high redshift universe may also hold the key to studying the dramatic process of building up the most massive galaxies. Recent studies present strong evidence that the most massive galaxies were largely assembled by redshifts of $z \approx 1 - 2$ (e.g., McCarthy et al., 1987; Bundy et al., 2005; Daddi et al., 2005). In the 3 – 5 Gyr after the Big Bang, these galaxies built up the majority of their mass swiftly and dramatically before star formation was quenched most likely via feedback processes (e.g., due to supernovae or AGN). In the hierarchical picture of galaxy assembly, this calls to mind an extremely complex system of gaseous filaments and satellite galaxies that surround and perhaps fuel the growth of a central massive galaxy which in turn may produce outflows and shocks that impact the surrounding interstellar medium. The possibility of finding regions that can be used

as laboratories for studying ongoing galaxy formation is an enticing prospect but requires identifying these systems observationally.

Radio galaxies have been a target of intense study for the past several decades, driven by the idea that they are the progenitors of the most massive galaxies we see in the local universe. These massive sources are surrounded by satellite galaxies, produce powerful radio jets and X-ray emission, and in many cases exhibit spatially extended emission line halos, particularly in $\text{Ly}\alpha$ (e.g., Baum & Heckman, 1989; McCarthy, 1993; McCarthy et al., 1996; Pentericci et al., 1997; Reuland et al., 2003; Villar-Martín et al., 2003; Reuland et al., 2007; Villar-Martín, 2007; Hatch et al., 2008, 2009). The interpretation of these emission-line halos is far from simple. The kinematics suggest the presence of starburst superwinds in the center and infalling gas near the periphery (e.g., Zirm et al., 2005; Villar-Martín, 2007). Many of these emission line halos are polarized and aligned with the radio jet (the ‘alignment effect,’ e.g., Chambers & Miley, 1990; McCarthy, 1993; Pentericci et al., 1999; Miley & De Breuck, 2008, and references therein), which are likely explained via a combination of photoionization from the AGN and jet-induced star formation. All of this suggests that ionization is dominated by the central AGN and the complex interaction of the jet with the surrounding material, which complicates any attempts to understand the physics within these regions.

A few of the early successful $\text{Ly}\alpha$ surveys reported discoveries of large, diffuse nebulae of $\text{Ly}\alpha$ emission in radio-quiet regions. With the discovery of several more examples, these giant radio-quiet $\text{Ly}\alpha$ nebulae began to attract attention as a valuable window into the physics of massive galaxy formation perhaps caught at a different (earlier?) stage. Like the $\text{Ly}\alpha$ halos around radio galaxies, these $\text{Ly}\alpha$ nebulae are large (~ 100 kpc) with copious $\text{Ly}\alpha$ emission ($\sim 10^{44}$ erg s $^{-1}$) attesting

Table 1.1. Large Ly α Nebulae

Right Ascension (hours)	Declination (degrees)	Redshift	Ly α Luminosity (erg s $^{-1}$)	Ly α Diameter (kpc)	Reference
14:34:10.977	+33:17:30.87	2.656	1.7×10^{44}	160	Dey et al. (2005)
22:17:25.7	+00:12:49.6	3.09	1×10^{44}	130	Steidel et al. (2000)
22:17:39.0	+00:13:30.1	3.09	9×10^{43}	115	Steidel et al. (2000)
06:50:43.4	+41:29:13.8	2.672	—	110	Greve et al. (2007)
21:42:27.45	-44:20:28.69	2.38	3.5×10^{43}	100	Francis et al. (1996)
17:09:52.3	+59:13:21.72	2.83	2.1×10^{43}	95	Smith & Jarvis (2007)
03:32:14.6	-27:43:02.4	3.157	1.0×10^{43}	60	Nilsson et al. (2006)
02:17:43.35	-05:16:12.4	3.68	1.1×10^{43}	57	Saito et al. (2008)

to the presence of energetic phenomena. Ly α nebulae are often associated with multiple young, star-forming galaxies — Ly α -emitting galaxies (LAEs), Lyman break galaxies (LBGs), and submillimeter galaxies (SMGs) — and seem to reside preferentially in overdense environments (Francis et al., 1996; Keel et al., 1999; Steidel et al., 2000; Matsuda et al., 2004; Saito et al., 2006; Yang et al., 2009). For all the similarities, these radio-quiet Ly α nebulae lacked the powerful central radio galaxy and its accompanying jet. They therefore provide a potentially more accessible laboratory in which to look for evidence of ongoing galaxy formation. Table 1.1 lists some of the largest examples.

1.5 Ly α Nebulae

Radio-quiet Ly α nebulae were first discovered in narrow-band Ly α surveys of overdense regions, i.e., in the vicinity of quasars with substantial populations of

absorbers and in known galaxy overdensities. Francis et al. (1996) discovered a 100 kpc scale $\text{Ly}\alpha$ nebula at $z \approx 2.38$ in the field of a radio-quiet QSO and an absorber overdensity. Within the extended $\text{Ly}\alpha$ emission are a close pair of red compact galaxies, which the authors argued were likely young ellipticals in the process of merging (Francis et al., 2001). Keel et al. (1999) found three ~ 50 kpc $\text{Ly}\alpha$ nebulae that appeared to be powered by radio-quiet AGN within the field near a radio galaxy at $z \approx 2.39$. A pair of 100 kpc $\text{Ly}\alpha$ nebulae found in close proximity within a Lyman break galaxy redshift spike at $z \approx 3.1$ (Steidel et al., 2000). This discovery received much greater notice than the earlier discoveries in large part because this $\text{Ly}\alpha$ nebula pair at first appeared to show no sign of AGN activity or any red central compact source, which made them unique relative to the $\text{Ly}\alpha$ halos around radio galaxies and the other $\text{Ly}\alpha$ nebulae that had been found up to that point. A deep narrow-band follow-up study of the same field uncovered a sample of 35 $\text{Ly}\alpha$ nebulae in the region down to fainter luminosities and smaller sizes and measured the luminosity function of $\text{Ly}\alpha$ nebulae within overdense environments (Matsuda et al., 2004).

By this point, it was becoming clear that systematic $\text{Ly}\alpha$ nebula surveys were required in order to make unbiased measurements of the $\text{Ly}\alpha$ nebula space density. Saito et al. (2006) conducted a blank field survey using multiple narrow-band filters within the range $z \approx 3.25 - 4.95$. They found no luminous $\text{Ly}\alpha$ nebulae and constructed a luminosity function for the field that showed an order of magnitude lower in number density. A $\text{Ly}\alpha$ nebula was discovered in the GOODS-S field that showed no detection in any band other than the $\text{Ly}\alpha$ imaging (Nilsson et al., 2006). A wide-area survey for $\text{Ly}\alpha$ nebulae at $z \approx 2.83$ has so far reported one $\text{Ly}\alpha$ nebula, which again is argued to be without clear AGN signatures (Smith &

Jarvis, 2007; Smith et al., 2008).

The discovery of multiple $\text{Ly}\alpha$ nebulae with no sign of AGN activity spurred a number of theoretical papers postulating that these cases were fundamentally different from the AGN-dominated $\text{Ly}\alpha$ nebulae of Francis et al. (1996); Keel et al. (1999); Palunas et al. (2004) and exploring the possibility that $\text{Ly}\alpha$ nebulae are powered by starburst superwinds (Taniguchi & Shioya, 2000; Taniguchi et al., 2001; Ohyama et al., 2003; Mori et al., 2004). These authors argued that the observed sizes, luminosities, elongation, and linewidths could all result from supernovae-driven superwinds following a massive central starburst within a forming elliptical galaxy (Taniguchi & Shioya, 2000). They postulated that $\text{Ly}\alpha$ nebulae form part of an evolutionary sequence where the initial central starburst is hidden as a dusty submillimeter source until the superwind is able to begin clearing out the gas and dust, during which time the source is seen as an extended emission line nebula around the forming galaxy (Taniguchi & Shioya, 2000). They also argued that the discovery of submillimeter detections of $\text{Ly}\alpha$ nebulae was further confirmation of this theory, as the full SED most closely resembled Arp 220, a typical ultraluminous starburst galaxy, scaled up by a factor of 30 moving it into the hyperluminous regime (Taniguchi et al., 2001). The similarity between the bubble-like morphology seen in some $\text{Ly}\alpha$ nebulae (Matsuda et al., 2004) and the simulations of supernova-dominated primordial galaxies was cited as evidence of the superwind scenario (Mori et al., 2004).

Infall of gravitationally cooling gas was also proposed as an explanation for the $\text{Ly}\alpha$ nebulae (e.g., Loeb & Rybicki, 1999; Haiman et al., 2000). As pristine gas collapses along filaments and is heated via collisional excitation, the primary coolants will be $\text{Ly}\alpha$ and HeII emission (e.g., Fardal et al., 2001). Due to reso-

nant scattering of $\text{Ly}\alpha$, these cooling clouds should appear as large $\text{Ly}\alpha$ nebulae around a central growing galaxy (Fardal et al., 2001) and at high redshifts, may show measurable polarization (Rybicki & Loeb, 1999). Prior to the onset of star formation, gravitationally cooling clouds would be expected to show a high $\text{Ly}\alpha$ equivalent widths ($>1000\text{\AA}$; Dijkstra, 2009) due to the lack of stellar or AGN continuum, but this simple picture is complicated by the effects of the intergalactic medium (IGM). In reality, the high intrinsic $\text{Ly}\alpha$ equivalent widths otherwise indicative of gravitational cooling will be diminished due to $\text{Ly}\alpha$ scattering in the IGM (Dijkstra, 2009), and the $\text{Ly}\alpha$ line profiles expected from infall can be as complex as those predicted for the outflow scenario (Dijkstra et al., 2006a,b). Thus it is a challenge to unambiguously identify cases in which gravitational cooling is the dominant process.

Despite the initial evidence that these $\text{Ly}\alpha$ nebulae were not AGN-powered, subsequent study has produced a more complicated picture. Detailed follow-up of the $\text{Ly}\alpha$ nebula pair of Steidel et al. (2000) showed that one case had a strong, unresolved submillimeter counterpart ('Blob 1,' one of the most luminous submillimeter sources known; Chapman et al., 2001), while the other was only weakly detected ('Blob 2'). X-ray coverage of both $\text{Ly}\alpha$ nebulae showed that the weak submillimeter source contains a hard X-ray detection while the strong submillimeter source is undetected (Basu-Zych & Scharf, 2004). Thus, in 'Blob 2' the hard X-ray detection combined with excess $2\mu\text{m}$ emission points to an AGN (Geach et al., 2007). By contrast, 'Blob 1' shows no sign of an energetic AGN: there are no high ionization lines in the spectrum, no X-ray emission, and the weak radio emission is consistent with the local FIR-radio correlation (Chapman et al., 2004). The kinematics are difficult to interpret in these regions; observations

of the $\text{Ly}\alpha$ line profile in ‘Blob 1’ showed multiple components, potentially a sign of an outflowing shell (Ohyama et al., 2003; Wilman et al., 2005) or a result of gas infall (Dijkstra et al., 2006b). More recent observations showed that the source has optical and NIR colors consistent with a heavily obscured starburst; the non-detection of ‘Blob 1’ in high resolution submillimeter observations suggests that the starburst must be spatially extended (Matsuda et al., 2007).

The diversity seen in this pair of $\text{Ly}\alpha$ nebulae turns out to be representative of the entire class. The largest $\text{Ly}\alpha$ nebula studied by Francis et al. (1996, 2001) and Palunas et al. (2004) has two extremely red galaxies embedded within the nebula and shows C IV emission. This is suggestive of an AGN, but since strong UV continuum is not observed, an AGN would have to be highly obscured. A $\text{Ly}\alpha$ nebulae discovered in the GOODS-S field at $z \approx 3.16$ shows no other emission lines and is not detected in any other band, even in the deep GOODS dataset. For this reason, the authors argue against an AGN or a starburst scenario, and conclude that gravitational cooling is most likely. A similar argument is made in the case of a $\text{Ly}\alpha$ nebulae found at $z \approx 2.83$; Smith & Jarvis (2007) argue the lack of high ionization emission lines, $24\mu\text{m}$, and radio emission rules out an AGN, no matter the level of obscuration. They cannot rule out a starburst model, but say that the $\text{Ly}\alpha$ surface brightness profile is in good agreement with models for gravitational cooling radiation (Smith & Jarvis, 2007; Smith et al., 2008). A number of $\text{Ly}\alpha$ nebulae also show strong mid-infrared and submillimeter emission, and signs of merger activity (Dey et al., 2005; Colbert et al., 2006).

$\text{Ly}\alpha$ nebulae are highly energetic phenomena, and their rarity, their presence in a number of well-studied galaxy overdensities, and their close association with other star-forming galaxy populations all suggest that $\text{Ly}\alpha$ nebulae offer unique

insight into the formation of the most massive structures. To better understand how $\text{Ly}\alpha$ nebulae fit into the high redshift universe, we must answer to a number of fundamental questions. What is the space density of $\text{Ly}\alpha$ nebulae? In what environments does this phenomenon occur? Can we find evidence that $\text{Ly}\alpha$ nebulae are sites of ongoing galaxy formation by studying their local environment and energetics? What constraints can we put on the physical conditions (metallicity, source of ionization) within these regions?

1.6 The Work of this Thesis

In this thesis, I have focused on addressing these questions from an observational perspective. Chapter 2 presents an innovative systematic search for $\text{Ly}\alpha$ nebulae, the largest of its kind, and a measure of the space density of large $\text{Ly}\alpha$ nebulae at $z \approx 2 - 3$. In Chapter 3, I present unbiased confirmation of the idea that large $\text{Ly}\alpha$ nebulae live preferentially in overdense regions. A detailed census of the local neighborhood of a large $\text{Ly}\alpha$ nebula in Chapter 4 demonstrates the complexity characteristic of these regions of ongoing galaxy formation. Chapter 5 is a detailed look at the physical conditions — the metallicity and source of ionization — within a $\text{Ly}\alpha + \text{HeII}$ nebula. Chapter 6 presents the conclusions of this thesis and a discussion of future directions.

CHAPTER 2

A SYSTEMATIC SEARCH FOR LARGE $\text{Ly}\alpha$ NEBULAE IN THE NOAO DEEP
WIDE-FIELD SURVEY BOÖTES FIELD

Giant $\text{Ly}\alpha$ nebulae have attracted attention as potential sites of ongoing massive galaxy formation, but the rarity of these powerful sources has made it difficult to obtain an accurate measurement of their space density. Systematic narrow-band $\text{Ly}\alpha$ nebula surveys are ongoing, but the limited redshift range probed and the observational expense of this technique has limited the comoving volume probed by even the largest of these surveys and posed a significant hurdle to finding more examples of such rare sources. To measure the true space density of large $\text{Ly}\alpha$ nebulae, we have carried out a systematic search for large $\text{Ly}\alpha$ nebulae using the existing deep *broad-band* B_W imaging of the NOAO Deep Wide-Field Survey (NDWFS). The survey covers the entire 9 square degree Boötes field and is sensitive to diffuse, blue sources within the B_W bandpass, corresponding to a redshift range of $\Delta z \approx 1$ for sources with strong $\text{Ly}\alpha$ emission. The comoving volume of the survey is $\approx 1.4 \times 10^8 h_{70}^{-3} \text{ Mpc}^3$, making this the largest survey for $\text{Ly}\alpha$ nebulae ever undertaken. This innovative approach, complementary to the narrow-band techniques, allows us to efficiently search a very large comoving volume for the largest (B_W sizes of $> 37 \text{ kpc}$) and brightest (average B_W surface brightnesses of $26.5\text{-}27.8 \text{ mag arcsec}^2$) $\text{Ly}\alpha$ nebulae. Our survey recovered a previously-known case and discovered 4 new $\text{Ly}\alpha$ nebulae, including the first spatially extended $\text{Ly}\alpha\text{+HeII}$ nebula. This corresponds to a number density of $1.5 \times 10^{-7} h_{70}^3 \text{ Mpc}^{-3}$, the first strong lower limit on the space density of $\text{Ly}\alpha$ nebulae.

2.1 Introduction

The formation of the most massive galaxies was a swift and dramatic process. Recent evidence presents a clear picture that the most massive galaxies in the universe were largely formed by $z \approx 1 - 2$ after only 3-5 Gyr of cosmic history (e.g., McCarthy et al., 2004; van Dokkum et al., 2004; Daddi et al., 2005; Bundy et al., 2005; Brown et al., 2007). Within the hierarchical picture of galaxy assembly, we would expect the formation sites of massive galaxies to be incredibly complex places - with gaseous filaments and satellite galaxies surrounding and perhaps fueling the growth of a massive galaxy while outflows and shocks stir up the surrounding medium.

Radio galaxies have been the subject of intense study as the most unequivocal examples of massive galaxy progenitors. With masses of $10^{11} - 10^{12} M_{\odot}$, numerous satellite galaxies, and large halos of excited gas emitting strongly in $\text{Ly}\alpha$ and other emission lines, radio galaxies fit the image of a massive galaxy in formation (e.g., Miley & De Breuck, 2008; Hatch et al., 2009). However, the power of the central active galactic nucleus (AGN) and the complex interaction of the jet with its surroundings complicates the interpretation of the energetics within these regions.

Instead, giant radio-quiet $\text{Ly}\alpha$ nebulae discovered more recently have begun to attract attention as a valuable window into the physics of ongoing massive galaxy formation (e.g., Francis et al., 2001; Steidel et al., 2000; Palunas et al., 2004; Matsuda et al., 2004; Saito et al., 2006; Nilsson et al., 2006; Smith & Jarvis, 2007; Yang et al., 2009). Like the $\text{Ly}\alpha$ halos around radio galaxies, these $\text{Ly}\alpha$ nebulae can be as large as ~ 100 kpc across. The copious $\text{Ly}\alpha$ emission ($\sim 10^{44} \text{ erg s}^{-1}$) signals the presence of energetic phenomena and, as described in

Chapter 4, Ly α nebulae frequently are surrounded by or associated with young, star-forming galaxy populations — Ly α -emitting galaxies (LAEs), Lyman break galaxies (LBGs), and submillimeter galaxies (SMGs). Chapter 3 provides unbiased confirmation that Ly α nebulae reside in overdense environments, in agreement with other studies (Matsuda et al., 2004; Saito et al., 2006; Yang et al., 2009).

For all the excitement about these sources, Ly α nebulae are rare. Only about a dozen large ($\sim 50 - 100$ kpc) cases are known. The very rarity of Ly α nebulae has thus far hindered our ability to derive an accurate estimate of the most basic metric for understanding a given population - the space density. Ly α nebulae were first discovered in targeted studies of known overdensities, biasing the space density measurements (Matsuda et al., 2004). Subsequent systematic surveys using narrow-band imaging to survey wider and wider areas have uncovered a handful more (Nilsson et al., 2006; Smith & Jarvis, 2007; Saito et al., 2006; Yang et al., 2009). The most recent number density estimates ranging from $\sim 10^{-6} - 10^{-5} h_{70}^3 \text{ Mpc}^{-3}$ for $z \approx 2 - 6.5$ (Matsuda et al., 2004; Saito et al., 2006; Ouchi et al., 2009; Yang et al., 2009) to $< 5 \times 10^{-7} h_{70}^3 \text{ Mpc}^{-3}$ below $z \approx 1$ (Keel et al., 2009). The rarity of Ly α nebulae requires surveys that cover enormous comoving volumes, but the existing surveys have been fundamentally limited by the inherently expensive nature of narrow-band imaging. To address this issue, we have taken a complementary approach.

We have designed a systematic survey for Ly α nebulae based on the deep *broad-band* imaging of the NOAO Deep Wide-Field Survey (NDWFS; Jannuzi & Dey, 1999). While less sensitive to faint emission line fluxes, deep broad-band data of wide-area surveys can be used effectively to search for the brightest Ly α nebulae, particularly in the blue where the Ly α line enhances the broad-band flux

against the dark sky. Our search uncovered 5 $\text{Ly}\alpha$ nebulae within the ~ 9 square degree field, corresponding to a number density of $1.9 \pm 1.1 \times 10^{-7} h_{70}^3 \text{ Mpc}^{-3}$.

In Section 2.2 we discuss the survey design, and Section 2.3 presents the spectroscopic follow-up of $\text{Ly}\alpha$ nebula candidates. The 5 individual $\text{Ly}\alpha$ nebulae selected with our search are described in Section 2.4, and the simulations used to understand the selection function of our survey are presented in Section 2.5. We present the number density measurement in Section 2.6 and discuss the implications of our results in Section 2.7. We conclude in Section 2.8.

We assume the standard Λ CDM cosmology ($\Omega_M = 0.3$, $\Omega_\Lambda = 0.7$, $h = 0.7$); $1''$ corresponds to a physical scales of 8.5-7.6 kpc for redshifts of $z = 1.7 - 3.1$. All magnitudes are in the AB system.

2.2 Search Design

While most of the early examples of the $\text{Ly}\alpha$ nebula class were found via narrow-band surveys of known galaxy overdensities, one of the largest $\text{Ly}\alpha$ nebulae was discovered more recently through very different means (LABd05; Dey et al., 2005). This $\text{Ly}\alpha$ nebula came to light during a study of strong $24\mu\text{m}$ sources detected by the Spitzer Space Telescope in the Boötes field. Unlike the rest of the sample, this source had a diffuse, extended morphology and very blue colors in deep broad-band imaging (Figure 2.1). The authors suspected and spectroscopically confirmed that $\text{Ly}\alpha$ line emission was dominating the blue broad-band flux and that the diffuse morphology indicated the presence of a giant $\text{Ly}\alpha$ nebula.

Inspired by this discovery, we designed an innovative search for $\text{Ly}\alpha$ nebulae in deep broad-band imaging of the NOAO Deep Wide-Field Survey (NDWFS; Jannuzi & Dey, 1999). Our survey is geared towards finding the largest and

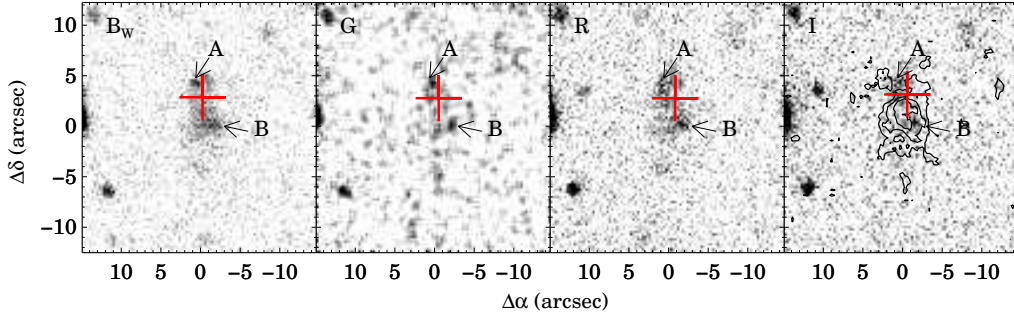


Figure 2.1 Images cutouts of the B_W , G , R , & I broad-band images of the $\text{Ly}\alpha$ nebula discovered at $z \approx 2.7$ by Dey et al. (2005). ‘A’ is a Lyman Break galaxy at the redshift of the nebula; B is a background galaxy. The red crosses in the 4 panels mark the positions of the mid-infrared source as measured from the *Spitzer* $24\mu\text{m}$ (on the B_W panel), $3.6\mu\text{m}$ (G), $4.5\mu\text{m}$ (R), and $8.0\mu\text{m}$ (I) images. The contours in the last panel show the central portion of the $\text{Ly}\alpha$ emission detected in a narrow-band filter. The contours drawn correspond to the line flux surface brightnesses of $[0.2, 0.4, 0.6, 0.8] \times 10^{-16} \text{ erg s}^{-1} \text{ cm}^{-2} \text{ arcsec}^{-2}$.

brightest Ly α nebulae, by leveraging the very deep imaging of NDWFS to look for sources where bright Ly α emission boosts the broad-band flux relative to the very dark sky in the blue. The wide-area of the NDWFS survey means we were able to probe an enormous comoving volume with an existing dataset, significantly reducing the required observational overhead. In that sense, our survey is complementary to the more sensitive but smaller volume narrow-band Ly α nebulae surveys (e.g., Matsuda et al., 2004; Saito et al., 2006; Smith & Jarvis, 2007; Yang et al., 2009).

In this section we describe our broad-band search algorithm and the resulting sample of 40 high priority (and 40 second priority) Ly α nebulae candidates.

2.2.1 NDWFS Broad-band Data

The deep broad-band optical data from the NOAO Deep Wide-Field Survey Boötes Field (NDWFS; Jannuzi & Dey, 1999) form the basis for this systematic survey for large Ly α nebulae. Observations in B_W , R , and I bands of the 9 square degree Boötes field were completed using the Mayall 4m Telescope and the MOSAIC imaging camera. Data reduction was performed using IRAF¹. The B_W , R , and I -band median 5σ point-source depths are ≈ 27.1 , 26.3, and 25.8 mag (AB), respectively. The Boötes field was chosen as a field with low IRAS 100 μ m and N(HI) background that would be at low airmass during the best observing conditions for Kitt Peak National Observatory.

2.2.2 The Search Algorithm

The survey was designed to select blue, diffuse, spatially-extended sources in the 27 pointings of the NDWFS Boötes field optical imaging. The B_W imaging

¹NDWFS Data Processing: <http://www.noao.edu/noao/noaodeep/ReductionOpt/frames.html>

was used as the primary search image, and the R imaging provided secondary color information. With nine square degrees to cover and an average 5σ limiting magnitude of 27.1 in B_W , our primary concern in designing the algorithm was to restrict the number of contaminant objects while retaining objects likely to be Ly α nebulae. Our search strategy involves first subtracting off bright galaxies and compact objects and then searching for diffuse, spatially extended, low surface brightness objects with blue colors.

The search pipeline steps are described below and shown as a flow chart in Figure 2.2. Figures 2.3 and 2.4 illustrate how the pipeline works using a sample image region. Prior to running the search pipeline, masked pixels originally set to large values in the archival NDWFS data were reset to the median sky value in the image to avoid ringing issues later in the algorithm. Each pointing was analyzed separately and was divided into nine sections (overlapping by $60''$) to speed the search process.

Background and Halo Subtraction

Step 1: The first step is to remove the sky background and the halos around bright stars using a background map generated by Source Extractor. We used a high detection threshold ($DETECT_THRESH = 10\sigma$ per pixel), set background parameters ($BACK_SIZE = 64$ and $BACK_FILTERSIZE = 3$), and required a minimum of 5 connected pixels ($MINAREA = 5$). This background map was subtracted from the search image.

Bright Object Removal

Step 2: First, we remove bright stars and galaxies that would produce a large number of false detections later on. We again ran Source Extractor using a high detection threshold ($DETECT_THRESH = 10\sigma$ per pixel) and a minimum of

5 connected pixels ($MINAREA = 5$) in order to generate a catalog of bright sources.

Step 3: We then ran Source Extractor with a very low threshold ($DETECT_THRESH = 1\sigma$ per pixel) in order to generate a deep segmentation map, i.e., a map of all object pixels, that would include pixels out into the faint wings of bright stars and galaxies. This iteration used the *ASSOC* mode in which the catalog from *Step 2* was used as an input to Source Extractor and only those detections that match were reported. Detected sources were matched against the input catalog based on measured pixel position, a weight set by the object flux ($FLUX_AUTO$), and a search radius ($ASSOC_RADIUS = 2$ pixels). Using the deep segmentation maps from this step and the image rms maps, we replace regions identified with bright objects (stars and galaxies) with patches of sky noise.

Step 4: We repeated *Step 2* running Source Extractor on the “cleaned” image from *Step 3* but with an intermediate threshold ($DETECT_THRESH = 6\sigma$ per pixel) to further remove stars and galaxies.

Step 5: We repeated *Step 3* running Source Extractor on the image from *Step 4* with the *ASSOC* feature in order to generate the necessary deep segmentation map. Again, the detections are replaced with sky noise.

Faint Compact Object Removal

Step 6: To remove fainter objects with compact morphology, we used *unsharp masking*. An unsharp masked image is produced by smoothing the image from *Step 5* using a 11×11 pixel kernel and then subtracting the smoothed image from the image from *Step 2*. In this process, diffuse emission is removed, so only compact sources remain in the unsharp masked image.

Step 7: We perform another *ASSOC* Source Extractor run on the unsharp

masked image in which we only allow matched detections to be returned, i.e., anything detected in both the *Step 5* image and the unsharp masked image is reported. We remove these object regions by replacing them with sky noise, and in this way remove additional faint compact sources from the image.

Final Image Cleaning

Step 8: To avoid artifacts from bright stars being selected as sources later in the pipeline, we replaced the regions around bright stars out a radius of 150 pixels with sky noise.

Identification of Spatially Extended Objects

Step 9: We then apply a wavelet decomposition algorithm to decompose the image into maps showing the power on a number of different spatial scales. We use the wavelet decomposition code *wvdecomp*² to filter the image across six size scales ($scalemin = 1$, $scalemax = 6$, $threshold = 3$, $thresholdmin = 2$, $iter = 10$). A more detailed discussion of the wavelet algorithm is given in Appendix A.

Step 10: We used the known Ly α nebula LABd05 to empirically determine the appropriate scale for large Ly α nebulae. Using one final run of SourceExtractor, we make a catalog of sources in the wavelet power map and select those with wavelet power peaks above 4σ , chosen to minimize the number of total candidates while preserving sources like LABd05.

Final Catalog Cleaning and Candidate Prioritization

Step 11: Sources drawn from high noise regions of the image as well as those found in regions that had been flagged in previous steps were removed from the candidate list.

²Alexey Vikhlinin; ZHTOOLS documentation and source code: <http://hea-www.harvard.edu/RDzhTools>.

Step 12: Postage stamps of candidates were inspected visually to remove artifacts and fake sources detected due to residual halos of stars and galaxies. The candidates are ranked by eye on a scale from 0 to 4, where 0 is a star halo, 1 is a galaxy halo, 2 is tidal tails or spiral arms, 3 is a tight grouping of compact sources selected as a single large source, and 4 is spatially-extended diffuse emission. We remove those objects categorized as 0-2 from the candidate sample, since these are easy to classify unambiguously by eye. Since the distinction between categories 3 and 4 is more subjective and since $\text{Ly}\alpha$ nebulae are known to show clumpy morphology in some cases, both category 3 and 4 objects were included in the final sample to be targeted for follow-up spectroscopy.

Step 13: The final sample was then prioritized based on $B_W - R$ color and size, as discussed in Section 2.2.3.

2.2.3 Candidate Sample

We used the search algorithm described in the previous section to morphologically select $\text{Ly}\alpha$ nebula candidates from the entire Boötes field dataset and in the final step use visual inspection to remove artifacts and tidal features from the sample. Since the objects we are looking for have strong $\text{Ly}\alpha$ emission, which at $1.9 < z < 2.9$ lies within the B_W bandpass, in principle we are looking for objects that are blue in $B_W - R$. However, unlike all other $\text{Ly}\alpha$ nebula surveys, our survey is not formally equivalent width limited. Figures 2.5 and 2.6 show the expected $B_W - R$ color for a source with a given redshift and $\text{Ly}\alpha$ equivalent width generated by adding a Gaussian emission line to unreddened single stellar population models of age 5 and 25 Myr (Bruzual & Charlot, 2003). Other than at the high redshift end of the survey ($z \gtrsim 2.6$), sources of any equivalent width will fall within our color selection window. The key factor is whether a source is spatially

Figure 2.2 Flow chart of the systematic broad-band search for Ly α nebulae in the NDWFS Boötes field.

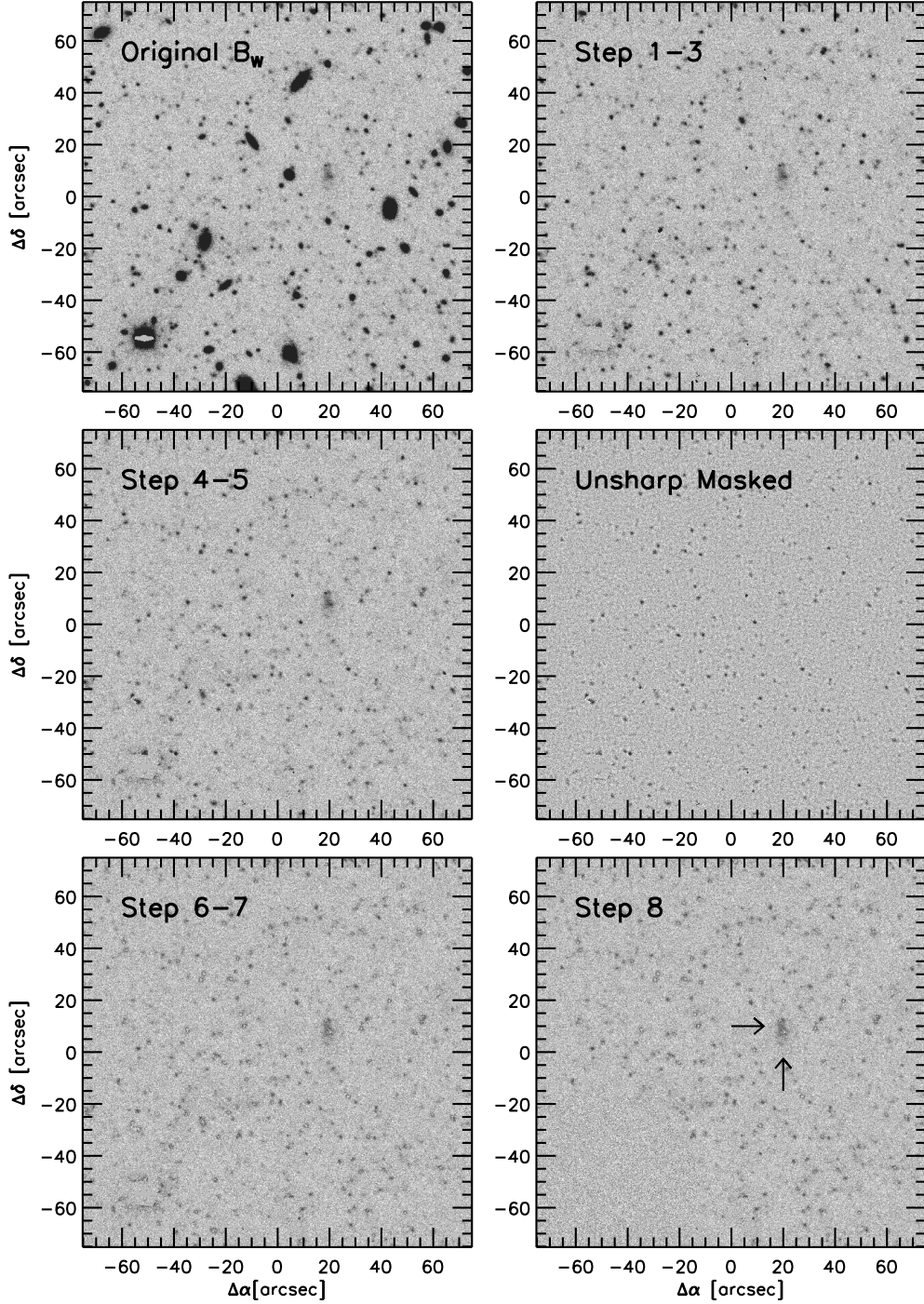


Figure 2.3 Steps of the broad-band $\text{Ly}\alpha$ nebula search algorithm illustrated using the region around the Dey et al. (2005) $\text{Ly}\alpha$ nebula (see text). The diffuse emission of the Dey et al. (2005) $\text{Ly}\alpha$ nebula is visible (arrows).

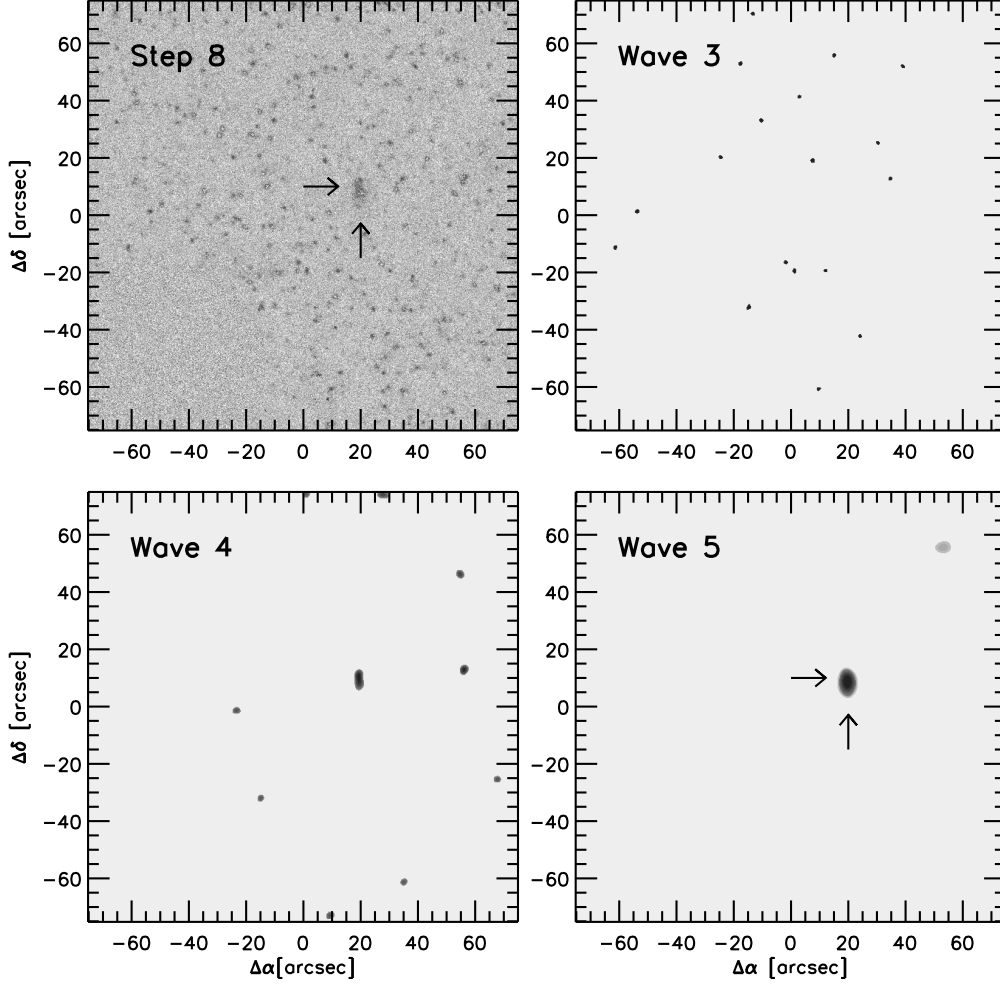


Figure 2.4 Wavelet decomposition is used to separate out sources of different size scales. The upper left panel shows the final result of Steps 1-8, an image with bright compact objects removed. The other three panels show the wavelet power maps for different size scales. The diffuse emission of the Dey et al. (2005) $\text{Ly}\alpha$ nebula generates a large wavelet power peak in the final panel and is easily selected as a $\text{Ly}\alpha$ nebula candidate (arrows). The other source in the upper right of the bottom right panel is below the 4σ threshold and is therefore too weak to be selected.

extended enough and bright enough in B_W to be selected via the morphological search pipeline.

Figure 2.7 shows the size and color distribution of the candidate sample. We measured $B_W - R$ colors in the original images using large apertures (30 pixel, $7.7''$ diameter; aperture sky subtraction). For the purposes of selecting candidates, we defined the size as that measured by Source Extractor (*ISOAREA_WORLD* in square degrees) in the final search on the wavelet power map. We stress that because these sizes are measured in the wavelet power map, they should not be taken as the true size of the object because the wavelet size is underestimated in cases where some portion of that object has been rejected during the pipeline (due to compact sources within or adjacent to the diffuse emission). In addition, it is also important to keep in mind that we are attempting to detect line emission within the broad B_W band, so the measured B_W sizes will underestimate the true nebular size.

The majority of the morphologically-selected candidates are red ($B_W - R \gtrsim 1.0$), but a small subset show blue colors, which could either result from a strong emission line within the B_W band or from very blue continuum emission. Due to the fact that we included both category 3 and 4 candidates (described in Section 2.2.2), the candidates span a range of morphologies from diffuse to clumpy. A number of the very blue sources appear to be a close grouping of compact sources selected as one. While at first glance these compact groups do not have the diffuse appearance we were looking for, we decided that it is unwise to remove them because the full range of morphological range spanned by the $\text{Ly}\alpha$ nebula class is not yet known. Indeed, as putative sites of massive galaxy formation, $\text{Ly}\alpha$ nebulae are sometimes found to encompass compact sources (e.g.,

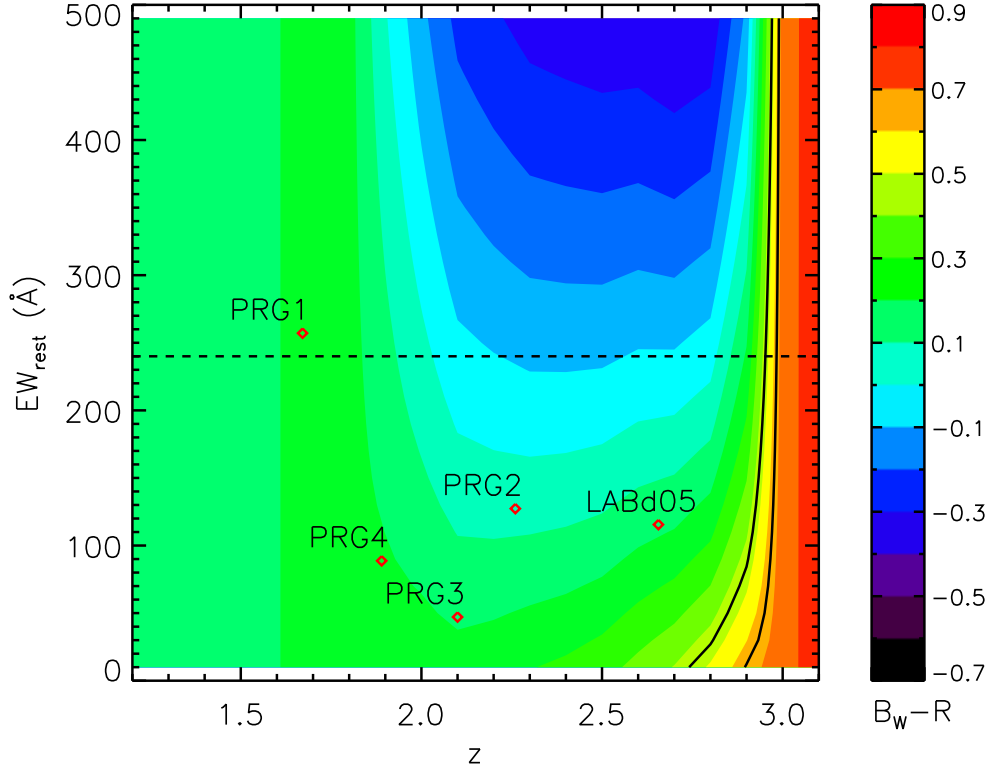


Figure 2.5 Expected $B_W - R$ colors for $\text{Ly}\alpha$ nebulae at redshifts $1.2 < z < 3.1$, where the colors are divided into 0.1 mag bins; the $B_W - R$ color cuts used in our survey are shown as black lines at $B_W - R < 0.45$ and at $B_W - R < 0.65$. The B_W bandpass will contain $\text{Ly}\alpha$ at $1.9 < z < 2.9$. $\text{Ly}\alpha$ nebulae are modeled as a 5 Myr single stellar populations with a $\text{Ly}\alpha$ line (unreddened; Bruzual & Charlot, 2003). The continuum at the position of $\text{Ly}\alpha$ is measured within $\pm 20\text{\AA}$ of the line. The stellar continuum is assumed to have the same morphology as the $\text{Ly}\alpha$, which means that these idealized $\text{Ly}\alpha$ nebulae would be detectable down to much lower redshifts where $\text{Ly}\alpha$ is not contained with the B_W band. The canonical upper limit for $\text{Ly}\alpha$ equivalent widths arising from stellar processes is shown (dashed line Charlot & Fall, 1993) along with the positions of the 5 confirmed $\text{Ly}\alpha$ sources from this survey (diamonds).

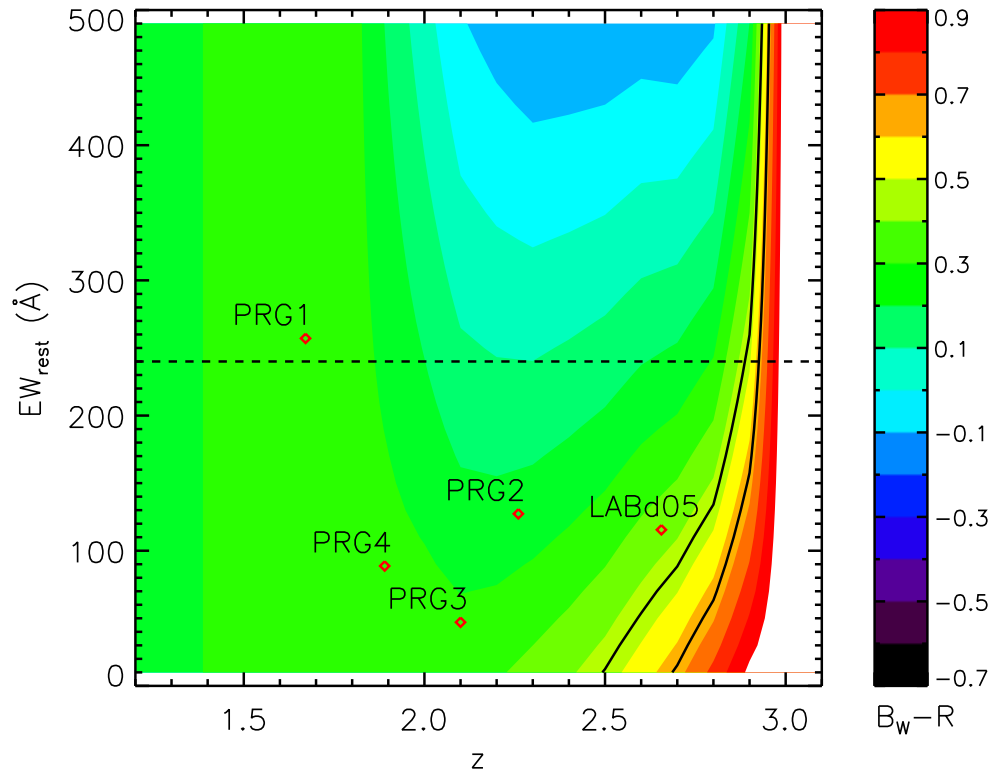


Figure 2.6 Same as Figure 2.5 except that the continuum is an unreddened 25 Myr model (single stellar population, unreddened; Bruzual & Charlot, 2003).

young galaxies; Chapter 4. For these reasons we do not apply any further morphological criteria at this point. We define our high priority region (Region A) as $B_W - R < 0.45$ and $\text{ISOAREA_WORLD} > 34 \text{ arcsec}^2$ and a second priority region (Region B) as $B_W - R < 0.65$ and $\text{Log}(\text{ISOAREA_WORLD}) > 0.934 \times (B_W - R) + 1.11 \text{ arcsec}^2$ (Figure 2.8). Our final high priority (second priority) candidate sample consists of 40 (40) sources over the entire ~ 9 square degree survey (Table 2.1). Finally, we selected a handful of candidates with promising diffuse morphologies from outside these regions as third priority follow-up targets.

Table 2.1. $\text{Ly}\alpha$ Nebula Candidates

Right Ascension (hours)	Declination (degrees)	Wavelet Size (arcsec ²)	$B_W - R$ (AB mag)	Priority
14:34:10.948	33:17:30.80	59.1	0.42	1
14:34:07.476	33:41:40.56	48.3	0.26	1
14:34:12.722	33:29:39.19	38.7	0.22	1
14:27:21.672	33:52:42.63	47.4	0.25	1
14:27:35.479	34:23:32.38	35.0	-0.26	1
14:27:32.520	34:12:13.39	34.4	-0.62	1
14:27:53.762	34:12:04.10	36.5	0.45	1
14:34:01.034	35:12:29.12	42.0	0.19	1
14:33:35.764	34:45:02.84	37.5	0.33	1
14:32:32.484	35:15:34.23	35.3	0.30	1
14:32:02.568	35:19:04.22	36.6	0.42	1
14:30:53.488	35:20:06.68	45.0	0.43	1
14:28:02.803	35:9:33.300	34.2	0.35	1
14:27:46.348	34:45:44.02	35.0	0.34	1
14:36:51.312	34:21:07.38	35.1	0.28	1
14:35:23.856	35:49:34.39	45.0	0.42	1
14:33:48.885	35:41:56.68	41.7	-0.08	1
14:30:57.662	35:45:47.26	59.6	0.43	1
14:30:55.192	35:28:54.76	61.6	0.43	1
14:28:32.733	35:41:04.56	37.8	-0.23	1
14:27:45.194	35:29:48.98	42.9	0.23	1
14:28:21.259	35:20:00.92	42.4	0.25	1
14:24:45.998	35:47:14.06	40.5	0.19	1
14:26:22.905	35:14:22.02	49.5	-0.49	1
14:28:19.735	32:54:48.70	37.1	0.44	1
14:27:10.447	32:48:41.76	35.4	0.41	1
14:25:16.629	32:43:35.47	39.0	0.14	1
14:24:49.761	32:47:42.61	34.9	-0.74	1
14:25:48.283	32:29:56.58	35.0	0.12	1

Table 2.1—Continued

Right Ascension (hours)	Declination (degrees)	Wavelet Size (arcsec ²)	$B_W - R$ (AB mag)	Priority
14:24:41.940	33:25:31.94	38.4	0.38	1
14:27:22.408	34:52:24.74	35.9	0.29	1
14:26:53.172	34:38:55.39	44.8	-0.67	1
14:27:07.840	34:47:48.84	35.4	0.43	1
14:26:14.714	34:44:34.22	49.9	0.43	1
14:25:39.859	34:49:59.19	37.1	0.14	1
14:24:43.869	34:48:34.45	36.9	0.37	1
14:26:43.850	34:9:36.828	36.1	0.03	1
14:26:19.982	34:04:27.01	35.7	-0.75	1
14:25:47.126	33:44:54.13	48.1	0.45	1
14:25:26.332	33:51:12.16	48.7	0.40	1
14:28:56.013	33:19:36.51	53.5	0.60	2
14:34:36.448	33:04:05.62	72.1	0.53	2
14:35:11.030	33:55:43.10	53.3	0.53	2
14:33:10.346	33:50:56.94	45.9	0.58	2
14:35:51.278	33:34:21.03	55.9	0.51	2
14:34:59.702	33:37:48.93	48.1	0.48	2
14:34:16.420	33:30:58.10	39.3	0.46	2
14:32:30.244	33:41:05.46	50.5	0.56	2
14:30:55.713	34:05:01.71	49.3	0.57	2
14:29:9.2784	34:25:42.38	55.8	0.58	2
14:29:06.271	34:11:30.26	53.5	0.48	2
14:27:29.894	34:11:25.22	56.2	0.48	2
14:35:12.336	35:11:08.62	55.7	0.56	2
14:34:38.700	35:04:19.84	38.4	0.46	2
14:34:35.932	35:07:9.912	44.2	0.57	2
14:32:36.883	35:18:00.32	49.1	0.57	2
14:31:53.066	35:14:36.45	62.6	0.53	2
14:31:41.253	35:21:9.864	39.5	0.48	2

2.2.4 Potential Contaminants

Due to the wide bandpass of the B_W filter, there are several populations that have the potential to contaminate our Ly α nebula candidate sample. The morphological selection method will tend to pick out any source of low surface brightness extended emission that cannot be easily identified as a nearby galaxy such as low surface brightness galaxies (LSBs) or even low surface brightness nebulae within the Galaxy. In principle lower redshift sources with [OII] $\lambda\lambda 3727, 3729$ emission in the selection band (B_W) are a contaminant population much as they are in Ly α -emitting galaxy surveys. In addition, galaxies and Ly α nebulae in the redshift desert ($1.2 < z < 1.8$) may be selected as candidates in our survey if they exhibit extended blue continuum emission or if the morphological selection is fooled by a close grouping of compact sources. As long as some fraction of the sources are blue, they may be targeted as high priority candidates. However, as discussed in the previous section, we do not remove these based on visual inspection because Ly α nebulae sometimes contain compact galaxies.

While this range of different populations should contaminate our sample in principle, not all of them will contribute in practice. We do not expect to find many LSBs because the $B_W - R$ color limit of our survey is selected to be bluer than typical LSB colors (i.e., $B_W - R = 1.49 \pm 0.60$; Habertzettl et al., 2007, also Figure 2.8); any remaining blue LSBs would be expected to show optical emission lines and be easily identified in follow-up spectroscopy. Low redshift [OII] emitters will not likely contaminate our sample due to the expected colors and morphological selection. To be selected as candidates in this survey these sources would need to have [OII] emission that is extended across several arcseconds, meaning that they would be [OII] nebulae at $z \lesssim 0.3$. If compact groupings of

Table 2.1—Continued

Right Ascension (hours)	Declination (degrees)	Wavelet Size (arcsec ²)	$B_W - R$ (AB mag)	Priority
14:28:19.840	34:46:57.14	50.4	0.61	2
14:36:41.373	34:15:10.26	52.1	0.55	2
14:38:41.956	33:53:24.79	59.5	0.63	2
14:38:33.249	34:03:59.32	39.6	0.52	2
14:37:06.588	33:56:52.65	41.3	0.52	2
14:34:22.348	35:15:34.27	46.3	0.51	2
14:33:02.844	35:47:29.43	52.7	0.50	2
14:31:15.055	35:41:47.76	50.1	0.55	2
14:31:28.245	35:26:57.91	47.3	0.56	2
14:32:03.760	35:18:54.86	37.4	0.46	2
14:29:59.978	35:39:26.89	42.4	0.47	2
14:29:29.198	35:47:10.78	49.5	0.52	2
14:27:58.617	35:44:28.42	44.4	0.50	2
14:30:04.687	35:35:9.060	134.0	0.61	2
14:28:54.998	35:30:21.70	64.9	0.52	2
14:28:25.999	35:21:15.62	42.7	0.48	2
14:29:06.398	35:24:32.22	47.2	0.54	2
14:32:22.768	32:49:42.67	53.1	0.53	2
14:25:35.205	32:49:34.17	42.6	0.49	2
14:25:22.339	32:54:23.65	39.9	0.48	2
14:27:14.791	34:31:54.55	47.7	0.52	2
14:26:34.106	33:49:53.61	44.3	0.51	2

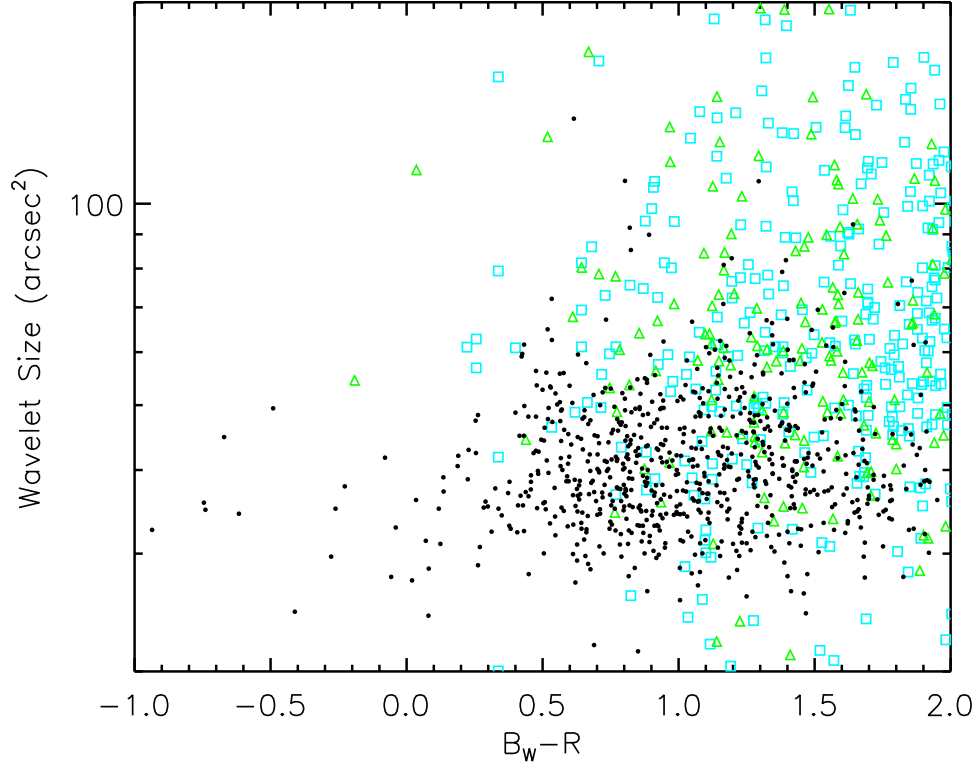


Figure 2.7 Size vs. $B_W - R$ color of Ly α nebula candidates selected using the morphological search pipeline. The candidates are shown (black circles) along with artifacts from the residual halos from bright galaxies (cyan squares) and detections of tidal tails and spiral arms (green triangles). The size axis corresponds to the size of the source in the wavelet power map and should not be taken to reflect the true size of the object, as discussed in the text.

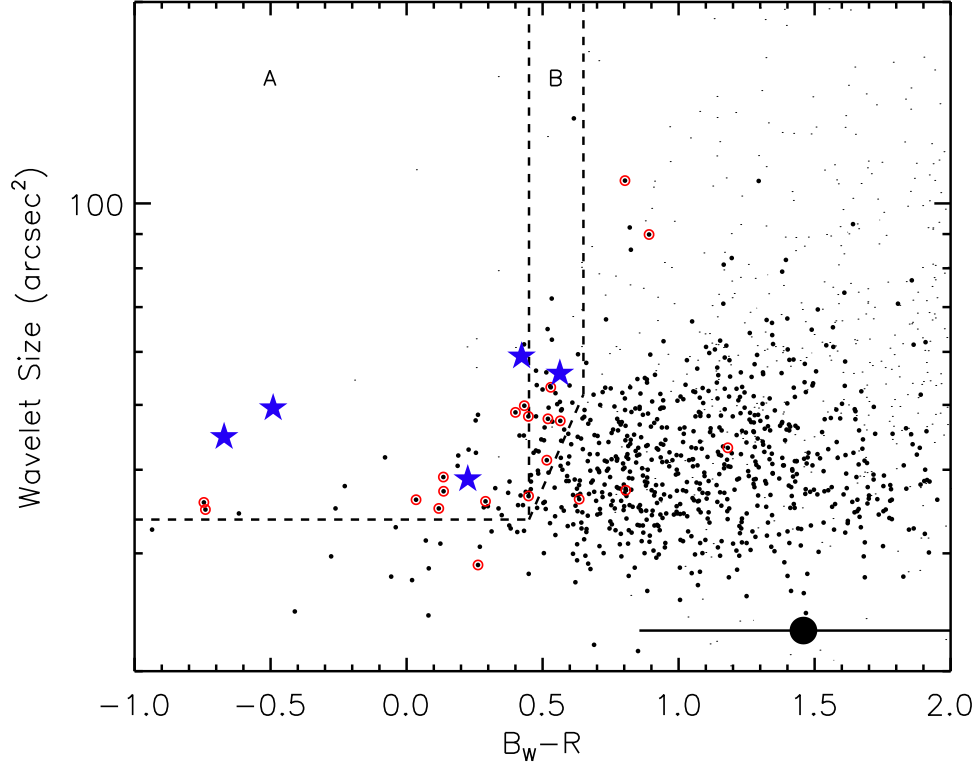


Figure 2.8 Size vs. $B_W - R$ color of $\text{Ly}\alpha$ nebula candidates selected using the morphological search pipeline. The high priority (A) and second priority (B) selection regions are indicated (dashed lines). The candidates are shown (black circles) along with spectroscopic targets with and without $\text{Ly}\alpha$ (blue stars and red circles, respectively). Artifacts described in the previous figure are shown as black dots. The large filled circle represents the typical color of low surface brightness galaxies (Haberzettl et al., 2007). The high (second) priority region contains 40 (40) $\text{Ly}\alpha$ nebula candidates. The size axis corresponds to the size of the source in the wavelet power map and should not be taken to reflect the true size of the object, as discussed in the text.

[OII]-emitters or extended [OII] nebulae were to be selected via our morphological search, the position of [OII] in the B_W , [OIII] in the R band, and $H\alpha$ in the R or I band would give the object redder colors, and therefore it is less likely they would be selected in our survey.

While LSBs and low redshift interlopers with emission lines are easily ruled out by follow-up spectroscopy, identifying line-less contaminants (e.g., Galactic reflection nebulae and $\text{Ly}\alpha$ nebulae or galaxies in the red desert including close groupings of compact sources) would require deeper spectroscopic follow-up than was practical when conducting a long-slit survey using a 6.5m telescope due to the faintness continua in these sources. Our spectroscopic campaign therefore focused on simply confirming whether or not a candidate showed strong line emission. If it did not, it was considered a contaminant for the purposes of this study. We discuss the survey contaminants further in Section 2.4.

2.3 Spectroscopic Follow-up

In this section we describe the spectroscopic follow-up of our $\text{Ly}\alpha$ nebula candidate sample.

2.3.1 Observations & Reductions

We obtained spectroscopic follow-up observations of 26 $\text{Ly}\alpha$ nebula candidates using the MMT and the Blue Channel Spectrograph during four separate runs in 2007 May, April 2008, and June 2008. Of these, 15 were from the high priority selection region, 5 were second priority, and 6 were third priority. The observing log is given in Table 2.2.

The observations used the 300 l/mm grating ($\lambda_c \approx 5713\text{\AA}$, $\Delta\lambda \approx 3100 - 8320\text{\AA}$). For each candidate we initially chose a slit orientation that would span

the longest dimension of the diffuse emission, and attempted to intersect a nearby bright reference object when possible. However, during the initial pilot run we found that the primary contaminants of our survey were faint continuum-only sources. We also decided it was essential to include a bright reference object on the slit and all subsequent slit positions were therefore chosen with this in mind. During the 2007 pilot run, we did not dither targets along the slit due to the lack of bright reference objects on the slit. During the later runs, we dithered the target along the slit by $\approx 5''$ in between exposures. The full list of targeted candidates is given in Table 2.3.

We reduced the spectroscopic data using IRAF³ in the usual manner. After performing the overscan and bias subtraction, we removed the response of the internal ‘Bright Continuum’ flatfield lamp by dividing out the median along columns and then applied the flatfield correction. Twilight flats were used to determine the illumination correction for the science frames. We removed cosmic rays using *xzap*⁴. We determined the wavelength solution using both HeArNe and HgCd comparison lamps, with an rms of $\approx 0.08\text{--}0.18\text{\AA}$, and then corrected the data for any slight systematic offset in the night sky lines. The night sky line wavelengths in the final spectra are correct to $\pm 0.42\text{\AA}$. The flux calibration was based on observations of the standard stars BD+33 2642, BD+26 2606, BD+28 4211, Feige 34, and Wolf 1346⁵. For each night we applied a grey shift ($\lesssim 0.1$ mag) and fit the relative sensitivity function. The typical 1σ line flux sensitivity limit in the region of Ly α was $6.6 \times 10^{-18} \text{ erg s}^{-1} \text{ cm}^{-2}$ (1σ assuming a line width of

³IRAF is distributed by the National Optical Astronomy Observatories, which are operated by the Association of Universities for Research in Astronomy, Inc., under cooperative agreement with the National Science Foundation.

⁴<http://iraf.noao.edu/iraf/ftp/iraf/extern/xdimsum020627>

⁵KPNO IRS Standard Star Manual

Table 2.2. Observing Log

UT Date	Instrumental Resolution ^a (arcsec)	Unvignetted Slit (Å)	Spatial Binning (arcsec)	Seeing (arcsec)	Conditions
2007 May 20	2.6	1.0×120	0.56	1.0-1.2	Clear, high winds
2007 May 21	2.6	1.0×120	0.56	1.0-1.2	Clear, high winds
2007 May 22	3.4	1.5×120	0.56	1.3-1.7	Clear, high winds
2008 April 3	3.4	1.5×120	0.28	1.0	Mostly clear
2008 April 30	3.4	1.5×120	0.28	1.2-1.9	Clear, high winds
2008 June 8	3.4	1.5×120	0.28	1.0	Clear
2008 June 9	3.4	1.5×120	0.28	1.1-2.0	Clear, high winds

Note. — All spectroscopic observations were taken with the MMT and the Blue Channel Spectrograph.

^aQuoted instrumental resolution is the average of measurements of the Hg $\lambda\lambda 4047$, Hg $\lambda\lambda 4358$, Hg $\lambda\lambda 5461$, and O $\lambda\lambda 5577$ lines.

$FWHM=12\text{\AA}$); at the very blue end of the spectrum the line sensitivity limit was $3.2 \times 10^{-17} \text{ erg s}^{-1} \text{ cm}^{-2}$.

Table 2.3. Spectroscopic Observations

Target	Right Ascension (hours)	Declination (degrees)	Wavelet Size (arcsec ²)	$B_W - R$ (AB mag)	Priority	UT Date	Exposure Time (s)	Class	Notes
1	14:30:06.864	35:34:36.73	108.2	0.80	3	2007 May 20-21	2400	Continuum	Galactic?
2	14:28:46.228	33:08:19.42	89.9	0.89	3	2007 May 20-21	10800	Continuum	Galactic?
3	14:34:10.948	33:17:30.80	59.1	0.42	1	2007 May 20	1800	Ly α	LABd05
4	14:35:12.336	35:11:08.62	55.7	0.56	2	2008 Jun 8-9	7200	Ly α	PRG1
5	14:32:22.768	32:49:42.67	53.1	0.53	2	2008 Jun 8	1800	Continuum	-
6	14:26:14.714	34:44:34.22	49.9	0.43	1	2008 Jun 8	3600	Continuum	-
7	14:26:22.905	35:14:22.02	49.5	-0.49	1	2008 Apr 3	3600	Ly α	PRG2
8	14:25:26.332	33:51:12.16	48.7	0.40	1	2008 Jun 9	3600	Continuum	-
9	14:25:47.126	33:44:54.13	48.1	0.45	1	2008 Apr 30	2400	Continuum	-
10	14:27:14.791	34:31:54.55	47.7	0.52	2	2008 Jun 8	1800	Continuum	-
11	14:31:28.245	35:26:57.91	47.3	0.56	2	2007 May 22	5400	Continuum	-
12	14:26:53.172	34:38:55.39	44.8	-0.67	1	2008 Apr 30	3600	Ly α	PRG4
13	14:29:27.837	34:59:06.14	43.1	1.18	3	2007 May 21	3600	Continuum	-
14	14:37:06.588	33:56:52.65	41.3	0.52	2	2007 May 20-21	4800	Continuum	-
15	14:25:16.629	32:43:35.47	39.0	0.14	1	2008 Jun 8	3600	Continuum	-
16	14:34:12.722	33:29:39.19	38.7	0.22	1	2008 May 20	10800	Ly α	PRG3
17	14:32:07.224	34:31:01.34	37.3	0.81	3	2007 May 22	3600	Continuum	-
18	14:25:39.859	34:49:59.19	37.1	0.14	1	2008 Jun 8	3600	Continuum	-
19	14:27:53.762	34:12:04.10	36.5	0.45	1	2007 May 20-21	8400	Continuum	-
20	14:26:00.842	35:02:52.36	36.1	0.63	3	2008 Apr 3	3600	Continuum	-

2.4 Individual Sources

Of the 15 high priority and 5 second priority candidates targeted for spectroscopic follow-up, 4 high priority sources and 1 second priority source had confirmed Ly α emission: we recovered the previously-discovered large Ly α nebula at $z \approx 2.66$ (LABd05; Dey et al., 2005) and discovered new Ly α sources at $z \approx 1.67$, $z \approx 1.88$, $z \approx 2.14$, and $z \approx 2.27$. In addition, we also targeted a handful of redder candidates that showed promising diffuse morphologies upon visual inspection (third priority). However, no Ly α or [OII] line emission was confirmed in any of the third priority candidates. In this section, we describe each of confirmed sources in turn and then discuss the primary contaminants to our survey. Figures 2.13-2.9 give the postage stamps, two-dimensional, and one-dimensional spectra of the Ly α sources; the coordinates and measured properties are listed in Table 2.4. The spectral extraction apertures were chosen to maximize the signal-to-noise ratio of Ly α , and the redshifts are measured from the Ly α line without any correction for Ly α absorption. The Ly α sizes along the slit were measured above a 3σ surface brightness limit of $\approx 7 \times 10^{-18}$ erg s $^{-1}$ cm $^{-2}$ arcsec $^{-2}$. The B_W surface brightnesses are measured as the average surface brightness above the isophotal surface brightness limit of $\mu = 27.8$ mag arcsec $^{-2}$, which is the typical 3σ surface brightness limit of NDWFS. The B_W sizes were estimated as a flux-weighted mean diameter above the same 3σ isophotal surface brightness limit⁶. This measure was chosen because Ly α nebulae often have very clumpy morphologies and depart strongly from Gaussian profiles, and hence a simple isophotal radius will underestimate the full angular extent of the source.

⁶The flux-weighted mean radius is equal to 2/3 of the full radius for a circular source of constant surface brightness.

Table 2.3—Continued

Target	Right Ascension (hours)	Declination (degrees)	Wavelet Size (arcsec ²)	$B_W - R$ (AB mag)	Priority	UT Date	Exposure Time (s)	Class	Notes
21	14:26:43.850	34:9:36.828	36.1	0.03	1	2008 Jun 9	3600	Continuum	-
22	14:27:22.408	34:52:24.74	35.9	0.29	1	2008 Apr 3	3600	Continuum	-
23	14:26:19.982	34:04:27.01	35.7	-0.75	1	2008 Apr 30	2400	Continuum	-
24	14:25:48.283	32:29:56.58	35.0	0.12	1	2008 Jun 9	3600	Continuum	-
25	14:24:49.761	32:47:42.61	34.9	-0.74	1	2008 Apr 30	3600	Continuum	-
26	14:25:32.966	34:39:11.95	28.8	0.26	3	2008 Apr 3	3600	Continuum	-

We stress that these size estimates are drawn from broad-band imaging and therefore underestimate the true nebular sizes. The conversion from B_W size to $\text{Ly}\alpha$ size that would have been measured in narrow-band observations depends on the depth of the images, the width of the narrow-band filter, and the profile of the $\text{Ly}\alpha$ nebula in both line and continuum emission. The $\text{Ly}\alpha$ nebulae discovered in this survey have B_W sizes that underestimate the $\text{Ly}\alpha$ sizes measured from the spectra by a factor of $\gtrsim 1.2$ -1.6 (Table 2.4).

Approximate estimates for the total $\text{Ly}\alpha$ luminosity, total $\text{Ly}\alpha$ isophotal area, and total $\text{Ly}\alpha$ size are also given in Table 2.4. The total $\text{Ly}\alpha$ luminosity was derived by scaling the $\text{Ly}\alpha$ luminosity within the spectroscopic slit by a geometric correction factor of $f_{geo} = A_{B_W} \times \nu / (\omega \times d)$, where A_{B_W} is the approximate area of the source on the B_W image, ν is the ratio of the $\text{Ly}\alpha$ and B_W sizes measured along the slit, ω is the slit width, and d is the aperture size. The total $\text{Ly}\alpha$ isophotal area was estimated by correcting A_{B_W} by a factor of ν^2 . The total $\text{Ly}\alpha$ size is simply the source size measured from the B_W image corrected by ν .

2.4.1 Confirmed $\text{Ly}\alpha$ Sources

In this section, we discuss each confirmed $\text{Ly}\alpha$ source in detail.

2.4.2 PRG1 — “The $\text{Ly}\alpha$ +HeII Blob”

PRG1 is the first example of a $\text{Ly}\alpha$ nebula with strong, spatially extended HeII emission and weak metal lines, suggestive of a hard ionizing continuum and potentially low metallicity gas (Figure 2.9). The B_W imaging shows a diffuse nebula and several compact sources, the strongest of which is located to the West-Northwest of the nebula. Despite the strong $\text{Ly}\alpha$ emission and large size (>60 kpc across), this source was selected as a second priority candidate because of its low

Table 2.4. Ly α Nebula Measurements

	PRG1	PRG2	PRG3	PRG4	LABd05
Aperture (arcsec)	1.5 \times 5.04	1.5 \times 7.84	1.0 \times 5.60	1.5 \times 1.68	1.0 \times 4.48
Redshift	1.6731 \pm 0.0003	2.2668 \pm 0.0001	2.1368 \pm 0.0007	1.8883 \pm 0.0005	2.6564 \pm 0.0003
Ly α Diameter Along Slit (arcsec)	7.56	10.90	8.40	3.36	9.50
B_W Diameter Along Slit (arcsec)	6.43	8.16	6.19	2.26	5.86
Flux-weighted Mean B_W Diameter (arcsec)	4.42	4.91	4.15	4.21	4.14
B_W SB (mag arcsec $^{-2}$)	27.4	27.2	27.0	27.1	27.0
$F_{Ly\alpha}$ (10^{-17} erg s $^{-1}$ cm $^{-2}$)	44.1 \pm 4.0	49.2 \pm 1.1	10.2 \pm 1.2	10.3 \pm 1.2	19.0 \pm 0.9
$L_{Ly\alpha}$ (10^{42} erg s $^{-1}$)	8.2 \pm 0.7	19.3 \pm 0.4	3.5 \pm 0.4	2.6 \pm 0.3	10.9 \pm 0.5
Ly α EW (\AA)	257.1 \pm 29.1	127.3 \pm 6.3	47.1 \pm 6.4	88.7 \pm 11.8	115.5 \pm 9.5
Ly α FWHM (\AA)	9.19 \pm 0.60	8.52 \pm 0.19	23.36 \pm 7.90	6.51 \pm 0.89	15.44 \pm 0.70
Ly α σ_v (km s $^{-1}$)	361.2 \pm 23.7	273.9 \pm 6.1	782.1 \pm 264.3	236.8 \pm 32.2	443.3 \pm 20.0
$F_{HeII\lambda 1640}$ (10^{-17} erg s $^{-1}$ cm $^{-2}$) ^a	5.8 \pm 1.0	< 2.2	< 1.4	< 1.0	< 2.9
Approximate Total $L_{Ly\alpha}$ (10^{42} erg s $^{-1}$)	44.2 \pm 4.0	93.3 \pm 2.0	25.5 \pm 3.1	- ^b	119.9 \pm 5.8
Approximate Ly α Isophotal Area (arcsec 2)	34.6	42.5	30.4	- ^b	30.3
Approximate Ly α Size (kpc)	66.1	80.9	70.1	- ^b	80.2

^aHe II λ 1640 flux upper limits are 3σ values.

^bApproximate values for PRG4 have not been included because the B_W is not an accurate tracer of the Ly α emission in this source.

redshift and relatively red $B_W - R$ color. At $z \approx 1.67$, $\text{Ly}\alpha$ is right at the edge of the optical window and not contained within the B_W band. Thanks to the diffuse blue continuum (95%) and HeII emission (5%), the source was selected by our survey none the less. As the lowest redshift $\text{Ly}\alpha$ nebula known and the only one for which HeII is spatially extended, PRG1 is an ideal target for detailed study of the physical conditions and kinematics within $\text{Ly}\alpha$ nebulae. Analysis of the metallicity and source of ionization in PRG1 is given in Chapter 5 (Prescott et al., 2009).

2.4.3 PRG2 — “The Diamond Blob”

PRG2 source is a large $\text{Ly}\alpha$ nebula at $z \approx 2.26$ with a roughly diamond-shaped morphology in the B_W image (Figure 2.10). At the Southwestern corner is a very blue compact source that appears to be a $\text{Ly}\alpha$ -emitting galaxy from the spectrum. This source is a perfect example of why it is important not to reject $\text{Ly}\alpha$ nebula candidates due to clumpy morphology or the presence of embedded compact sources (as discussed in Section 2.2.2). The $\text{Ly}\alpha$ nebula spans at least 80 kpc in $\text{Ly}\alpha$ and shows a velocity gradient across the Northeastern part of the source. No other strong lines are detected in the observed optical spectrum, although there may be a weak detection at the position of HeII and CIII]. The redshift of this source is ideal for follow-up NIR spectroscopy as the rest-frame optical emission lines ([OII], [OIII], $\text{H}\beta$, and $\text{H}\alpha$) will be observable in the J , H , and K bands.

2.4.4 PRG3 — “The Horseshoe Blob”

PRG3 is a ≈ 40 kpc $\text{Ly}\alpha$ nebula at $z \approx 2.1$ (Figure 2.11). It has a rather clumpy horseshoe-shaped morphology in the B_W imaging. The spectrum shows slight velocity structure and strong continuum, but no other emission lines.

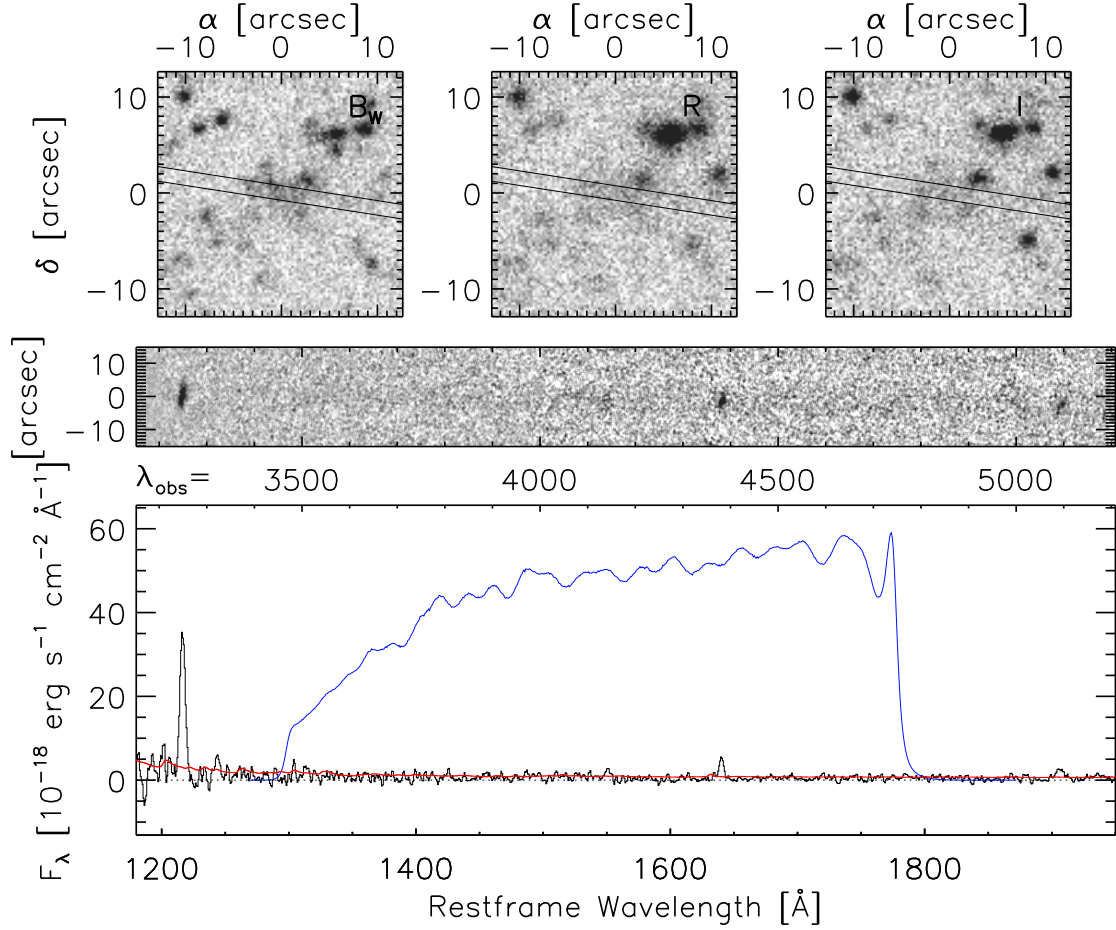


Figure 2.9 Imaging and MMT spectroscopic observations of PRG1, a $\text{Ly}\alpha$ nebula at $z \approx 1.67$. The top row shows the optical B_W , R , and I imaging along with the slit used for follow-up spectroscopy. The central panel contains the two-dimensional spectrum versus observed wavelength and the bottom panel presents the one-dimensional spectrum extracted from a $1.5 \times 5.04''$ aperture. The error spectrum (red line) and B_W bandpass (blue line) are shown.

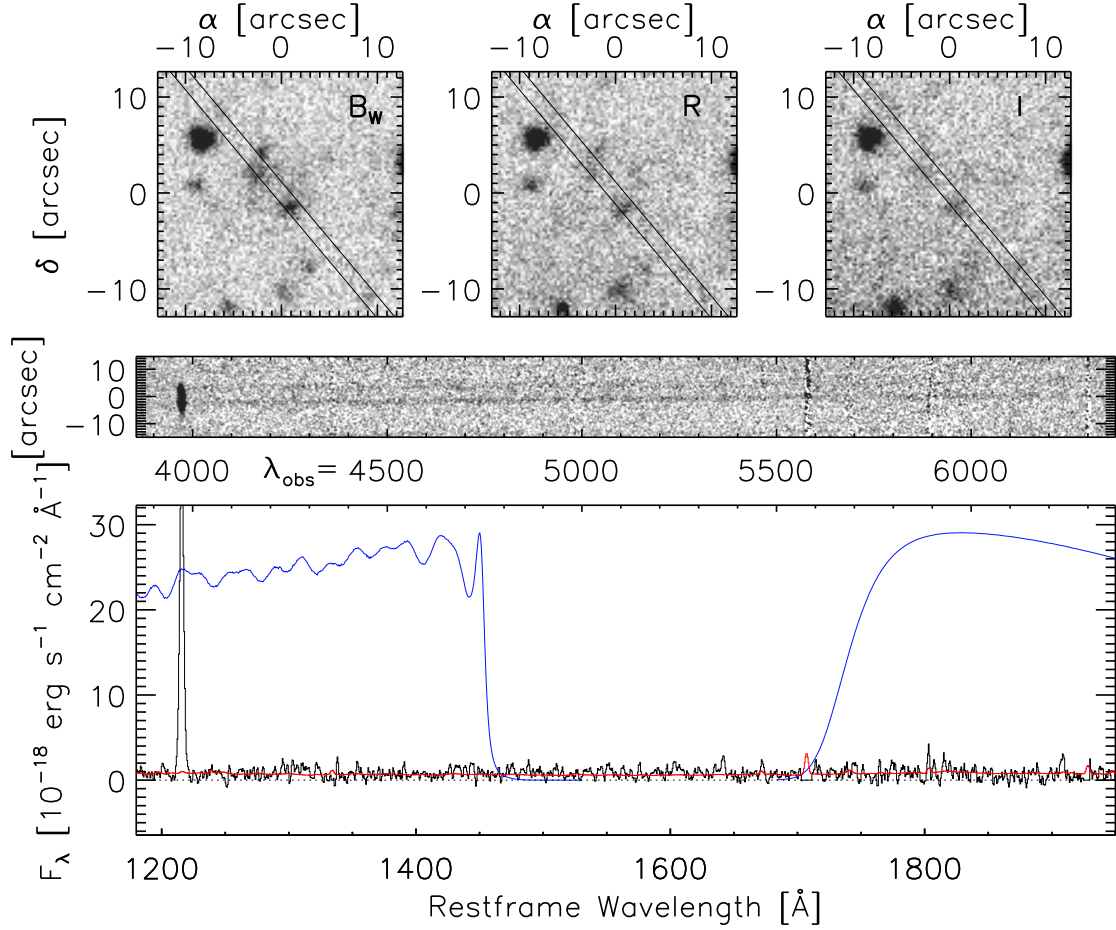


Figure 2.10 Imaging and MMT spectroscopic observations of PRG2, a Ly α nebula at $z \approx 2.27$. The top row shows the optical B_W , R , and I imaging along with the slit used for follow-up spectroscopy. The central panel contains the two-dimensional spectrum versus observed wavelength and the bottom panel presents the one-dimensional spectrum extracted from a $1.5 \times 7.84''$ aperture. The error spectrum (red line) and B_W and R bandpasses (blue line) are shown.

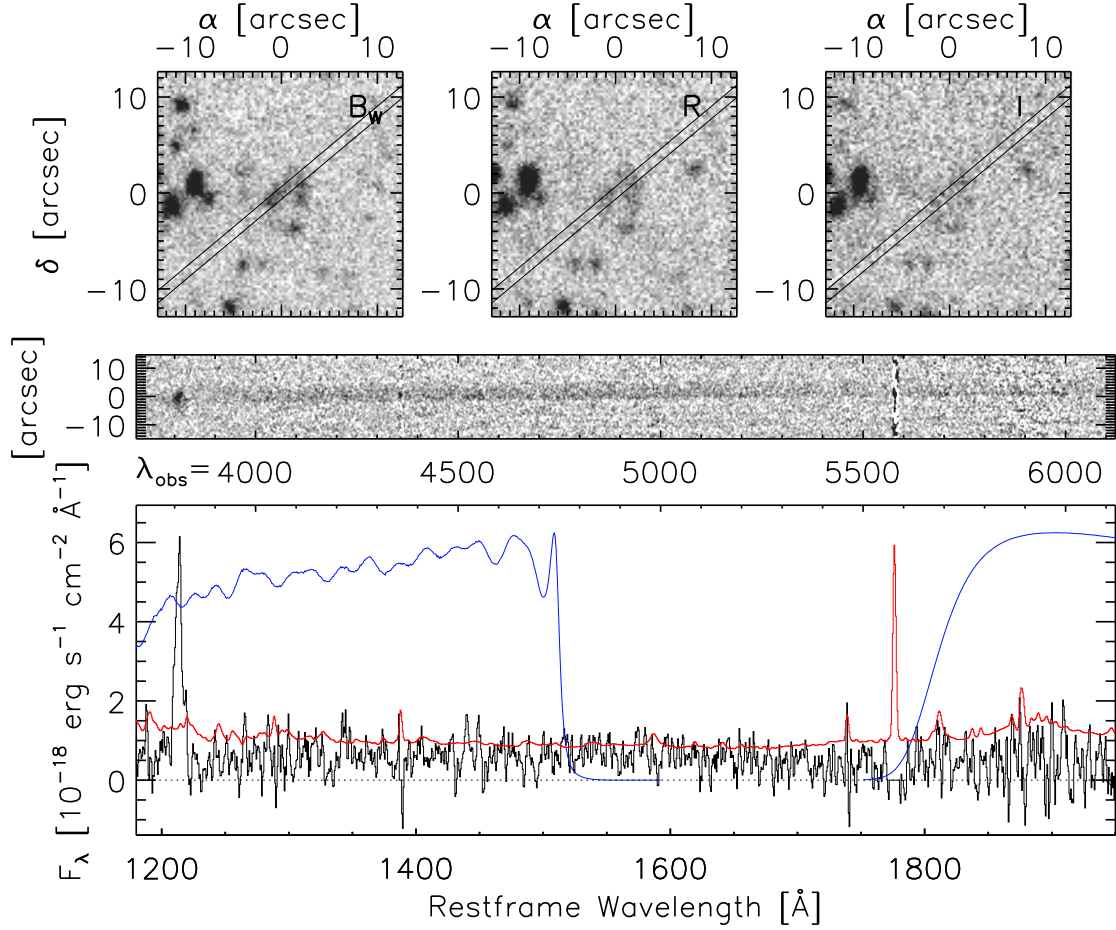


Figure 2.11 Imaging and MMT spectroscopic observations of PRG3, a Ly α nebula at $z \approx 2.14$. The top row shows the optical B_W , R , and I imaging along with the slit used for follow-up spectroscopy. The central panel contains the two-dimensional spectrum versus observed wavelength and the bottom panel presents the one-dimensional spectrum extracted from a $1.0 \times 5.6''$ aperture. The error spectrum (red line) and B_W and R bandpasses (blue line) are shown.

2.4.5 PRG4

PRG4 appears to be a candidate that was selected due to a close grouping of compact sources (Figure 2.12). Due to the very blue color, it was selected as a high priority target. Although the B_W size of the full grouping is roughly $6''$, the observed $\text{Ly}\alpha$ at $z \approx 1.89$ is only marginally extended along the direction of the spectroscopic slit ($2.8''$, 24 kpc). The source may be larger — there is diffuse B_W emission seen to the Southwest in the B_W imaging — but without further spectroscopy, we cannot determine if it is associated. No other lines are seen in the spectrum.

2.4.6 LABd05

This is the source that was the inspiration for our broad-band $\text{Ly}\alpha$ nebula search (Figure 2.13 Dey et al., 2005). One of the largest $\text{Ly}\alpha$ nebulae known ($\gtrsim 100$ kpc), it is located at $z \approx 2.66$. From the B_W imaging, it was clear that there are two compact sources embedded with the nebula. Detailed study of ground-based data revealed that the one to the Northeast is a Lyman break galaxy at the same redshift and the one to the Southwest is an interloper galaxy at $z \approx 3.2$. Dey et al. (2005) presented a detailed analysis of the energetics of the system from ground-based data. Chapter 4 presented high resolution imaging of LABd05 from HST/ACS and NICMOS, revealing that there are 7 compact galaxies within the system alongside as well as an obscured AGN.

2.4.7 Survey Contaminants

The dominant contaminants in both the primary and secondary samples were sources with spatially resolved blue continuum emission but no emission lines visible over the entire observed range of 3200-8300Å. We found no sources that

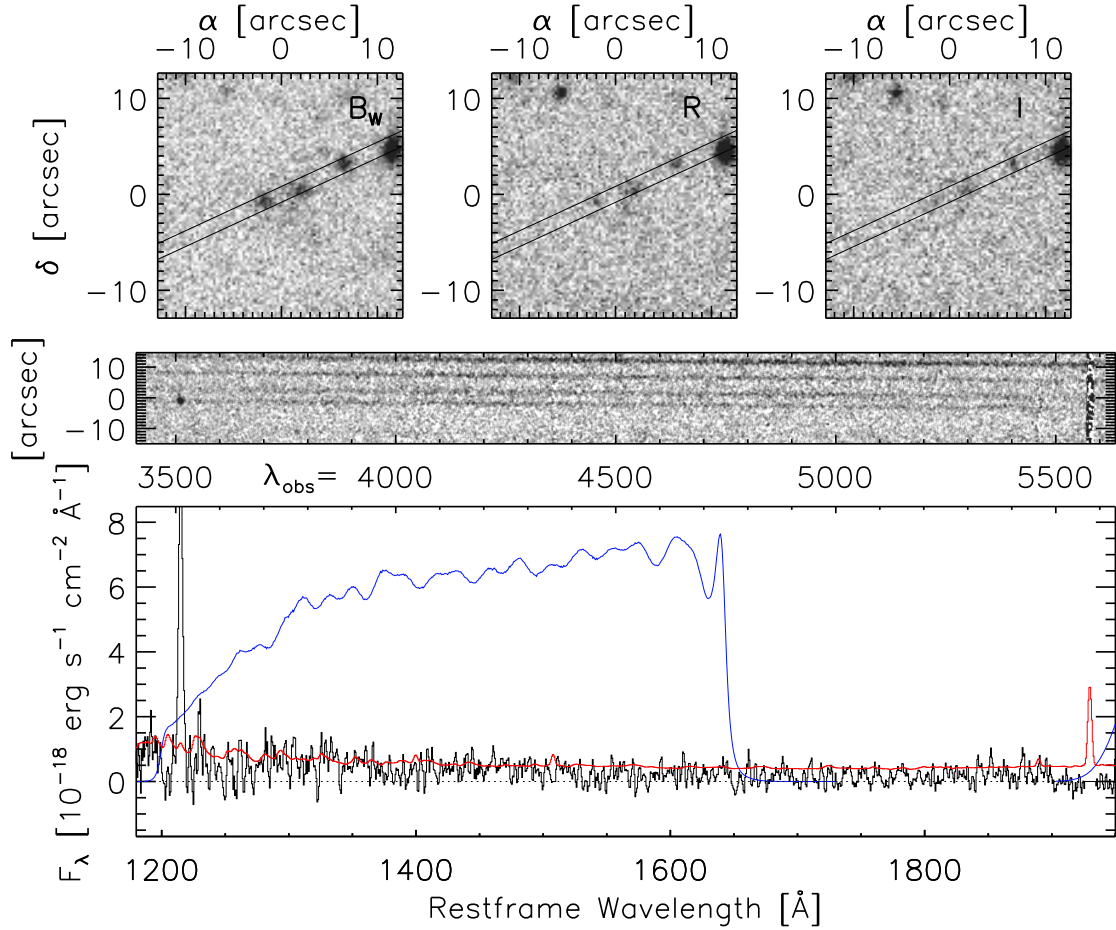


Figure 2.12 Imaging and MMT spectroscopic observations of PRG4, a Ly α nebula at $z \approx 1.89$. The top row shows the optical B_W , R , and I imaging along with the slit used for follow-up spectroscopy. The central panel contains the two-dimensional spectrum versus observed wavelength and the bottom panel presents the one-dimensional spectrum extracted from a $1.5 \times 1.68''$ aperture. The error spectrum (red line) and B_W and R bandpasses (blue line) are shown. The size of PRG4 is unknown; the source is very compact along the spectroscopic slit, but additional diffuse emission is visible to the South in the B_W imaging.

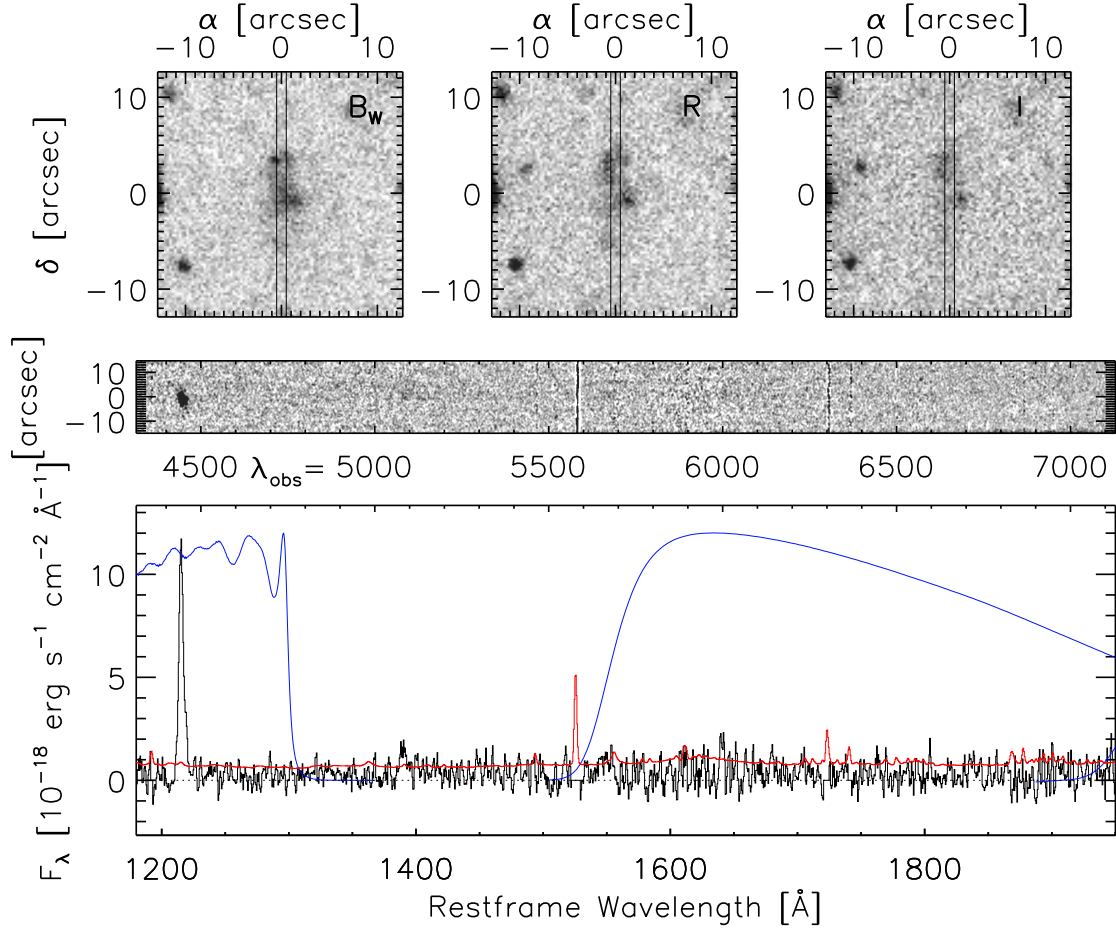


Figure 2.13 Imaging and MMT spectroscopic observations of LABd05, a previously-known Ly α nebula at $z \approx 2.656$ (Dey et al., 2005). The top row shows the optical B_W , R , and I imaging along with the slit used for follow-up spectroscopy. The central panel contains the two-dimensional spectrum versus observed wavelength and the bottom panel presents the one-dimensional spectrum extracted from a $1.0 \times 4.48''$ aperture. The error spectrum (red line) and B_W and R bandpasses (blue line) are shown.

showed extended line emission in lines other than $\text{Ly}\alpha$, which is consistent with the argument we made against low redshift line-emitting contaminants in Section 2.2.4. Sources either showed $\text{Ly}\alpha$ emission (with or without other emission lines or continuum) or showed nothing but continuum emission. Two of the continuum-only cases from the second and third priority samples were so large that they are almost certainly located within the Galaxy, e.g., low surface brightness Galactic reflection nebulae. Since low redshift blue star-forming populations or LSBs would be expected to show $[\text{OII}]$, $[\text{OIII}]$, or $\text{H}\alpha$ emission lines, the remaining contaminants are likely sources at high redshift where $\text{Ly}\alpha$ is not yet visible in the optical but where $[\text{OII}]$ has been redshifted out of the red end of the MMT/Blue Channel spectra (i.e., with redshifts $1.2 \lesssim z \lesssim 1.6$, in the redshift desert). Despite the lack of line emission in the B_W band, these sources were selected as spatially-extended, blue sources by the morphological search either due to sufficiently extended, blue continuum emission or a close grouping of projected neighbors. These sources may in fact be galaxies or $\text{Ly}\alpha$ nebulae in the redshift desert. The fact that one of the $\text{Ly}\alpha$ nebulae confirmed from this survey (the case at $z \approx 1.67$) is below the redshift where $\text{Ly}\alpha$ would be covered by the B_W -band gives weight to this hypothesis. This source was selected by our survey due to the blue continuum emission, and thanks to the excellent blue sensitivity of MMT/Blue Channel we were still able to detect its $\text{Ly}\alpha$ emission at 3250\AA . Without deeper spectroscopy capable of identifying stellar absorption features or UV spectroscopy from space, however, it is not possible to confirm the origin of the continuum-only sources on a case by case basis. The presence of continuum does confirm that these are indeed real astrophysical sources and not artifacts within the NDWFS imaging.

Due to the fact that sources either showed Ly α emission or continuum emission only and due to the faintness of our targets, we defined the primary purpose of the follow-up spectroscopy to be determining whether or not there was in fact an emission line in the system. Candidates with strong line emission in the B_W -band are easily detectable with the MMT/Blue Channel. However, sources with only continuum emission are much fainter and require much longer integration times in order to produce a high signal-to-noise ratio spectrum. We therefore integrated on each of the 26 targeted candidates up until the point where we could either confirm the presence of a line or confirm the presence of continuum with no strong lines. This strategy allowed us to target the largest number of candidates. Deeper spectroscopy of continuum-only sources to detect absorption features is left to future observations with larger telescopes.

2.5 The Selection Function

While narrow-band surveys effectively rely on the narrow width of the filter to eliminate contaminant sources — because only a small subset of sources will show the narrow-band excess required to be selected as a line-emitting candidate — in using deep broad-band data, we have to contend with every blue object in the field. Our iterative method is designed to remove as many contaminants as possible, but this means that our survey is most sensitive within a restricted range of size, surface brightness, and redshift. In this section, we discuss Monte Carlo simulations used to probe our survey sensitivity as a function of the two observables (angular size and B_W surface brightness) and as a function of redshift.

2.5.1 The Simulations

Here we discuss Monte Carlo simulations used to estimate the selection function of our search and how our survey complements other systematic Ly α nebulae surveys.

First, we generated a catalog of artificial sources that represent a range of possible physical characteristics for Ly α nebulae, inserted the fake sources into the imaging data, and determined what fraction are recovered when using the same selection algorithm as in the science survey. Unlike in the case of Ly α -emitting galaxy surveys, the reddening distribution, luminosity function, morphology distribution, and equivalent width distributions of Ly α nebulae are not well-constrained. We therefore chose to select source properties from flat distributions of observational rather than intrinsic properties (B_W size and surface brightness), since those are the parameters that most affect the surveys ability to select a source as a Ly α nebula candidate. We start by randomly selecting the angular size and B_W surface brightness of the source, all drawn from flat distributions spanning the ranges populated by Ly α nebulae (1-12'' angular sizes, 24-28 mag arcsec⁻² B_W surface brightnesses).

Next, we generated 2D images with the correct magnitudes and added them to the survey images. While Ly α nebulae show a range of morphologies — some smooth and others with multiple high surface brightness clumps or embedded galaxies and AGN — in order to understand our selection function it is important to keep our method simple, understandable, and reproducible when generating the 2D images. For the primary selection function simulation we therefore model simple Ly α nebulae using ellipses of constant surface brightness in order to understand how our survey's sensitivity depends on the B_W size and B_W surface

brightness of the source. We use a fixed axis ratio of 0.7 and assign a random position angle. After adding Poisson noise, we insert artificial $\text{Ly}\alpha$ nebulae into a representative $30' \times 30'$ image at random positions. We run this artificial image through the same selection algorithm as the science survey, and track how many of the artificial sources are recovered as a function of angular B_W size and B_W surface brightness.

2.5.2 Angular Size and B_W Surface Brightness Selection Function

We define a source as having been successfully recovered if a candidate source position is found within one semi-major axis of the inserted ellipse position. Figure 2.14 shows the fraction of fake $\text{Ly}\alpha$ nebulae recovered as a function of angular size and B_W surface brightness. The $\text{Ly}\alpha$ nebulae found in this survey are shown for reference. Not surprisingly given our broad-band strategy, we are only sensitive to large and luminous $\text{Ly}\alpha$ nebulae with B_W angular sizes $\gtrsim 4''$ and B_W surface brightness $\approx 27 \pm 0.5 \text{ mag arcsec}^{-2}$. At the bright end, we miss sources if they are brighter than the bright star/galaxy threshold leading them to be replaced with sky; at the faint end, we are limited by sky noise. In the size dimension, our morphological search was tuned to select spatially extended sources within a physically-motivated size range, i.e., similar in size to LABd05. Our survey is therefore not sensitive to sources significantly smaller than this scale by construction. The largest size scales probed by our survey are well beyond the realm of known $\text{Ly}\alpha$ nebulae, thus our search is sensitive to the largest and brightest $\text{Ly}\alpha$ nebulae.

Otherwise detectable sources are not recovered if they land in close proximity to a bright star or galaxy or in a noisy area at the edge of the imaging. These losses are included in the final recovery fractions and are the reason why the measured

recovery fractions do not reach 100% even for the most sensitive region of the survey.

2.5.3 Redshift Selection Function

In order to interpret the discovery of 5 $\text{Ly}\alpha$ nebulae within our survey volume, we need to determine the redshift selection function of each source. To do this, we compute the expected B_W angular size and B_W surface brightness for the observed sources across the full redshift range of the survey. We use these size and surface brightness measurements in combination with the simulations from Section 2.5.1 to assign the correct recovery fraction for each source at each redshift. In computing the angular size and surface brightness as a function of redshift, we need to take into account both the cosmological effects as well as the effect of the object spectrum moving through the non-square B_W bandpass. Ideally, we would use observed spectra to make the bandpass corrections, but in practice, the spectra do not sample a wide enough range in rest-frame wavelength and are too noisy to be used directly. Instead, we create a spectral model for each source using the measured equivalent widths and a range of reasonable continuum templates (5, 25, and 100 Myr unreddened single stellar populations; Bruzual & Charlot, 2003). This range of continuum templates brackets the observed colors of the sources, with the exception of PRG1 for which a very red source to the West-Northwest contaminates the measured colors. We use these spectral models to calculate the factor by which the B_W flux changes as the source redshifts through the filter and scale the source flux and size to account for surface brightness dimming.

Figures 2.15-2.19 show the recovery fraction for each $\text{Ly}\alpha$ source as a function of redshift and the path that the source follows in surface brightness vs. angular

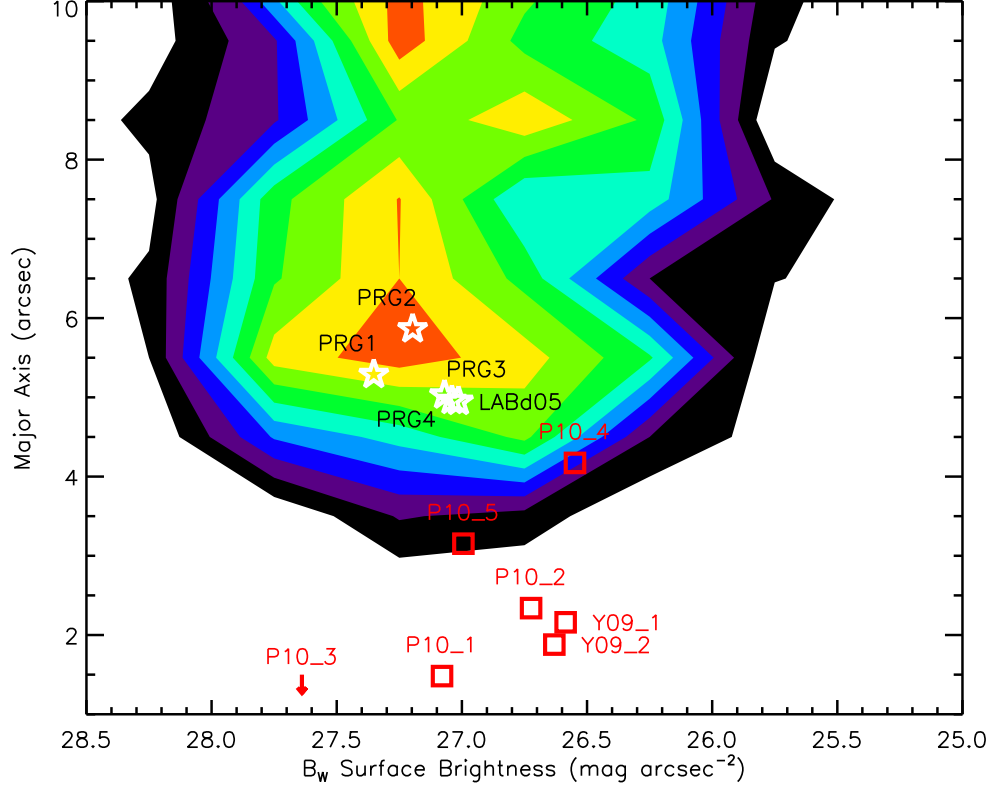


Figure 2.14 The selection function of our survey as a function of angular size and average B_W surface brightness. The color range corresponds to recovery fractions ranging from 0.1 (black) to 0.9 (red). The correspondence between the modeled sources and the true $\text{Ly}\alpha$ nebulae is not exact, making it difficult to place actual $\text{Ly}\alpha$ nebulae accurately on this plot. None the less, for the purposes of illustration the approximate locations of the $\text{Ly}\alpha$ nebulae found in this survey are shown (white stars), derived by computing the equivalent major axis of an ellipse with the same B_W area as the $\text{Ly}\alpha$ nebula. The $\text{Ly}\alpha$ nebulae from other surveys listed in Table 2.5 are shown (red open squares).

size space. Each source has a very different redshift completeness curve, as a consequence of the fact that our survey is based on broad-band imaging. In each of the observed $\text{Ly}\alpha$ nebulae, the $\text{Ly}\alpha$ emission line contributes but does not dominate the B_W flux. which implies that the continuum contributes substantially. This means that sources with $\text{Ly}\alpha$ outside the B_W band can be selected by our search if they are sufficiently diffuse in morphology and blue in color. Over the large redshift range of our search, a source will fade by of order $1 \text{ mag arcsec}^{-2}$ via surface brightness dimming, which is comparable to the range of B_W surface brightnesses over which our survey is sensitive. Thus, a source that is detectable at the low redshift end of our survey will fade and drop out of our surface brightness selection window if moved to higher redshift; conversely, a source that is detectable at the high redshift end of our survey will brighten as it moves to lower redshift and eventually be too bright to be selected. Simply put, sources discovered at the low redshift end of our survey will therefore be intrinsically fainter on average in terms of B_W luminosity than those discovered at the high redshift end and will therefore have a very different recovery fraction curve as a function of redshift. In the case of our observed sources, the source was found roughly near the middle of the redshift range for which it is detectable. The dashed lines on the recovery fraction plots indicate the redshift at which the source fades into or out of the surface brightness selection window; the same selection window is shown on the bottom panel for reference. The shape of the recovery fraction curve is driven primarily by this surface brightness effect and not by the $\text{Ly}\alpha$ line redshifting in or out of the filter bandpass.

Figure 2.20 illustrates the sensitivity of these recovery fraction curves to the choice of continuum template age for each source. With older and redder con-

tinuum templates, the continuum in the region of $\text{Ly}\alpha$ is reduced, leading to a narrower range of high recovery fractions. The final panel compares the recovery fraction curves for all 5 $\text{Ly}\alpha$ sources in the case of a 25 Myr model.

We note that below $z \approx 1.2$ the $[\text{OII}]$ emission line will be visible in our follow-up spectroscopy, but at redshifts of $z \approx 1.2 - 1.6$ (the redshift desert) galaxies and $\text{Ly}\alpha$ nebulae will appear as continuum-only sources. This is consistent with the hypothesis that at least some fraction of the “contaminant” continuum-only sources we discussed in Section 2.4.7 are in fact galaxies or $\text{Ly}\alpha$ nebulae in the redshift desert.

2.5.4 Known $\text{Ly}\alpha$ Nebulae as Test Cases

The NDWFS Boötes field is a wide-area field that has received a lot of multiwavelength attention. In addition to our broad-band search, traditional narrow-band survey for both $\text{Ly}\alpha$ nebulae and $\text{Ly}\alpha$ -emitting galaxies have been carried out, some by us and some by other researchers (Yang et al., 2009; Prescott et al., 2008). In the process, a handful of other $\text{Ly}\alpha$ nebulae have been discovered within the Boötes field that were not recovered by our broad-band search. These sources provide real test cases for understanding the selection function of our survey. A list of these sources is given in Table 2.5.

The known $\text{Ly}\alpha$ nebulae missed by our survey fall into two morphological categories: either the $\text{Ly}\alpha$ emission surrounds a much brighter compact continuum source (‘core-halo’ morphology) or the diffuse B_W emission is too faint to be selected by our search algorithm. In the first category are the $\text{Ly}\alpha$ nebulae discovered by Yang et al. (2009). Two of their $\text{Ly}\alpha$ nebulae (Y09_1 and Y09_2) consist of faint $\text{Ly}\alpha$ halos (undetected in the broad-band imaging) surrounding bright continuum sources. Due to the bright central sources, both objects are rejected

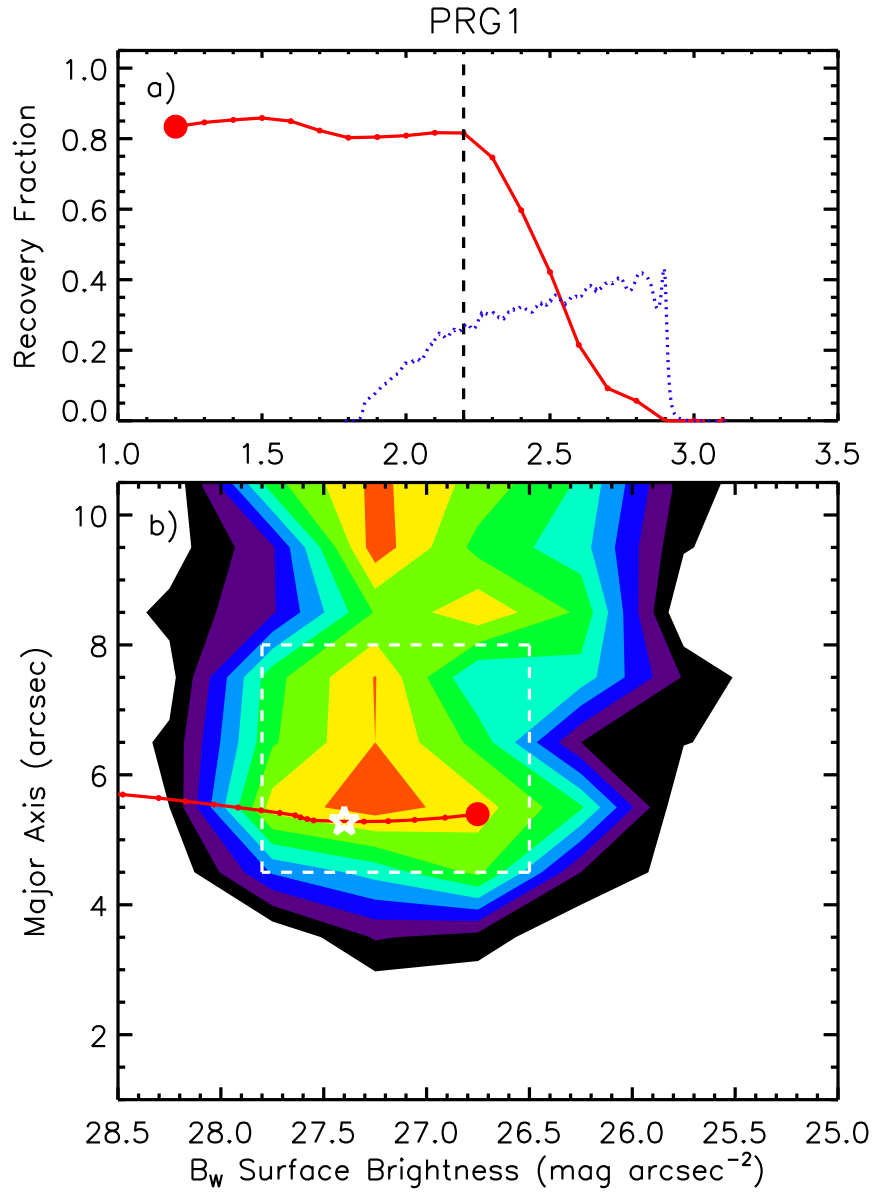


Figure 2.15 a) Recovery fraction as a function of redshift. The B_W bandpass is shown (blue dotted line), along with the redshifts where the source fades out of the high sensitivity region of the survey (dashed lines). b) Path of the source (red line) from low redshift (large red circle) to high redshift. The observed position (white star) and the high sensitivity region of the survey (white dashed lines) are shown. The colored contours span recovery fractions of 0.1 (black) to 0.9 (red).

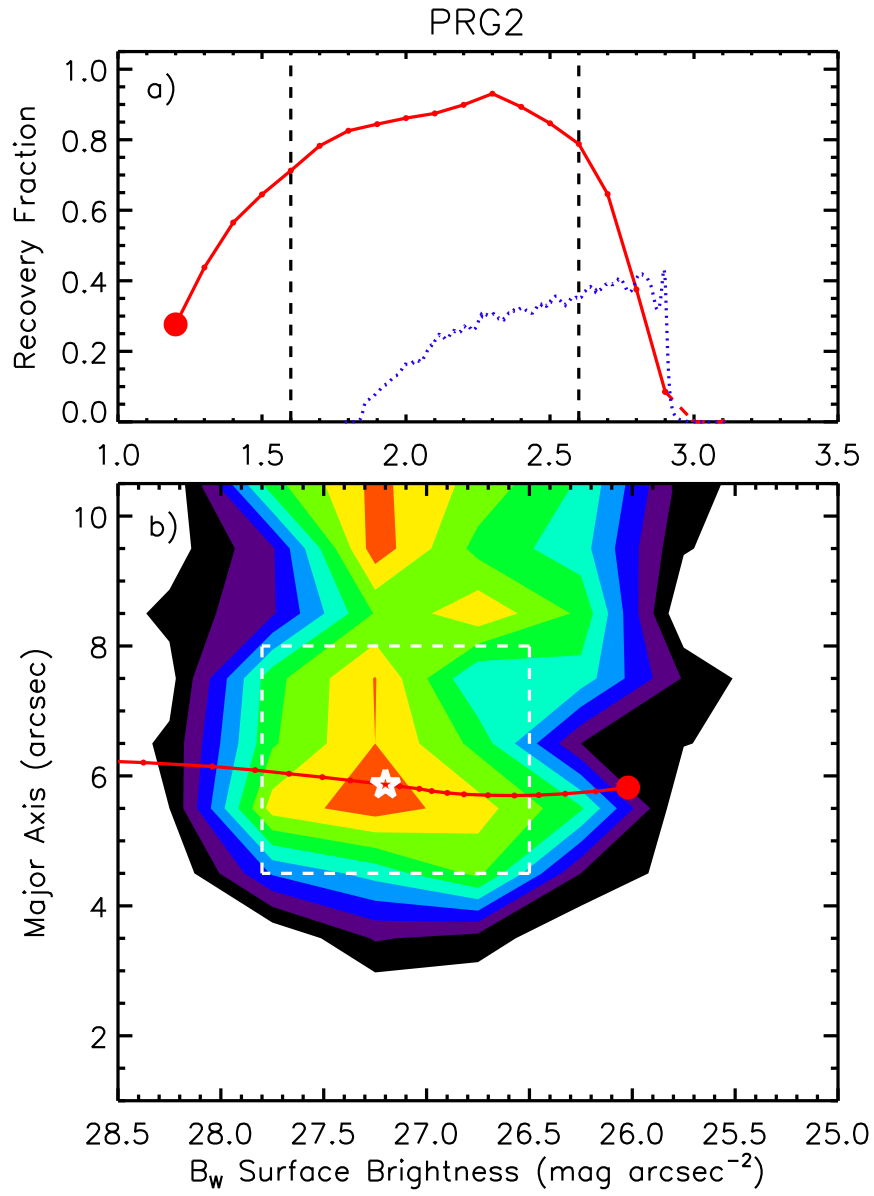


Figure 2.16 Same as Figure 2.15 but for PRG2.

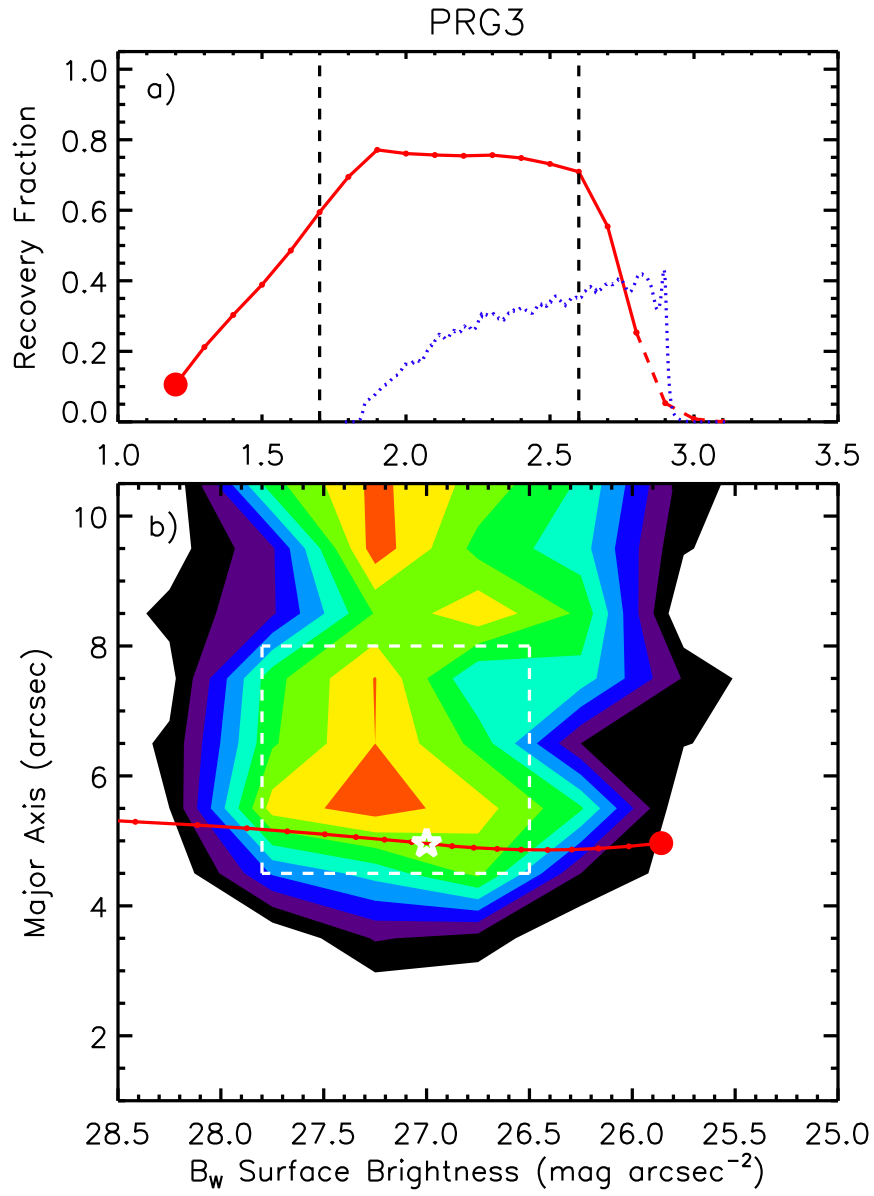


Figure 2.17 Same as Figure 2.15 but for PRG3.

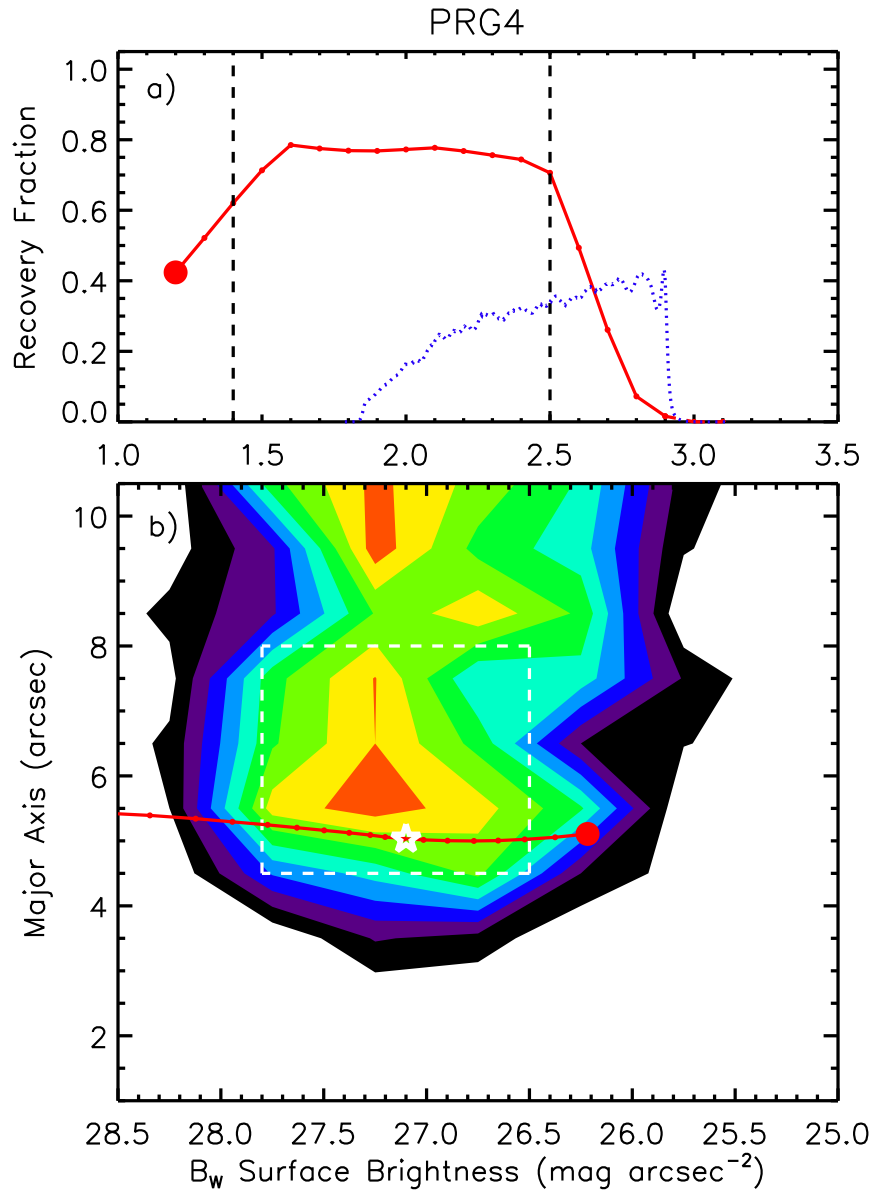


Figure 2.18 Same as Figure 2.15 but for PRG4.

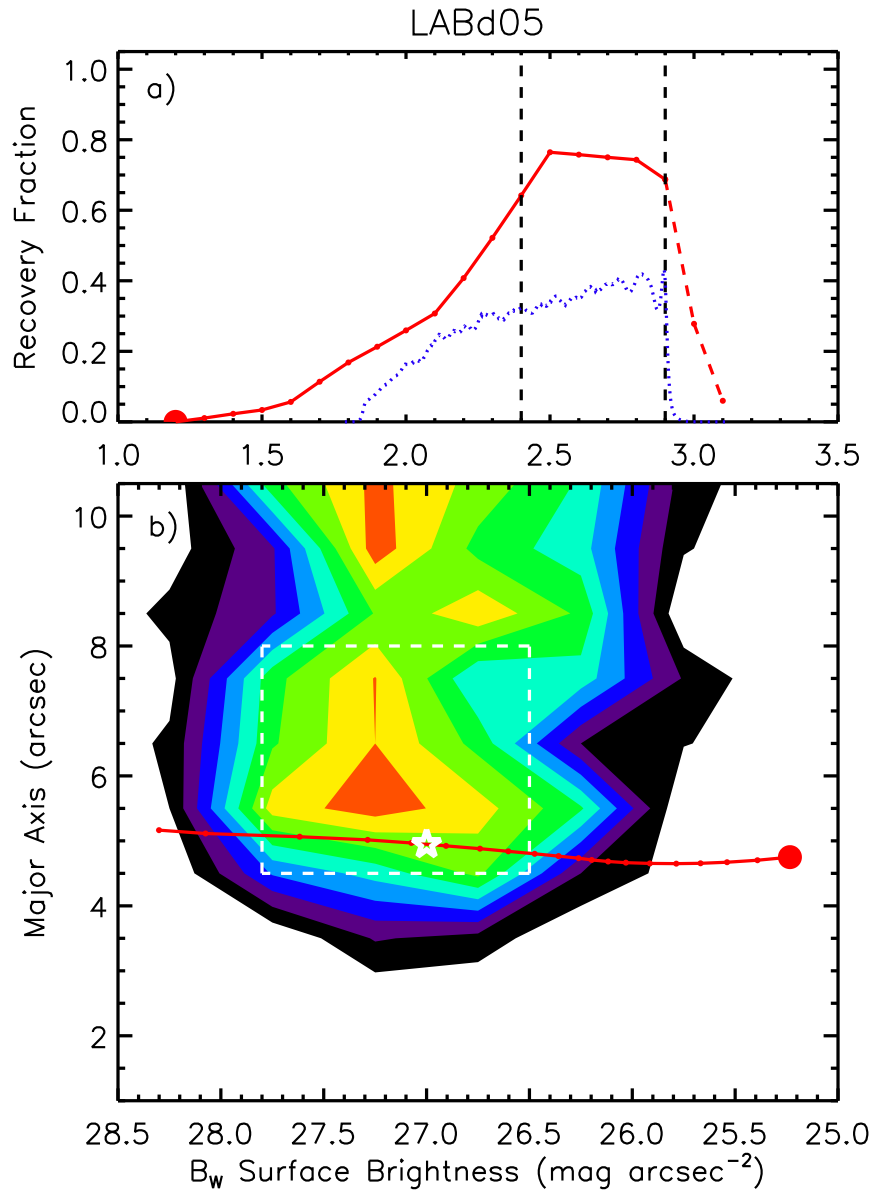


Figure 2.19 Same as Figure 2.15 but for LABd05.

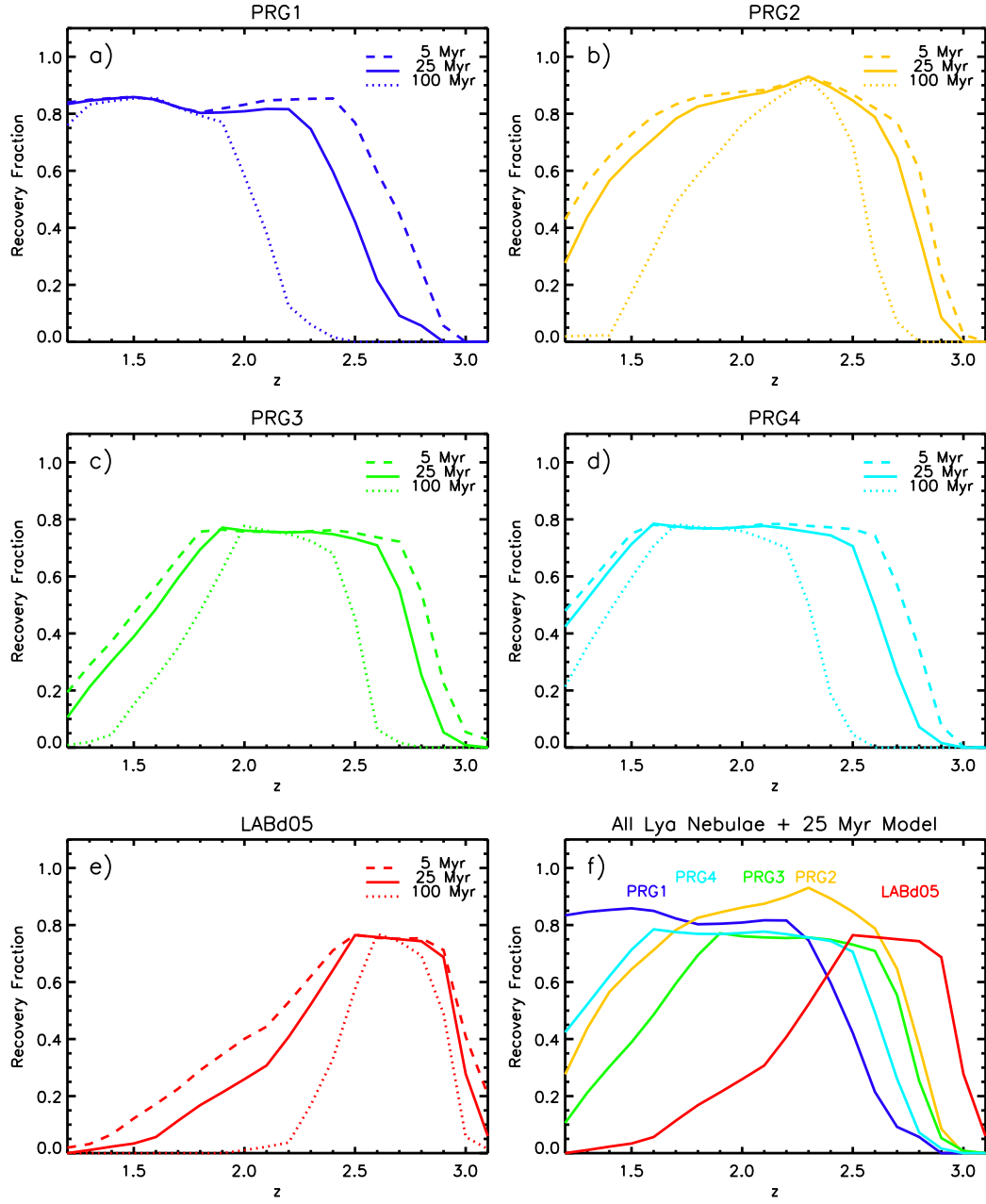


Figure 2.20 Recovery fractions as a function of redshift for all 5 sources using a range of continuum template ages (simple stellar population, 5, 25, 100 Myr, unreddened; Bruzual & Charlot, 2003). Panel (f) shows recovery fraction curves for all 5 sources using the 25 Myr model.

and replaced with sky noise during Steps 2-3 (high threshold star and galaxy rejection) of the search pipeline. The other two $\text{Ly}\alpha$ nebulae found in their survey (their Blobs 3 and 4) are AGN-dominated with even brighter central sources dominating the appearance in the broad-band imaging and suffer from the same treatment. We discovered two other core-halo $\text{Ly}\alpha$ nebula candidates using a deep 1 square degree intermediate-band imaging survey with Subaru (Chapter 3). The first (P10_4) has been confirmed to be a $\text{Ly}\alpha$ halo surrounding a pair of bright continuum sources at $z \approx 2.6$, one of which shows unambiguous AGN emission lines in the spectrum. The AGN is rejected during Steps 2-3 and the second central source is rejected during Steps 4-5 used for intermediate threshold star and galaxy rejection (Figure 2.21). Due to the large size and luminosity of the $\text{Ly}\alpha$ halo, the wings of the $\text{Ly}\alpha$ emission are detected in the B_W imaging, but on larger size scales and much weaker wavelet power limits than probed by the current survey. The second $\text{Ly}\alpha$ nebula candidate (P10_3, unconfirmed) has what we assume to be a faint $\text{Ly}\alpha$ halo (undetected in B_W) around a bright continuum sources, so it too is rejected during Steps 2-3. In all of these core-halo cases, the presence of a bright compact source near the center of faint $\text{Ly}\alpha$ emission makes it impossible for our broad-band search method to pick them out.

Our Subaru intermediate-band imaging survey also uncovered two $\text{Ly}\alpha$ nebulae candidates in the second morphological category (P10_1, confirmed, and P10_2). These sources do not have strong central sources, but in each case the diffuse emission is too faint to be detected by our search algorithm.

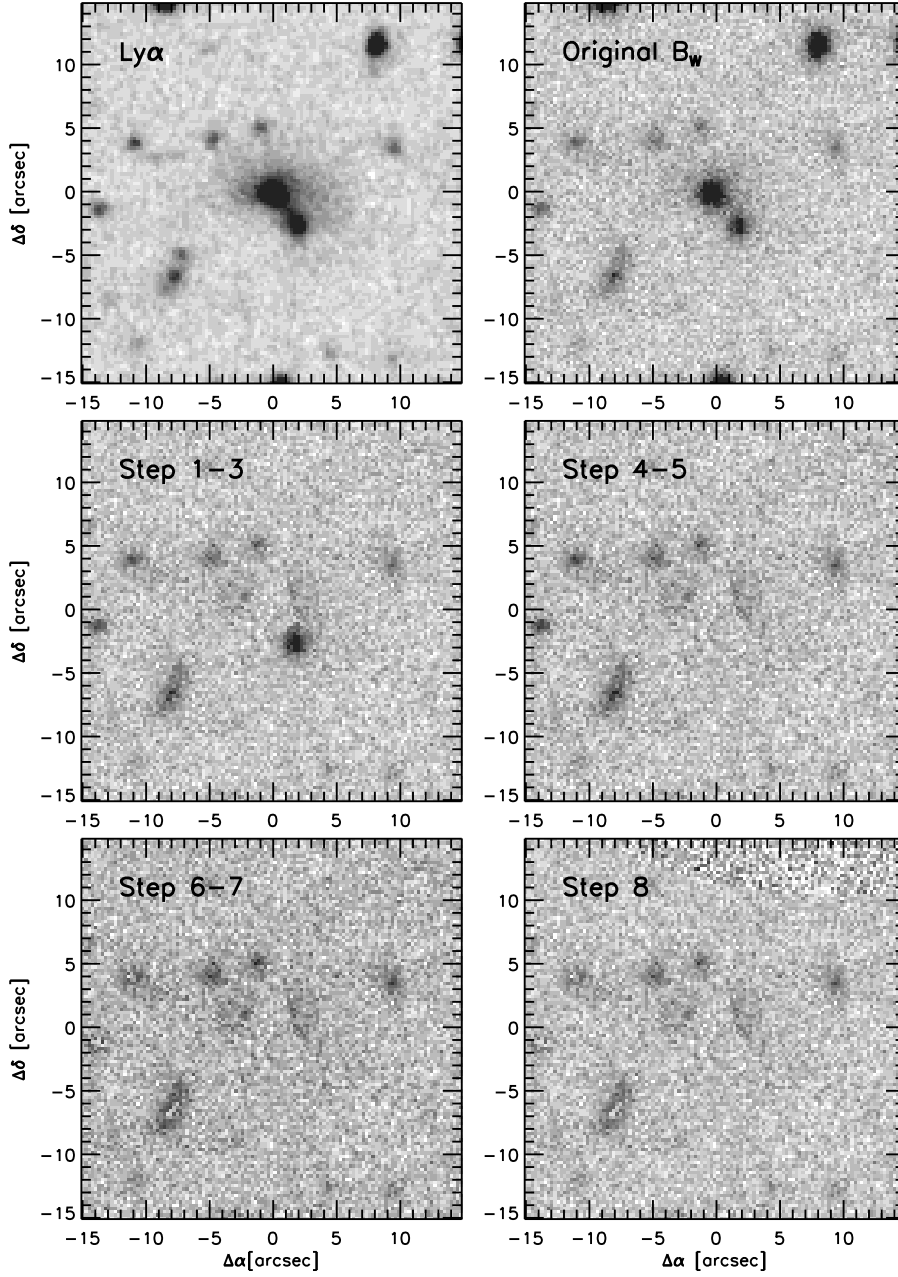


Figure 2.21 Ly α nebulae with a “core-halo” morphology are not selected by our search algorithm. In this example, the bright, compact, central sources seen in the Ly α and B_W imaging (upper two panels) are removed during the pipeline as discussed in the text (remaining panels). While some diffuse emission remains, it is too faint to be detected by the search algorithm.

Table 2.5. Other Known Ly α Nebulae in the Boötes Field

Source	Survey ^a	Redshift ^b	B_W Size (arcsec)	B_W Surface Brightness (mag arcsec ⁻²)	Notes ^c
P10_1	Prescott et al. (2010) - Subaru	2.7	1.2	27.1	Too Faint
P10_2	Prescott et al. (2010) - Subaru	-	2.0	26.7	Core-Halo
P10_3	Prescott et al. (2010) - Subaru	-	0.4	27.6	Too Faint
P10_4	Prescott et al. (2010) - Subaru	2.6	3.5	26.5	Core-Halo
P10_5	Prescott et al. (2010) - Mayall	1.9	2.6	27.0	Too Faint
Y09_1	Yang et al. (2009)	2.3	1.8	26.6	Core-Halo
Y09_2	Yang et al. (2009)	2.3	1.6	26.6	Core-Halo

^aSources selected from a Subaru intermediate-band survey (Prescott et al. 2010, in preparation) and a Mayall intermediate-band survey (Prescott et al. 2010, in preparation) are listed along with two Ly α nebulae from Yang et al. (2009).

^bSources without redshifts are Ly α nebulae candidates selected from intermediate-band Ly α imaging centered at $z \approx 2.7$ but have not yet been spectroscopically confirmed.

^c"Too Faint" indicates that only a small fraction of the source area exceeds the isophotal surface brightness threshold, causing the source to be missed by our survey. "Core-Halo" describes sources with a central compact continuum source surrounded by the Ly α halo; these sources are removed from the images during pipeline steps designed to remove bright stars and galaxies and are not selected by our survey.

2.6 Results

2.6.1 The Space Density of Large Ly α Nebulae

Our survey was designed to find sources from the large and bright end of the Ly α nebulae luminosity function, and is sensitive to diffuse, spatially extended blue sources with B_W sizes of > 37 kpc and B_W surface brightnesses of 26.5-27.8 mag arcsec $^{-2}$. The total redshift range of the survey spans from $z \approx 1.6$, where Ly α is no longer detectable with MMT/Blue Channel, to $z \approx 2.9$ when sources redshift out of the B_W filter. The total survey comoving volume is $1.38 \times 10^8 h_{70-3}$ Mpc 3 , by far the largest Ly α nebulae survey ever attempted. Within our survey volume, we found 5 Ly α nebulae — 1 previously known (Dey et al., 2005) and 4 newly-discovered. Due to selection and spectroscopic incompleteness, each of these sources represents a larger number of Ly α nebulae within the survey volume: $N_{total} = \sum_{i=1}^5 \frac{1}{f_{select,i}} \times \frac{1}{f_{spec,i}}$, where $f_{select,i}$ corrects for the fact that our survey does not select sources equally well across the full redshift window and $f_{spec,i}$ corrects for the fraction of Ly α nebula candidates that we were not able to target for follow-up spectroscopy. The selection incompleteness factors $f_{select,i}$ were determined by calculating the comoving volume-weighted recovery fraction for each Ly α nebula over $1.6 < z < 2.9$, using the redshift recovery fraction curves developed in Section 2.5.3. In doing this calculation, the recovery fraction is set to zero for redshifts where a source no longer meets the color cut $B_W - R < 0.65$. The spectroscopic incompleteness factor is $f_{spec,i} = N_{targets}/N_{candidates} = 0.38$ for sources in the high priority region and 0.13 for sources in the second priority region, where $N_{targets}$ and $N_{candidates}$ are the number of spectroscopic targets and total Ly α nebula candidates, respectively. The total number of Ly α nebulae

within our survey volume is $N_{total} = 30.9 \pm 16.0$, yielding a number density of $2.2 \pm 1.2 \times 10^{-7} h_{70}^3 \text{ Mpc}^{-3}$ for sources with B_W sizes of > 37 kpc. If we consider only the four brightest $\text{Ly}\alpha$ nebulae (with total $L_{\text{Ly}\alpha} \gtrsim 1.5 \times 10^{43} \text{ erg s}^{-1}$), the measured number density is $1.9 \pm 1.1 \times 10^{-7} h_{70}^3 \text{ Mpc}^{-3}$.

2.6.2 Sources of Uncertainty

Thanks to the enormous volume of our survey, cosmic variance is not a substantial contribution to the uncertainty in our number density estimate ($1 - 2\%$; Trenti & Stiavelli, 2008). Instead, the main source of uncertainty in this estimate is the effect of morphology. $\text{Ly}\alpha$ nebulae are complex sources, some with a bright compact central continuum source embedded within the $\text{Ly}\alpha$ cloud, others with a predominantly diffuse morphology. As discussed in Section 2.5.4, cases with a strong central source are not selected by our survey, whereas they are easily selected by traditional narrow-band approach. Since the fraction of $\text{Ly}\alpha$ nebulae with this morphology is unknown, it is difficult to assess the impact of this aspect of our survey design. Within a 1 square degree intermediate-band $\text{Ly}\alpha$ imaging survey that overlaps the NDWFS Boötes field, we know there are three bright $\text{Ly}\alpha$ nebulae (P10.2, P10.4, and LABd05 in Table 2.5) — one, LABd05, has a predominantly diffuse morphology while the other two have a core-halo morphology that removes them from our survey, as discussed in Section 2.5.4. If this is representative of the class as a whole, this would imply that a factor of 3 correction should be applied to our number density estimate: $\approx 5.8 \times 10^{-7} h_{70}^3 \text{ Mpc}^{-3}$. We discuss this point further in Section 2.7.2.

2.7 Discussion

2.7.1 A Broad-band Ly α Nebula Survey

This work has shown that it is possible to find large Ly α nebulae using deep broad-band imaging data. There are many advantages to this unusual approach. The rarity of Ly α nebulae necessitates surveys that cover enormous comoving volumes, a requirement which is observationally expensive when using a narrow-band filter. A narrow-band survey using a 100Å filter at $z \approx 2.3$ would need to search over 100 square degrees to reach the same comoving volume covered in our broad-band survey. Our technique builds on existing deep datasets, requiring much less observational overhead. Our survey is also completely unbiased in terms of environment. The early, successful Ly α surveys often targeted known overdensities and were limited to smaller areas (Steidel et al., 2000; Matsuda et al., 2004; Francis et al., 1996; Palunas et al., 2004), introducing a bias to the number density estimate. By contrast, our 9 square degree survey spans a $\Delta z \approx 1.3$ covers a comoving transverse distance of $\approx 290 h_{70}^{-1}$ Mpc (at the redshift midpoint, $z \approx 2.25$) and a comoving line-of-sight distance of $\approx 1700 h_{70}^{-1}$ Mpc.

The drawbacks of using broad-band data to select line-emitting sources stem from the need to restrict our search to the largest Ly α nebulae in order to reduce the number of contaminants. While our survey does not have a formal equivalent width limit, to be selected a source must be bright in terms of total B_W (line+continuum) flux. Thus, smaller and fainter Ly α nebulae are not easily found with this technique. In addition, as discussed in Section 2.5.4, Ly α nebulae with a “core-halo” morphology, in which the Ly α forms a halo around a bright, compact continuum source, are not selected in our survey.

2.7.2 Comparisons to Other Surveys

This Ly α nebula survey is fundamentally different and complementary to standard narrow-band surveys. Our survey design is primarily a morphology-based selection — searching for diffuse, spatially extended sources in the B_W band — and is less biased to high Ly α equivalent widths due to the broad B_W filter. By contrast, narrow-band surveys are highly sensitive to the Ly α equivalent width of a source and are much less affected by morphology (Section 2.5.4).

Due to the unique nature of our survey, it is difficult to compare our measured number density directly with measurements from narrow-band Ly α surveys. After generating a catalog of narrow-band sources, a standard narrow-band survey will first apply a color-excess cut, selecting sources with excess flux in the narrow-band relative to a nearby broad-band, in order to find line-emitting candidates above a certain Ly α equivalent width ($W_{Ly\alpha,nb}$). The final Ly α nebula candidate sample is then derived by selecting only those sources in the color-excess sample that are larger than a certain Ly α size ($\theta_{Ly\alpha,nb}$) and brighter than a certain Ly α luminosity ($L_{Ly\alpha,nb}$). The number density can then be quoted as $n_{Ly\alpha,nb}$ for Ly α nebulae with $W > W_{Ly\alpha,nb}$, $\theta > \theta_{Ly\alpha,nb}$, and $L_{Ly\alpha} > L_{Ly\alpha,nb}$ (e.g., Yang et al., 2009), or for sufficiently large samples, a Ly α luminosity function can be constructed (e.g., Saito et al., 2006). At the conclusion of our survey, on the other hand, we have a sample of Ly α nebulae for which we know the Ly α equivalent widths and Ly α luminosity within a spectroscopic slit, and the total size and surface brightness of the source in the B_W image. Without a narrow-band image or more extensive spectroscopy, we do not know the total Ly α luminosity nor the full Ly α size, both of which are needed for a direct comparison to narrow-band number density results.

Very approximate estimates of the total $\text{Ly}\alpha$ luminosity and $\text{Ly}\alpha$ size can be derived by assuming that $\text{Ly}\alpha$ traces the emission in the B_W image. We scale the $\text{Ly}\alpha$ luminosity measured within the spectroscopic slit using the ratio of the measured size of the source in the B_W image to the aperture size and by the ratio of the $\text{Ly}\alpha$ and B_W sizes as measured within the slit. The $\text{Ly}\alpha$ size measurements were estimated down to a surface brightness limit of $\approx 7 \times 10^{-18} \text{ erg s}^{-1} \text{ cm}^{-2} \text{ arcsec}^{-2}$ ($\approx 3.2 \times 10^{-18} \text{ erg s}^{-1} \text{ cm}^{-2} \text{ arcsec}^{-2}$ for PRG1 at $z \approx 1.67$), which is roughly equal to that used in Yang et al. (2009). The resultant values are listed in Table 2.4. The total $\text{Ly}\alpha$ luminosities of our sample of $\text{Ly}\alpha$ nebulae are in the range $\approx 0.2 - 12 \times 10^{43} \text{ erg s}^{-1}$ and the $\text{Ly}\alpha$ sizes are $\approx 30\text{-}45 \text{ arcsec}^2$. These are almost certainly underestimates of the true $\text{Ly}\alpha$ luminosity and $\text{Ly}\alpha$ size, but it is instructive to make the comparison to other surveys none the less.

To compare with the results of other surveys, we follow Yang et al. (2009) and compute the number density of the 4 sources in our sample with $\text{Ly}\alpha$ luminosities greater than a $\text{Ly}\alpha$ luminosity limit of $(1.5 \times 10^{43} \text{ erg s}^{-1}) - 1.9 \pm 1.1 \times 10^{-7} h_{70}^{-3} \text{ Mpc}^3$ over $1.6 < z < 2.9$. Given that all 4 of these sources are larger than 30 arcsec^2 we recompute the Yang et al. (2009) number density estimate to what it would be for this size threshold ($1.2 \times 10^{-6} h_{70}^3 \text{ Mpc}^{-3}$ at $z \approx 2.3$). The estimate from Saito et al. (2006) for sources above this $\text{Ly}\alpha$ luminosity is an order of magnitude higher ($\lesssim 6.7 \times 10^{-6} h_{70}^3 \text{ Mpc}^{-3}$) at $z \approx 4$ while that from Ouchi et al. (2009) is $\sim 1.2 \times 10^{-6} h_{70}^3 \text{ Mpc}^{-3}$ at $z \approx 6.6$. The number density comparison is shown in Figure 2.22.

Despite the uncertainties, it is clear that our derived number density is roughly an order of magnitude lower than that derived using systematic narrow-band studies (Saito et al., 2006; Ouchi et al., 2009; Yang et al., 2009). This discrepancy could be due to a number of factors. First, we know that our survey is insen-

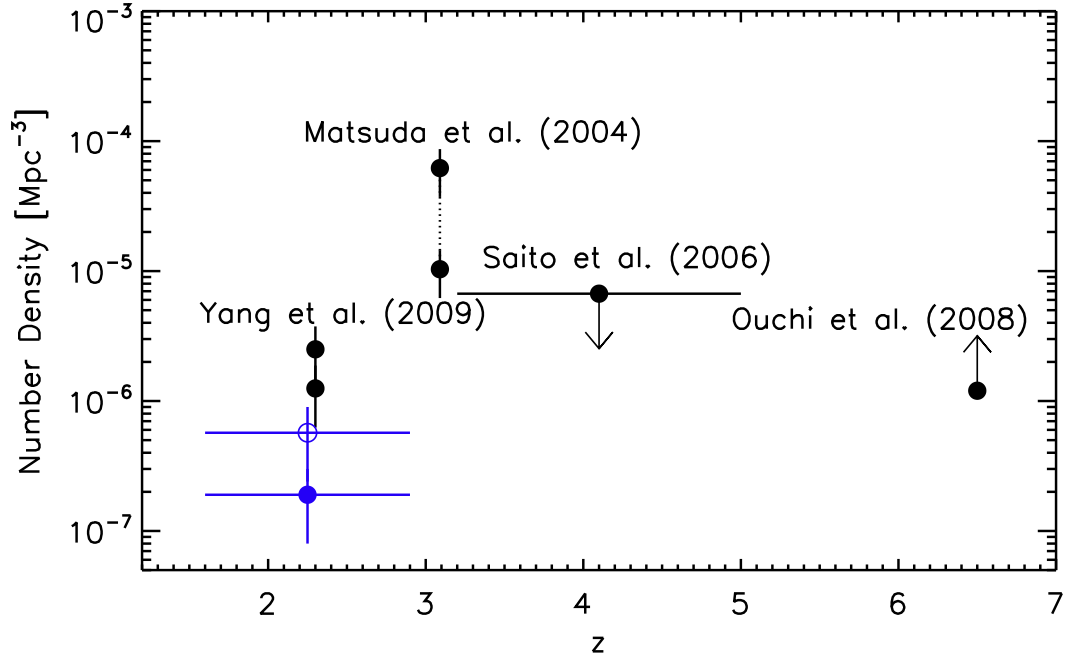


Figure 2.22 The $\text{Ly}\alpha$ number density measured by our broad-band survey (blue points) compared with that from narrow-band surveys (black points; Yang et al., 2009; Matsuda et al., 2004; Saito et al., 2006; Ouchi et al., 2008). The comparison between broad-band and narrow-band surveys is complicated by a number of factors, as discussed in Section 2.7.2. The lower point from our survey (filled blue circle) is the measured number density; the upper value (blue open circle) includes an approximate morphology correction. The upper value shown for Yang et al. (2009) is the final number density they derive; the lower value represents the value for non-AGN-dominated $\text{Ly}\alpha$ nebulae only.

sitive to $\text{Ly}\alpha$ nebulae with a core-halo morphology, which means our number density estimate should be boosted by some factor to represent all $\text{Ly}\alpha$ nebulae. A factor of at least 10 would be required to explain the discrepancy between our value and that of Yang et al. (2009), but this seems unlikely given what we know about the small sample of large $\text{Ly}\alpha$ nebulae discovered to date. For example, for sources with $\text{Ly}\alpha$ luminosity $> 1.5 \times 10^{43} \text{ erg s}^{-1}$ within the Matsuda et al. (2004) survey, roughly 5 out of 9 appear to have a strong compact continuum source in the center. The $\text{Ly}\alpha$ nebulae found by Nilsson et al. (2006), Smith & Jarvis (2007), and Ouchi et al. (2009) do not appear to have the core-halo morphology, while all 4 cases found by Yang et al. (2009) do. These fractions point towards a factor of 2-3 correction. Similarly, in Section 2.6.2 we discussed the comparison of our survey with that of an overlapping $\text{Ly}\alpha$ survey at $z \approx 2.7$, which suggests that the correction for core-halo $\text{Ly}\alpha$ nebulae is roughly a factor of 3. We note, however, that it is not clear whether these two morphological classes should in fact be considered together, since the core-halo morphology will in some cases host an unobscured AGN and may indicate different powering mechanisms or a more mature system.

A second consideration is the effects of cosmic variance. While cosmic variance is not the dominant source of noise in our survey, it will cause scatter in number density estimates derived from smaller survey volumes. If we assume our number density estimate (or apply a factor of 3 “morphology correction”) the calculated cosmic variance for a survey similar to Yang et al. (2009) is a factor of 2.8 (1.7). Thus, cosmic variance alone cannot account for the discrepancy in our number density estimates, but it is likely a contributing factor.

Finally, in this comparison we may inadvertently be comparing different pop-

ulations of $\text{Ly}\alpha$ nebulae due to the fact that our total $\text{Ly}\alpha$ luminosity and size estimates are very approximate. Since we are working at the steep end of the luminosity function a small change in the luminosity estimate will have a substantial effect on the number density. For one $\text{Ly}\alpha$ nebula for which we have intermediate-band $\text{Ly}\alpha$ imaging, we find that approximate $\text{Ly}\alpha$ luminosities and sizes are underestimated by roughly 30%. If this is true in general, our number density estimates are appropriate for larger and brighter $\text{Ly}\alpha$ nebulae, which we expect to be rarer. Indeed, Yang et al. (2009) note that their survey suggests $\text{Ly}\alpha$ nebulae larger and more luminous than their sample have a number density of $< 5 \times 10^{-7} h_{70}^3 \text{ Mpc}^{-3}$, which is consistent with our measurement after including the morphology correction.

We suspect that all three of these factors — morphology, cosmic variance, and luminosity/size underestimates - contribute to the discrepancy between our number density estimate and those of smaller volume surveys. Two of these factors (morphology and luminosity/size underestimates) will tend to increase our number density measurement, while cosmic variance will decrease the number density estimates from smaller volume surveys. Our $\text{Ly}\alpha$ nebula survey provides the first strong lower limit on the space density of $\text{Ly}\alpha$ nebulae. Deep narrow-band imaging of our sample of $\text{Ly}\alpha$ nebulae will be required to measure the total $\text{Ly}\alpha$ luminosity and $\text{Ly}\alpha$ size measurements of our 5 $\text{Ly}\alpha$ nebulae and to perform a robust comparison with other surveys.

2.7.3 Host Dark Matter Halos

The idea that large $\text{Ly}\alpha$ nebulae should be so rare is not surprising, given the emerging consensus that $\text{Ly}\alpha$ nebulae are found in the highest density regions. The largest $\text{Ly}\alpha$ nebulae have been shown to be strongly associated with over-

densities (e.g., Chapter 3); comparisons with the Millennium Simulation suggest that the overdensity hosting LABd05 is in fact the largest it would be possible to observe, given the relatively large filter bandpass used in the study ($\Delta\lambda \approx 201 \text{ \AA}$; Prescott et al., 2008). With a number of examples of multiple $\text{Ly}\alpha$ nebulae located within a small region, we have independent evidence that $\text{Ly}\alpha$ nebulae are a highly clustered phenomenon (Steidel et al., 2000; Matsuda et al., 2004; Palunas et al., 2004; Yang et al., 2009).

If we assume that all dark matter halos above a given minimum mass have $\text{Ly}\alpha$ nebulae, we can use our number density measurement to estimate the mass of these host halos. Λ CDM simulation predictions for the dark matter halo mass function at $z \approx 2 - 3$ predict that halos of mass $\sim 1.3 \times 10^{14} h_{70}^{-1} M_{\odot}$ have number densities similar to our original value; the estimate is $\sim 0.9 \times 10^{14} h_{70}^{-1} M_{\odot}$ if we apply the factor of 3 “morphology correction” (Trenti & Stiavelli, 2008). If $\text{Ly}\alpha$ nebulae require certain conditions not found in all halos (a filling factor) or have a duty cycle less than unity, that will lower the dark matter halo mass. For example, a duty cycle or filling factor of 0.1 translates into a minimum halo mass of $6.0 \times 10^{13} h_{70}^{-1} M_{\odot}$ ($3.8 \times 10^{13} h_{70}^{-1} M_{\odot}$ for the morphology-corrected value). The number density derived by Yang et al. (2009) corresponds to slightly lower minimum halo masses of $4.7 \times 10^{13} h_{70}^{-1} M_{\odot}$ ($1.5 \times 10^{13} h_{70}^{-1} M_{\odot}$ for a duty cycle of 0.1). For comparison, at $z \approx 3$ LBGs and LAEs reside in $\sim 10^{11} M_{\odot}$ halos (Adelberger et al., 2005; Gawiser et al., 2007); red star-forming or passively evolving BzK-selected galaxies are found in 10^{12} - $10^{13} M_{\odot}$ mass halos (Blanc et al., 2008). $\text{Ly}\alpha$ nebulae are a highly unusual phenomenon and live in much more massive halos than other well-studied galaxy populations. A $10^{14} M_{\odot}$ dark matter halo at $z \approx 2$ will evolve into a $\sim 5 \times 10^{13} - 10^{15} h_{70}^{-1} M_{\odot}$ halo at $z = 0$ (McBride et al., 2009).

Thus it seems clear that $\text{Ly}\alpha$ nebulae reside in the most massive dark matter halos at high redshifts and likely evolve into the most massive structures in the local universe.

2.8 Conclusions

We have designed an innovative systematic search for large $\text{Ly}\alpha$ nebulae using deep broad-band data. While our technique is only sensitive to the largest and brightest $\text{Ly}\alpha$ nebulae (B_W sizes > 37 kpc and surface brightnesses $SB = 26.5 - 27.8$ AB mag arcsec $^{-2}$), it is able to probe enormous comoving volumes ($1.4 \times 10^8 h_{70}^{-3} \text{ Mpc}^3$) using existing deep broad-band datasets. Within our ~ 9 square degree survey area and a redshift range of $z \approx 1.6 - 2.9$ we recovered 1 previously known $\text{Ly}\alpha$ nebula and 4 newly-discovered cases. The brightest 4 $\text{Ly}\alpha$ nebulae have $\text{Ly}\alpha$ luminosities of $\sim 2 - 12 \times 10^{43} \text{ erg s}^{-1}$ and sizes $> 60 \text{ kpc}$. The results of this search provide the first strong lower limit on the $\text{Ly}\alpha$ nebula number density of $\approx 1.9 \times 10^{-7} h_{70}^3 \text{ Mpc}^{-3}$. This is comparable to the number density of $\sim 10^{14} M_\odot$ mass halos.

CHAPTER 3

THE OVERDENSE ENVIRONMENT OF A LARGE $\text{Ly}\alpha$ NEBULA AT $z \approx 2.7$

Large nebulae ($\gtrsim 50$ kpc) emitting strongly in $\text{Ly}\alpha$ (also known as $\text{Ly}\alpha$ “blobs”) are likely signposts of ongoing massive galaxy formation. The relative rarity of these sources and their discovery in well-studied galaxy overdensities suggest that they may be associated with regions of high galaxy density. One of the largest $\text{Ly}\alpha$ nebulae, discovered at a redshift of $z \approx 2.7$ via its strong mid-infrared emission, provides an unbiased test of this association. We have carried out a deep intermediate-band imaging survey for $\text{Ly}\alpha$ -emitting galaxies (LAEs) within a $30' \times 26'$ field of view around this $\text{Ly}\alpha$ nebula. This is the first study of the environment of a $\text{Ly}\alpha$ nebula found without a priori knowledge of its surroundings. We find that the nebula is located in an overdense region, at least $20 \times 50 \text{ h}_{70}^{-1}$ comoving Mpc in size, showing a factor of ~ 3 LAE number density enhancement relative to the edge of the field. Given the predicted number of such overdensities, we rule out the possibility of a chance coincidence at the $\lesssim 1\%$ level. This study, in conjunction with previous work, provides strong confirmation of the association between the largest $\text{Ly}\alpha$ nebulae and overdense regions of the Universe.

3.1 Introduction

Studies of massive galaxy populations show that the most massive galaxies are in place and in possession of the majority of their stellar mass by $z \sim 1 - 2$ (Mc-

This chapter originally appeared in Prescott, M. K. M., Kashikawa, N., Dey, A., & Matsuda, Y. 2008, *ApJL*, 678, L77.

Carthy et al., 2004; van Dokkum et al., 2004; Daddi et al., 2005; Bundy et al., 2005; Brown et al., 2007). Thus, while dark matter halos in a Λ CDM cosmology build up hierarchically with the gradual accretion and merging of smaller halos, the most massive galaxies within that context likely have more dramatic origins. The details of this process are uncertain, and ideally we would like to study sites of ongoing massive galaxy formation. $\text{Ly}\alpha$ nebulae or $\text{Ly}\alpha$ “blobs” (LABs) – large ($\gtrsim 50$ kpc) clouds of gas emitting strongly in $\text{Ly}\alpha$ ($\sim 10^{44}$ erg s $^{-1}$) – provide such an opportunity. The large $\text{Ly}\alpha$ equivalent widths and the association with galaxy populations such as Lyman break galaxies (LBGs) and submillimeter galaxies (SMGs) strongly suggest that LABs are sites of ongoing galaxy formation. They have been found in small numbers (only 16 $\gtrsim 50$ kpc LABs are known) around $z \sim 2-3$, a key epoch of black hole and galaxy growth (Steidel et al. 2000, hereafter S00; Francis et al. 2001; Palunas et al. 2004; Matsuda et al. 2004; Dey et al. 2005; Nilsson et al. 2006; Smith & Jarvis 2007; Greve et al. 2007). LABs span a range in size and surface brightness from the scales of $\text{Ly}\alpha$ -emitting galaxies (LAEs) to the largest LABs known (~ 150 kpc, ~ 27 mag arcsec $^{-2}$; e.g., Matsuda et al., 2004). LABs are similar to the large $\text{Ly}\alpha$ halos observed in the overdensities around higher redshift radio galaxies (e.g., Venemans et al., 2007; Overzier et al., 2008) but are found in radio quiet environments. The dominant power source in LABs is difficult to determine; among the limited sample of large LABs, there is evidence for embedded AGN, starburst-driven superwinds, gravitational cooling radiation, and spatially-extended star formation, all of which may play a role in powering the $\text{Ly}\alpha$ emission (Prescott et al. 2008, in preparation; S00; Chapman et al. 2004; Nilsson et al. 2006; Taniguchi & Shioya 2000; Matsuda et al. 2004; Dey et al. 2005; Matsuda et al. 2007).

Most known LABs, including two of the largest cases, have been discovered via narrow-band surveys, often by targeting known galaxy overdensities (S00; Francis et al. 2001; Palunas et al. 2004; Matsuda et al. 2004). Follow-up narrow-band imaging of the SSA22 region surrounding the S00 LABs revealed fainter LABs associated with the same overdensity traced by the LAEs (Matsuda et al., 2004). This suggests that LABs may be confined to overdense regions, as would be expected for sites of massive galaxy formation. A blank field survey by Saito et al. (2006) supported this claim, finding no LABs with sizes greater than ~ 30 kpc and an order of magnitude lower number density of LABs relative to that found within the SSA22 galaxy overdensity. However, the association between LABs and galaxy overdensities may be misleading, as a truly systematic wide-area search has yet to be completed. A thorough environmental study has only been done for the S00 LABs, which were found by targeting a known galaxy overdensity.

In contrast, one of the largest LABs uncovered recently was found by entirely different means. While conducting a study of mid-infrared ($24\mu\text{m}$) sources detected by the *Spitzer Space Telescope*, Dey et al. (2005) discovered a LAB at $z = 2.656$ within the NOAO Deep Wide-Field Survey Boötes field (NDWFS¹; Jannuzi & Dey, 1999). Follow-up observations revealed complexity typical of the LAB class: the region hosts a buried AGN, many young galaxies, an LBG, and diffuse HeII and continuum emission suggestive of spatially-extended star formation (Prescott et al. 2008, in preparation). One of the largest and most luminous LABs known, and found without any a priori knowledge of its surroundings, this

¹This research draws upon data provided by Dr. Buell Jannuzi and Dr. Arjun Dey as distributed by the NOAO Science Archive.

source represents a unique opportunity to perform an unbiased, complementary test of the association between LABs and overdense regions.

In this work, we present the first results from an ongoing deep intermediate-band Ly α imaging survey of the environment of the Dey et al. (2005) LAB (hereafter, LABd05) and report on the spatial distribution of the LAEs in the immediate vicinity. A detailed analysis of the multiwavelength properties of LABd05 and the properties and clustering of the LAEs in the region will be presented by Prescott et al. (2009, in preparation). We assume the standard Λ CDM cosmology ($\Omega_M=0.3$, $\Omega_\Lambda=0.7$, $h=0.7$); the angular scale at $z = 2.656$ is 7.96 kpc/'. All magnitudes are in the AB system.

3.2 Observations & Reductions

We obtained deep imaging of the field around LABd05 using the Subaru telescope and the SuprimeCam imager (Miyazaki et al., 2002) on U.T. 2007 May 10-14 and June 17. The survey covers 0.22 deg² in an intermediate-band filter, IA445 ($\lambda_c \approx 4458\text{\AA}$, $\Delta\lambda_{FWHM} \approx 201\text{\AA}$), centered on the Ly α line at the redshift of the nebula; this corresponds to a comoving volume of $4.27 \times 10^5 h_{70}^{-3} \text{ Mpc}^3$ ($52 \times 45 \times 180 h_{70}^{-1} \text{ Mpc}$). Conditions during the May observations were variable (clouds, variable seeing 0.7''-1.2'') and good in June (clear with 0.7'' seeing). We obtained a total of 3 hours of observations.

We reduced the data using the SDFRED software (Yagi et al., 2002; Ouchi et al., 2004). The data were overscan-subtracted and corrected for geometric and atmospheric distortions. We generated the sky flat using object frames that were free of bright stars in combination with other images taken in the same intermediate-band filter (Y. Taniguchi, private communication). Small portions of the Suprime-

Cam field of view are vignetted by the autoguider probe; the affected areas were masked, as were bad columns, bright star ghosts, and satellite trails. Images were aligned and scaled using common stars and then combined using a clipped mean algorithm, which successfully removed cosmic rays. Of the SuprimeCam field-of-view (0.26 deg^2), 73% was usable (the remainder being of lower signal-to-noise along the edge of the field or in the vicinity of bright stars).

The limiting magnitude of the stacked image is 28.3 AB mag (1σ , $2''$ diameter aperture), calculated using 10,000 random apertures. An approximate magnitude zeropoint was calculated from observations of the standard stars BD+25d4655 and Feige 34. For the NDWFS broad-band imaging, the limiting magnitudes are $B_W^{\text{limit}}=27.9 \text{ mag}$, $R^{\text{limit}}=27.1 \text{ mag}$, $I^{\text{limit}}=26.0 \text{ mag}$ (1σ , $2''$ diameter aperture).

A portion of the field was observed in a custom U -band filter (U_d ; $\lambda \approx 3590 \text{ \AA}$, $\Delta\lambda_{FWHM} \approx 116 \text{ \AA}$) using the Mayall 4m Telescope over 6 nights (U.T. 2007 June 8-13). These data will be described elsewhere (Prescott et al. 2008, in preparation) but here provide a useful check on interlopers in our $z \approx 2.7$ LAE sample.

3.3 Ly α -Emitting Galaxy Candidate Selection

We used Source Extractor (Bertin & Arnouts, 1996) to select a sample of $\approx 38,600$ sources detected in the $IA445$ band down to the 5σ limit of $IA445=26.5 \text{ mag}$ ($2''$ diameter aperture; $L_{IA445}(z = 2.656)=1.5 \times 10^{42} \text{ erg s}^{-1}$) with the following search parameters: at least 5 contiguous pixels, a threshold of 2σ per pixel, and a Gaussian filter matched to the seeing ($FWHM \approx 0.8 \text{ arcsec}$). We measured matched aperture photometry using $2''$ diameter apertures from the $IA445$, B_W , R , and I imaging datasets, which were registered and resampled to match the B_W astrometry and pixel scale (0.258 arcsec/pix). Aperture corrections were neglected

(≈ 1.08 for an unresolved source). Line-emitting sources are strongly detected in $IA445$ relative to B_W , i.e., they have large negative $IA445 - B_W$ colors relative to the normal galaxy locus (see Figure 3.1). We removed bright stars ($IA445 \leq 25.0$) using the CLASS_STAR parameter in Source Extractor (> 0.91) and employed a cut of $IA445 - B_W \leq -0.85$ mag yielding 1500 candidates. Shifting the $IA445 - B_W$ cut by ± 0.2 mag causes no significant change to the main results presented in Section 4. For a $F_\nu \propto \nu^0$ continuum source, this corresponds to an observed equivalent width (EW) cut of $W_{obs} \geq 148 \text{ \AA}$. LAEs are known to be young, with estimated ages of 4-200 Myr (Finkelstein et al., 2007; Lai et al., 2008; Gawiser et al., 2007). For the case of a young galaxy (25 Myr old simple stellar population, solar metallicity, Chabrier IMF; Bruzual & Charlot, 2003; Tremonti et al., 2004) at $z = 2.7$ with standard intergalactic absorption (Madau, 1995), this is equivalent to a rest-frame EW cut of $W_{rest} \geq 50 \text{ \AA}$.

We expect our LAE candidate sample to be contaminated by high EW, low-redshift [OII] $\lambda\lambda 3727, 3729$ -emitting galaxies at $z \approx 0.2$. Since the $IA445$ bandpass lies on the red side of the B_W filter (Figure 3.1, see inset), we also expect contamination from higher redshift galaxies ($z \gtrsim 2.9 - 4.0$) for which the Lyman limit has entered the B_W filter, thus depressing the B_W flux relative to the $IA445$ flux. Using the publicly available NDWFS imaging (Jannuzi & Dey, 1999), we employ a cut of $B_W - R \leq 0.8$ to remove both contaminant populations (see Figure 3.2). The final sample of 785 LAE candidates corresponds to a mean LAE surface density of $\approx 4200 \text{ deg}^{-2}$. The properties and sizes of the LAE sample will be discussed in an upcoming paper (Prescott et al. 2008, in preparation). There are no other large ($\gtrsim 50 \text{ kpc}$) LABs in the vicinity of LABd05.

Sources at these redshifts should show very little flux in the U_d -band, which

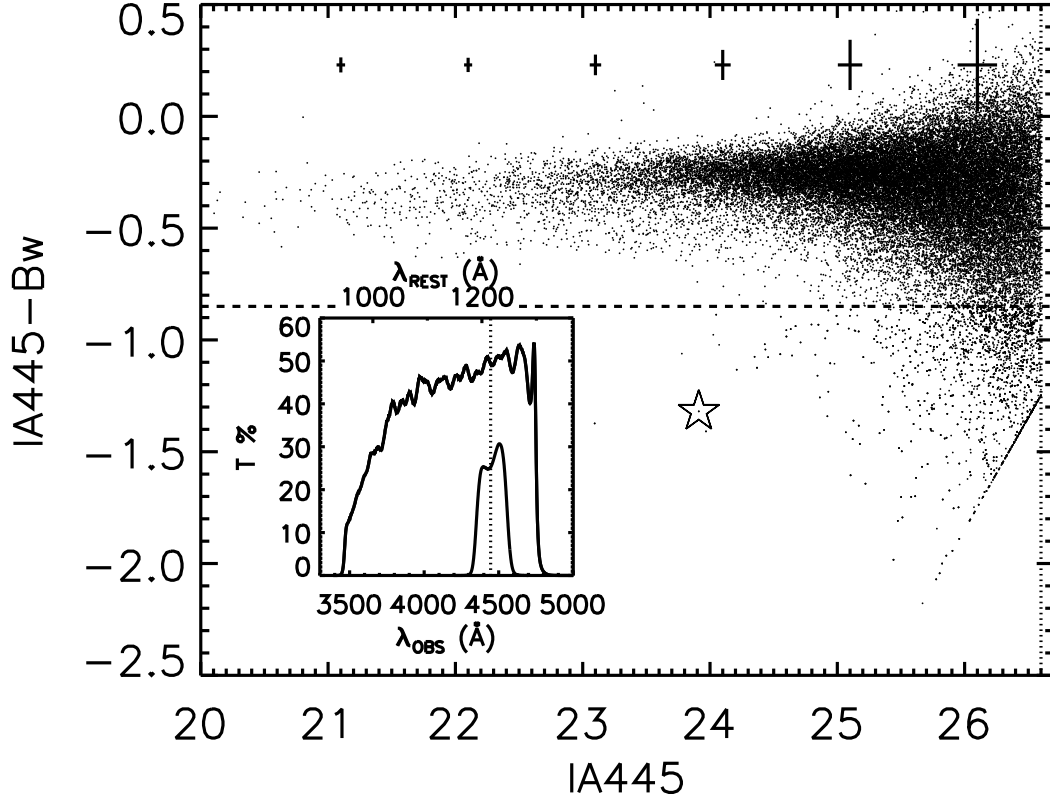


Figure 3.1 $IA445-B_W$ color-magnitude diagram for sources detected in the $IA445$ image (dots). Initial candidates were selected to meet the color cut $IA445-B_W \leq -0.85$ (dashed line, which corresponds to an observed equivalent width of $W_{obs} \geq 148\text{\AA}$) and to be brighter than the 5σ limiting magnitude in $IA445$ band ($IA445_{5\sigma,limit}=26.6$; dotted line). LABd05 is shown as a star, and non-detections in the B_W band are set to the B_W limiting magnitude. Typical error bars are shown. The inset shows the effective transmission curves for the B_W and $IA445$ filters and the wavelength of $\text{Ly}\alpha$ at the redshift of the system (dotted line).

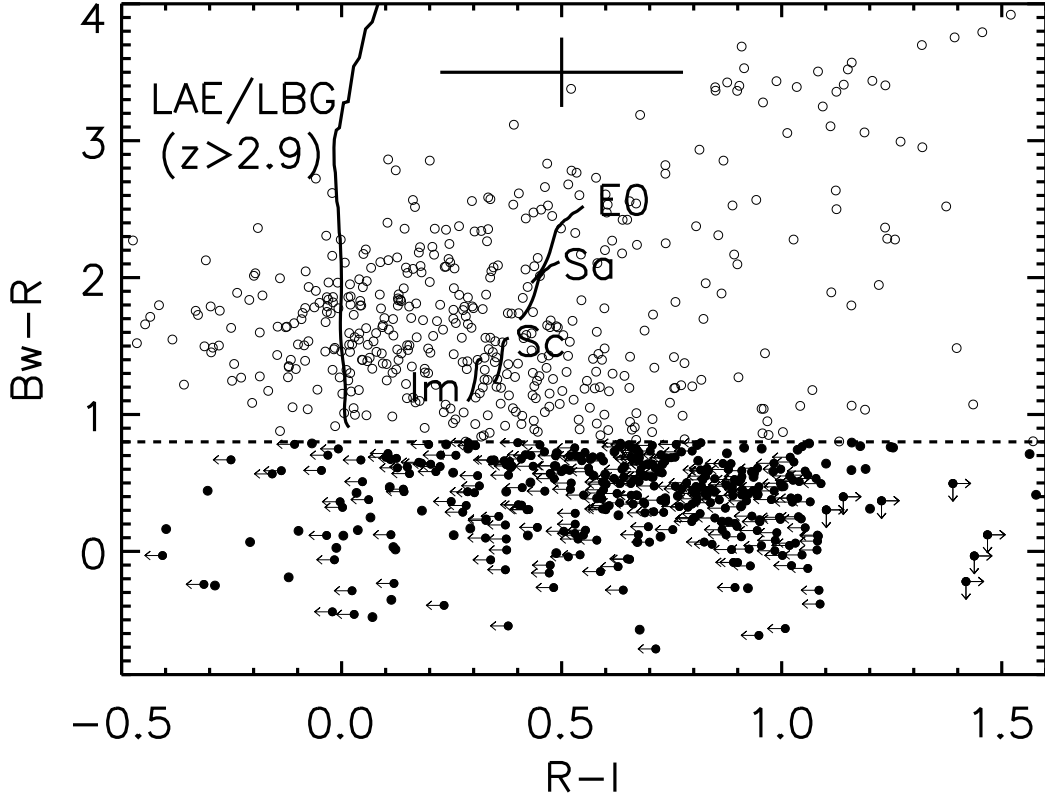


Figure 3.2 $B_W - R$ vs. $R - I$ color-color diagram of the 1500 line-emitting candidates (open and filled circles). A typical error bar is shown. Expected color tracks for low redshift galaxy templates are shown for $0.1 < z < 0.3$ (Leitherer et al., 1996); the color track for high redshift LAE/LBG contaminants is based on a young galaxy template at $2.9 < z < 4.0$ (25 Myr old simple stellar population, solar metallicity, Chabrier IMF; Bruzual & Charlot, 2003) with standard intergalactic absorption (Madau, 1995). To remove both low and high redshift interlopers, candidates were required to have $B_W - R \leq 0.8$. The final sample of 785 LAE candidates is shown (filled circles).

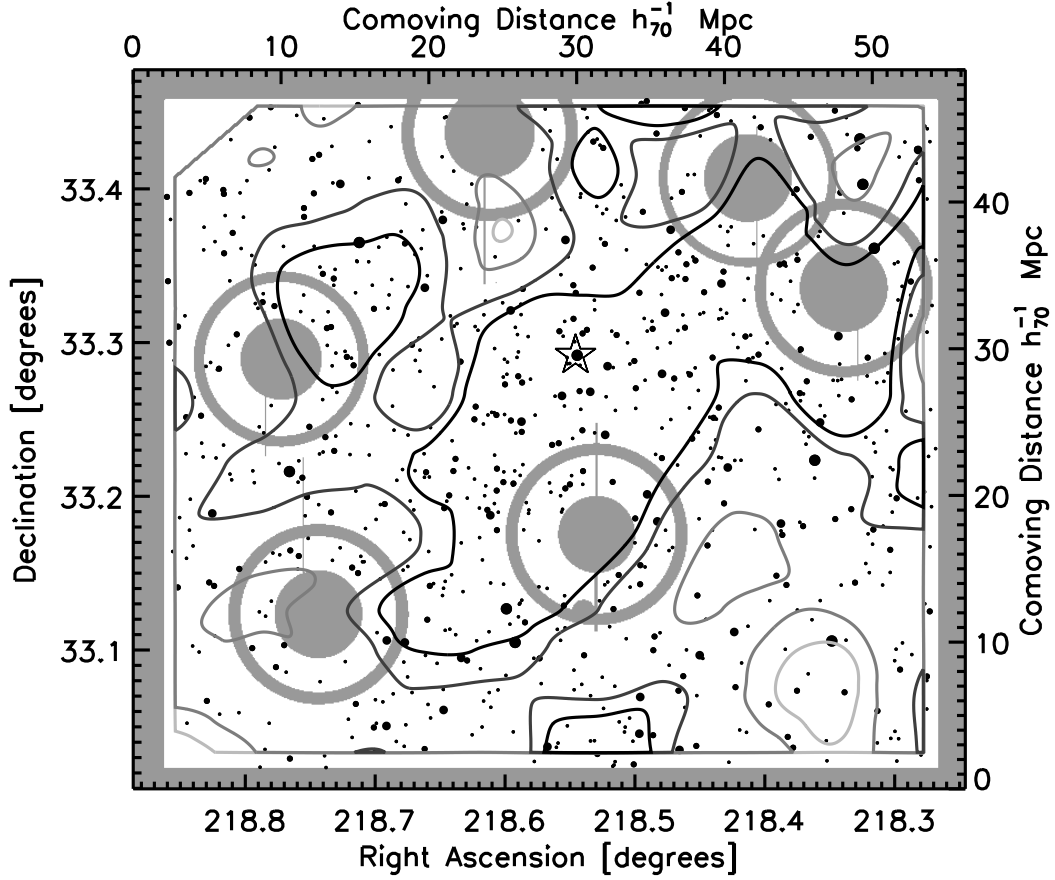


Figure 3.3 Spatial distribution of LAE candidates (filled circles). After smoothing on $3.2' \times 2.8'$ scales, isodensity contours were laid down at 0.7, 1.0, 1.8, and 2.3 times the average LAE density at the edge of the field. The four circle sizes represent four bins in IA_{445} luminosity: $L_{IA_{445}} \leq 2.5 \times 10^{42}$, $2.5 \times 10^{42} < L_{IA_{445}} \leq 5 \times 10^{42}$, $5.0 \times 10^{42} < L_{IA_{445}} \leq 1.0 \times 10^{43}$, $L_{IA_{445}} > 1.0 \times 10^{43}$. The position of LABd05 is indicated with a star. Regions masked along the edge and due to bright stars are shown in grey. There is evidence for an extended structure stretching from SE to NW and a $\sim 10 h_{70}^{-1}$ Mpc void at $[218.36, 33.07]$.

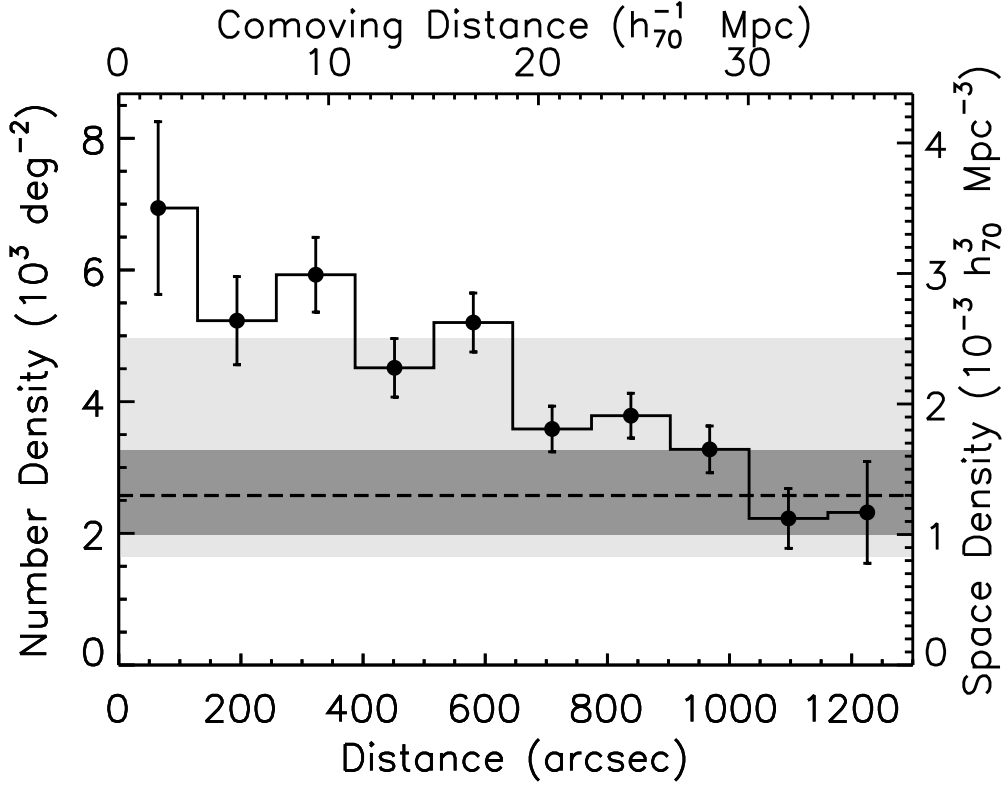


Figure 3.4 The radial density profile measured in circular annuli centered on LABd05. The LAB lies in an overdense region that is a factor of ~ 3 times the density at the edge of the field of view. The dashed line represent the predicted number density at $z \approx 3$ if we assume a uniform redshift distribution and no evolution (Gronwall et al., 2007; Ouchi et al., 2008). The shaded areas correspond to the range covered by 1σ error bars; all three parameters (α, L^*, ϕ^*) from Gronwall et al. (2007) were allowed to vary in turn (light shading), while in the comparison to Ouchi et al. (2008) the faint-end slope α is fixed at -1.5 (dark shading). The predicted LAE number density is consistent with what we measured at the edge of the field. Since the redshift distribution of our sample can only be narrower than assumed, the overdensity measured within the structure is likely a lower limit.

straddles the Lyman limit ($\lambda_{rest} \approx 970\text{-}1000\text{\AA}$ at $z \approx 2.656$). Using the 25 Myr old model above to represent the typical LAE continuum shape, the $z \approx 3$ galaxy luminosity function from Reddy et al. (2008), and standard intergalactic absorption (Madau, 1995), we predict that $\sim 1\text{-}2\%$ of the LAE sample should have U_d detected at the 5σ level ($U_d=25.3$). Only 1 LAE candidate ($<1\%$) is detected with $U_d \leq 25.3$, giving us confidence that we have selected a clean sample of LAEs. More sophisticated interloper rejection would require deeper U_d imaging over the entire field.

3.4 Results & Discussion

Figure 3.3 shows the spatial distribution of LAEs in the vicinity of LABd05. We find an overabundance of LAEs in the immediate vicinity of the LAB and clear evidence of an elongated overdense structure, with what appears to be a $\sim 10 h_{70}^{-1}$ Mpc underdensity at $[218.36, 33.07]$. In Figure 3.4, we plot the surface density of LAEs versus distance from LABd05. This shows a peak overdensity of a factor of 3.0 relative to the edge of the field, or a factor of 2.6 when averaged over the central $10 h_{70}^{-1}$ Mpc radius. For comparison, the dashed line shows the expected LAE surface density estimated from the $z \approx 3.1$ luminosity functions of Gronwall et al. (2007) and Ouchi et al. (2008) assuming a uniform redshift distribution across our bandpass and no evolution. The overdensity spans at least $\approx 17 \times 47 h_{70}^{-1}$ Mpc (comoving). A study of the LAE population around the two S00 LABs, which are of comparable size and luminosity to LABd05, also found a factor of ~ 3 overdensity relative to the field that was ~ 60 Mpc across (Hayashino et al., 2004). Thus, although it was found without any a priori knowledge of its surroundings, LABd05 appears to reside in a similarly overdense environment.

Without follow-up spectroscopy, we cannot know the true redshift distribution of the sample within the intermediate-band filter. Assuming a uniform distribution across the filter ($\Delta z \approx 0.17$, $180 \text{ h}_{70}^{-1} \text{ Mpc}$, comoving, along the line-of-sight), our survey yields a mean number density of $\rho \approx 2.1 \times 10^{-3} \text{ h}_{70}^3 \text{ Mpc}^{-3}$ for LAEs with $L_{IA445} \gtrsim 1.5 \times 10^{42} \text{ erg s}^{-1} \text{ cm}^{-2}$. The inner contour in Figure 3.3 corresponds to $\rho \approx 2.8 \times 10^{-3} \text{ h}_{70}^3 \text{ Mpc}^{-3}$ while at the edge of the field $\rho \approx 1.2 \times 10^{-3} \text{ h}_{70}^3 \text{ Mpc}^{-3}$. Given the presence of an overdensity, we expect the true redshift distribution to be significantly narrower. If we assume the overdensity resembles that hosting the S00 LABs, which extends $40 \text{ h}_{70}^{-1} \text{ Mpc}$ comoving (22% of the filter width) along the line-of-sight (Matsuda et al., 2005), and that it is centered within the $IA445$ filter, the inner contour corresponds to a number density of $\rho \approx 12 \times 10^{-3} \text{ h}_{70}^3 \text{ Mpc}^{-3}$. Alternately, if the structure is cylindrical in shape with a radius of $10 \text{ h}_{70}^{-1} \text{ Mpc}$, the corresponding number density at the inner contour is $\rho \approx 25 \times 10^{-3} \text{ h}_{70}^3 \text{ Mpc}^{-3}$.

We estimate the expected frequency of such overdense structures using the galaxy catalog of Bower et al. (2006), which is based on the Millennium Simulation (Springel et al., 2005). We approximate our observational set-up by sampling the simulation volume randomly with cylinders that are $10 \text{ h}_{70}^{-1} \text{ Mpc}$ in radius (the size of the overdensity peak) and $180 \text{ h}_{70}^{-1} \text{ Mpc}$ in depth (the full span of the filter). We assumed a $\text{Ly}\alpha/\text{H}\alpha$ ratio of 10 (Osterbrock, 1989) and scaled from the predicted $\text{H}\alpha$ luminosity to select model LAE galaxies down to the $\text{Ly}\alpha$ limit of our observations (under the assumption that $\text{Ly}\alpha$ dominates the measured $IA445$ flux) at a redshift of $z \approx 2.7$. The number density of model LAEs in this case is $10.8 \times 10^{-3} \text{ h}_{70}^3 \text{ Mpc}^{-3}$, which is a factor of ~ 5 higher than the mean density we observe. Taken at face value, this could imply that LAEs have a duty cycle of $\sim 20\%$

or that they are a younger, less massive subset of this population. If we restrict the model galaxies to be younger than the sample’s median age (≤ 172 Myr) and less massive than the median stellar mass ($\leq 9 \times 10^8 M_\odot$), the number density of model LAEs is $3.5 \times 10^{-3} h_{70}^3 \text{ Mpc}^{-3}$. In either case, we uncover overdensities of greater than a factor of 2 at a rate of $\approx 0.3\%$. Therefore, within the large span of our filter, which will tend to average out inhomogeneities and reduce the signal, our imaging survey had only a $\approx 0.3\%$ chance of randomly uncovering such an overdense region if LABs and overdensities are independent phenomena. The space density of large $\text{Ly}\alpha$ nebulae is very uncertain, but at the high end is the range quoted for the S00 $\text{Ly}\alpha$ nebulae; $\sim 3\text{--}400 \times 10^{-6} \text{ Mpc}^{-3}$ (Saito et al., 2006). Taking these values (equivalent to a $\sim 17\text{--}100\%$ chance of finding one large LAB within the peak of the overdensity), the likelihood of a chance coincidence between a factor of >2 overdensity and a large $\text{Ly}\alpha$ nebulae would be $\lesssim 0.05\text{--}0.3\%$. Preliminary results from more recent systematic $\text{Ly}\alpha$ nebulae surveys hint that their true space density may be orders of magnitude lower (e.g., Prescott et al. 2008, in preparation), making the likelihood of chance coincidence vanishingly small.

In terms of the relevant emission mechanisms the $\text{Ly}\alpha$ nebula class appears to be a highly heterogeneous mix, and this diversity could in principle derive from environmental differences. The largest $\text{Ly}\alpha$ nebulae ($\gtrsim 100$ kpc), including the case studied here, often show evidence for obscured AGN and extended star formation (e.g., Matsuda et al., 2007; Basu-Zych & Scharf, 2004, Prescott et al. 2008, in preparation) and have received the most scrutiny in terms of their properties and environments. Presumably, the somewhat smaller “cooling” LABs (e.g., Nilsson et al., 2006; Smith & Jarvis, 2007) must also reside in dense regions with

sufficient gas supply, but thorough environmental studies of these sources have, to our knowledge, not yet been completed.

3.5 Conclusions

The discovery of a large $\text{Ly}\alpha$ nebula at $z \approx 2.7$ via its strong mid-infrared emission has provided an unbiased test of the association between these rare sources and galaxy overdensities. Using deep $\text{Ly}\alpha$ imaging of the environment surrounding this LAB, we identify 785 LAE candidates and find evidence for a factor of ~ 3 LAE overdensity which spans 20×50 Mpc (comoving). This is comparable to what is found in the vicinity of the well-known S00 $\text{Ly}\alpha$ nebulae. We rule out a chance coincidence at the $\lesssim 1\%$ level. In conjunction with previous work, these results point conclusively to a strong association between the largest $\text{Ly}\alpha$ nebulae and overdense regions of the Universe.

CHAPTER 4

DISSECTING A LARGE $\text{Ly}\alpha$ NEBULA AT $z \approx 2.7$

Using high resolution imaging from HST/ACS and NICMOS, we investigate the sources of ionization within a large $\text{Ly}\alpha$ nebula at $z \approx 2.656$. The local environment is filled with numerous compact galaxies — all with disk-like morphologies. At least 8 galaxies are likely at the redshift of the system, but they are offset by tens of kiloparsecs from the peak of the $\text{Ly}\alpha$ emission. We pinpoint the location of an obscured AGN (discovered previously via mid-infrared imaging) by identifying the near-infrared counterpart in the NICMOS J_{110} and H_{160} imaging and confirm that it too is offset ≈ 20 kpc in projection from the $\text{Ly}\alpha$ cloud. The HeII-emitting source seen in a ground-based spectrum is shown to be spatially extended by $0.79\text{--}1.0''$ (6–8 kpc), and the $\text{Ly}\alpha$ nebula itself is smooth with no knots or high surface brightness clumps, suggesting it cannot be powered by compact sources within the cloud. The system shows diffuse V_{606} continuum emission that is nearly coincident with the $\text{Ly}\alpha$ and HeII emission and that may either result from scattered light or a spatially extended stellar population. Since we find that the continuum sources are a negligible contribution to the ionization of the nebula, we suspect that the ionization of the system is dominated either by an obscured AGN that is directed towards the $\text{Ly}\alpha$ cloud, or by a combination of an obscured AGN and a spatially extended stellar population.

4.1 Introduction

Giant $\text{Ly}\alpha$ nebulae (or $\text{Ly}\alpha$ ‘blobs’) are an extremely energetic and rare phenomenon. The handful of cases that have been studied in detail show complex

morphologies, high Ly α luminosities, numerous associated star-forming galaxies, and obscured AGN (e.g., Francis et al., 1996; Steidel et al., 2000; Palunas et al., 2004; Chapman et al., 2004; Geach et al., 2007; Basu-Zych & Scharf, 2004; Dey et al., 2005; Smith et al., 2008). The largest examples of the Ly α nebula class are over 100 kpc in size with Ly α line luminosities of 10^{44} erg s $^{-1}$. There is now strong evidence that Ly α nebulae are confined to the most overdense regions of the Universe (Chapter 3; e.g., Palunas et al., 2004; Matsuda et al., 2004; Saito et al., 2006; Prescott et al., 2008; Yang et al., 2009). All of these factors suggest that these sources may be sites of ongoing massive galaxy formation.

As the number of large Ly α nebulae remains small, attempts to understand their inner workings have focused on studies of individual objects. Individual cases yield valuable insights into the range of physical processes involved in powering Ly α nebulae and demonstrate the regimes in which each process dominates. For example, the two Ly α nebulae that were found in close proximity within the SSA22 field at $z \approx 3.1$ appear to be distinct in terms of their ionization mechanisms (Steidel et al., 2000). One is thought to be powered by a heavily-obscured starburst galaxy, while the other shows evidence of being ionized by an AGN (Geach et al., 2007). In contrast, a Ly α nebula found in the GOOD-S field cannot be easily explained either by AGN activity or by the starburst hypothesis, and is claimed to be a candidate for the gravitational cooling radiation model (Nilsson et al., 2006).

One particularly interesting Ly α nebula was discovered at $z \approx 2.656$ via its extreme MIPS 24 micron emission and its extended morphology in broad-band B_W imaging (Paper I; Dey et al., 2005). Roughly 20'' (~ 160 kpc) in size with a Ly α luminosity of $\approx 1.7 \times 10^{44}$ erg s $^{-1}$, it rivals other known Ly α nebulae both

in terms of energetics and complexity. The ground-based spectrum revealed at least three potential sources of ionization in the system. First, there is the strong $24\mu\text{m}$ source, which is likely dominated by an obscured AGN. Second, there is a Lyman break galaxy to the Northeast of the nebula, and third, there is an unidentified source near the center of the $\text{Ly}\alpha$ emission that has narrow He II and C IV emission lines, suggesting a hard ionizing source.

From the ground-based study it was unclear whether the $24\mu\text{m}$ sources and the Lyman break galaxy can provide the necessary ionization to power the $\text{Ly}\alpha$ nebula. The geometry of the system, with both the $24\mu\text{m}$ source and the Lyman break galaxy offset from the centroid of the $\text{Ly}\alpha$ by $2''.5$ (~ 20 kpc in projection), argues against this possibility. In addition, the observed SED of both sources suggests that they are unlikely to power more than $\sim 20\%$ of the $\text{Ly}\alpha$ emission. On the other hand, the source of He II and C IV emission appears to be centered on the nebula but the line ratios are inconsistent with shocks and no obvious continuum source could be identified in the ground-based data. At the conclusion of this initial study, it appeared likely that the $\text{Ly}\alpha$ nebula is powered by multiple sources.

The high resolution HST imaging presented here allowed us to take a census of all the compact ionization sources in the system. We use HST/ACS V_{606} and NICMOS J_{110} and H_{160} imaging to determine the locations of continuum sources relative to the line-emitting gas, and measure their luminosities and morphologies. We address the question of the location and morphology of the He II-emitting region and investigate the clumpiness of the $\text{Ly}\alpha$ nebula itself. In Section 4.2 we describe our observations and reductions and in Section 4.3 we present our results on the different components of the $\text{Ly}\alpha$ nebula system. Section 4.4 dis-

Table 4.1. Multiwavelength Observations of a Large Ly α Nebula at $z \approx 2.656$

Instrument	Filter/Grating/Configuration Description	Exposure Time (min)	λ_C	Bandpass Width	Restframe λ at $z \approx 2.656$
HST/ACS	FR462N ([O II] outer ramp)	216	4448.9 Å	89 Å	Ly α 1216
HST/ACS	F606W (Broad-band V)	129	5917.7 Å	2342 Å	1298-1939 Å
HST/ACS	FR601N ([O III] outer ramp)	129	5998.1 Å	120 Å	He II λ 1640
HST/NICMOS NIC2	F110W (Broad-band J)	141	1.1 μ m	0.52 μ m	2298-3720 Å
HST/NICMOS NIC2	F160W (Broad-band H)	141	1.6 μ m	0.40 μ m	3829-4923 Å

cusses the sources of ionization and the total energy budget of the system, and we conclude in Section 4.5. In this paper, we assume the standard Λ CDM cosmology ($\Omega_M=0.3$, $\Omega_\Lambda=0.7$, $h=0.7$); the angular scale at $z = 2.656$ is 7.96 kpc/'. All magnitudes are in the AB system (Oke, 1974).

4.2 Observations & Reductions

Previous work looked at the properties and large scale environment of LABd05 using Keck/LRIS spectroscopy, NDWFS optical imaging, Spitzer/IRAC and MIPS imaging (Paper I, Jannuzi & Dey, 1999; Eisenhardt et al., 2004, , E. Le Floch, private communication), and Subaru/SuprimeCam intermediate-band Ly α imaging (Prescott et al., 2008). In this paper we use high resolution HST/ACS and NICMOS imaging to study the local environment of this large Ly α nebulae and locate the potential sources of ionization in the system. Table 4.1 lists the instruments, filters, and total exposure times for the dataset used in this work; Figure 4.1 shows postage stamps of the entire multiwavelength dataset.

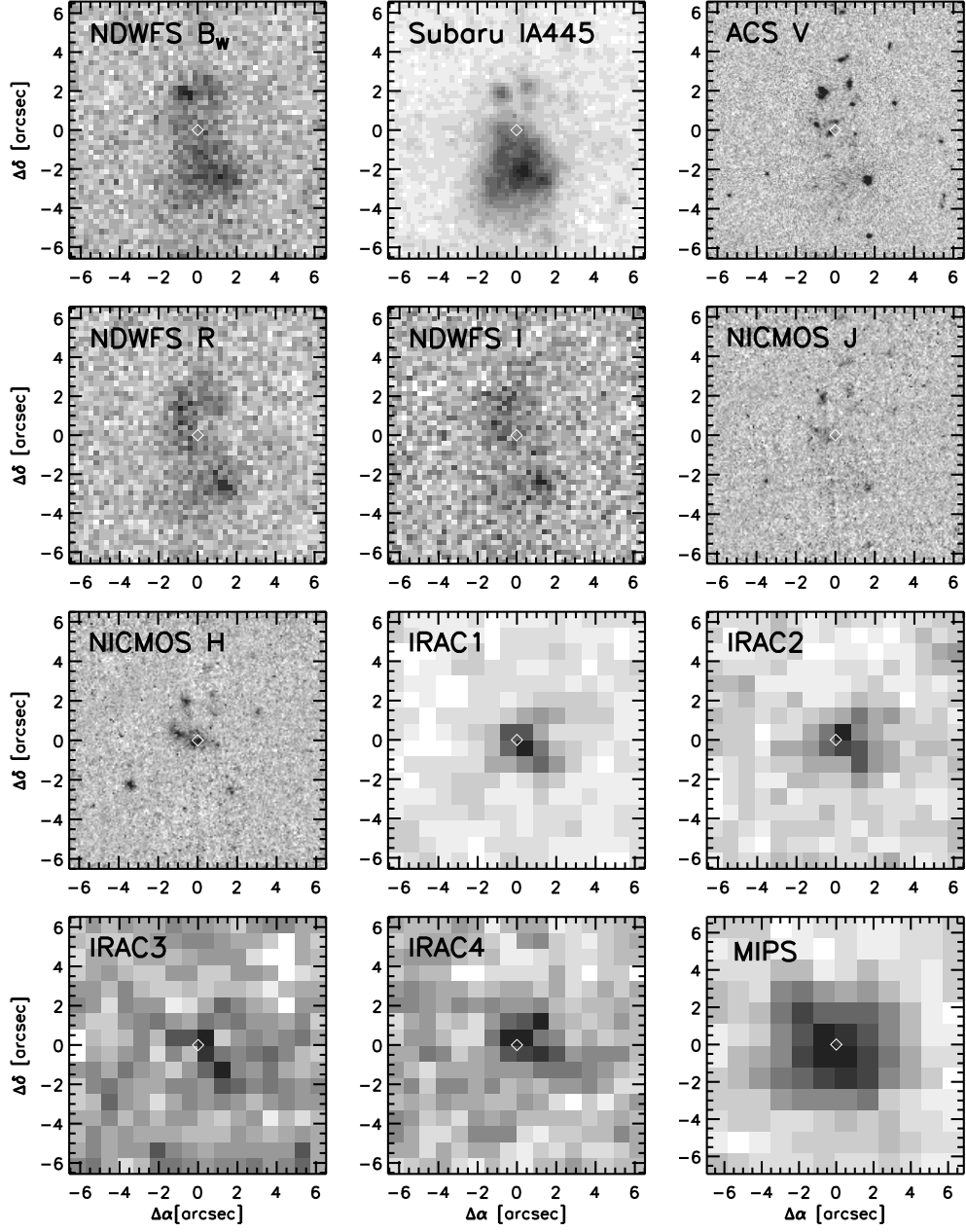


Figure 4.1 Multiwavelength imaging of LABd05. In each panel, the white diamond denotes the location of the obscured AGN (Section 4.4.1).

4.2.1 HST ACS Data

We obtained HST Advanced Camera for Surveys (ACS) imaging of LABd05 on UT 2006 January 13, 14, and 24 using the *F606W* (V_{606}) and two ramp filters, *FR462N* (centered on $\text{Ly}\alpha$ at $z\approx 2.7$) and *FR601N* (centered on HeII at $z\approx 2.7$) filters, respectively. Basic image calibrations (overscan, bias, and dark subtraction, flat-fielding) were provided by the standard HST ACS pipeline with On-The-Fly-Reprocessing (OTFR) and the task *calacs*. We removed a residual offset in the bias level of the individual amplifiers on each of the ACS detectors (roughly a 2% effect relative to the background) by estimating the sky background in each amplifier separately using a sigma-clipped mean and subtracting it from the calibrated, flat-fielded individual exposures (file suffix *_FLT*). Using MultiDrizzle’s default settings and no sky subtraction, we performed the distortion correction, cosmic-ray rejection, and image combination. The point-spread-function (PSF) size measured from the *F606W* imaging is $0.11''$. The 5σ point source limiting magnitudes for the ACS imaging are 28.33, 25.67, and 25.70 mag ($0.4''$ diameter aperture) for the *F606W*, *FR462N*, and *F601N* filters, respectively.

As the narrow-band $\text{Ly}\alpha$ and HeII imaging contains both line and continuum emission, we had to subtract off the continuum in order to generate a line-only image. We scaled the V_{606} image by a factor of 51.52 and 23.95, respectively (estimated empirically based on sources common to both images) and subtracted it from the original narrow-band image. The HeII and CIV lines are contained within the V_{606} bandpass but contribute only 6% of the flux, so we do not apply a correction for the lines. The continuum-subtracted $\text{Ly}\alpha$ and HeII images are shown in Figure 4.7.

4.2.2 HST NICMOS Data

Using the HST NICMOS NIC2 camera, we obtained high-resolution imaging of the source in the $F110W$ (J_{110}) and $F160W$ (H_{160}) filters, which at $z \approx 2.7$ bracket the Balmer/4000Å break. The observations were taken during UT 2006 March 25 and 31. The raw data (file suffix *_RAW*) were processed using *nicpipe*, which controls the operation of the main calibration task, *calnica*, the tasks *biaseq* and *pedsky*, which attempt to remove the pedestal, and the task *calnicb*, which combines the images. The *pedsky* task was used, following the procedure outlined in the NICMOS Data Handbook¹, to mitigate the problem of variable quadrant bias or “pedestal” - a well-known issue with NICMOS data. To remove residual pedestal structure, we then created a background map by masking all the objects and boxcar smoothing the image using a 20×20 pixel ($1.5 \times 1.5''$) kernel; this background map was subtracted off to create the final image. The measured PSF sizes are 0.11 and 0.16'', and the 5σ point source limiting magnitudes are 26.83 and 26.60 mag (0.4'' diameter aperture) for the J_{110} and H_{160} imaging, respectively. There is a $\sim 1\%$ uncertainty in the magnitude zeropoint². After the data reduction was completed, the NICMOS team discovered that NICMOS has a substantial count rate non-linearity that depends on wavelength. The magnitude of the offset for faint sources is at most ~ -0.2 mag in J_{110} ; the effect in H_{160} is smaller ~ -0.03 mag³. A complete correction to the problem involves redoing some of the data reduction using the task *rnlincon*. As of this writing we have applied a generic correction of -0.2 mag to our J_{110} photometry, but we will complete the full correction prior to publication. All conclusions regarding the energy budget

¹<http://www.stsci.edu/hst/nicmos/documents/handbooks/DataHandbookv6/>

²NICMOS Data Handbook — <http://www.stsci.edu/hst/nicmos/>

³NICMOS ISR 2006-001 — http://www.stsci.edu/hst/nicmos/documents/isrs/isr_2006_001.pdf

and membership in the system will be unaffected.

4.2.3 Image Registration

Much of our analysis relies on understanding the relative positions of a sources within this complex object, making correct image registration essential. To ensure accurate registration, we generated catalogs of source positions in each image using SExtractor and registered all images to the NDWFS frame using the IRAF tasks *ccmap* and *ccsetwcs*. We carried out the registration in three steps. First, the ACS V_{606} was convolved with a Gaussian kernel of FWHM=20 pixels in order to match the PSF of the B_W image. We matched the smoothed ACS V_{606} images to the NDWFS B_W image and then registered the HST ACS HeII and NICMOS (J_{110} and H_{160}) images to the unsmoothed HST V_{606} . Finally, we registered the HST ACS Ly α image to the HST ACS HeII image. This sequential procedure was used to maximize the number of common sources available to compute the astrometric solution for each image pair and to avoid compounding registration errors. Table 4.2 details the number of sources used in the registration and the estimated astrometric errors.

4.3 The Components of the Nebula

Using these HST observations we find that LABd05 contains a number of compact galaxies, smooth Ly α emission, spatially-extended HeII emission, diffuse continuum emission, and an obscured AGN, all within a $\sim 10''$ region. Here we discuss each of these components of the Ly α nebula system in detail.

Table 4.2. Astrometric Uncertainty

Band	N_{obj}^a	σ_α	σ_δ
		(arcsec)	(arcsec)
NDWFS B_W	-	-	-
ACS Ly α	17	0.19	0.17
ACS HeII	37	0.13	0.12
ACS V	402	0.13	0.11
NICMOS J	5	0.13	0.12
NICMOS H	6	0.13	0.11

Note. — Astrometric uncertainty relative to the NDWFS B_W image.

^aNumber of common sources used to compute astrometric correction.

4.3.1 Compact Sources

The high resolution ACS and NICMOS images reveal a large number of compact sources in the vicinity of LABd05. Only two of these neighboring sources were previously identified from ground-based data: a Lyman Break Galaxy to the Northeast and at the redshift of the system, and an interloper galaxy to the Southwest at $z \approx 3.2$ (Paper I). In the ACS imaging, we find that both of these sources are resolved into two components and are possibly interacting systems. We determined the relative positions of all the sources in the vicinity of the Ly α nebula by generating an initial list of source positions using SExtractor to the V_{606} image (3σ threshold, 4 pixel minimum contiguous area) (Bertin & Arnouts, 1996). For the 27 compact sources within $7''$ of the Ly α nebula, we then used GALFIT (Peng et al., 2002) to fit Sérsic profiles in order to derive precise cen-

troids, radii, and morphologies (Figure 4.2). The morphology results are given in Table 4.3. Aside from a large, diffuse V_{606} continuum component (Section 4.3.4), all the galaxies in the vicinity of LABd05 are all small ($R_e = 1 - 3$ kpc) with Sérsic $n \approx 1$, indicative of exponential disk morphologies (Figure 4.3).

Since the NICMOS bands straddle the Balmer/4000Å break at the redshift of the nebula, sources at the redshift of the nebula should show a break in the SED and red $J_{110} - H_{160}$ colors; we attempt to use this fact to identify sources that are likely associated with the system. To derive colors for the compact sources in the vicinity of the Ly α nebula we smoothed the ACS V_{606} and NICMOS J_{110} band images to match the PSF of the NICMOS H_{160} band and then measured aperture photometry (0.4'' diameter apertures) using the positions derived from the V_{606} imaging. Since the images were PSF-matched, no aperture correction was applied. Figure 4.4 shows the V_{606} , J_{110} , and H_{160} images with the positions of the sources indicated. In Figure 4.5 we plot the $J_{110} - H_{160}$ versus $V_{606} - J_{110}$ colors of the compact sources in the vicinity of the Ly α nebula; the V_{606} , J_{110} , and H_{160} aperture photometry of the compact sources are included in Table 4.3. We discuss using the ACS and NICMOS photometry to determine system membership in Section 4.4.2.

4.3.2 Diffuse Ly α Emission

We used the high resolution ACS Ly α imaging to determine whether the Ly α nebula is spatially resolved into discrete knots or clumps that could signal the locations of the ionizing sources for the nebula. We find that the morphology of the Ly α nebula is smooth, with no significant substructure (Figure 4.6). At the depth of these observations we would have detected point-source regions to Ly α line fluxes of 3.0×10^{-17} erg s $^{-1}$ cm $^{-2}$ (5σ). This corresponds to a mass limit of

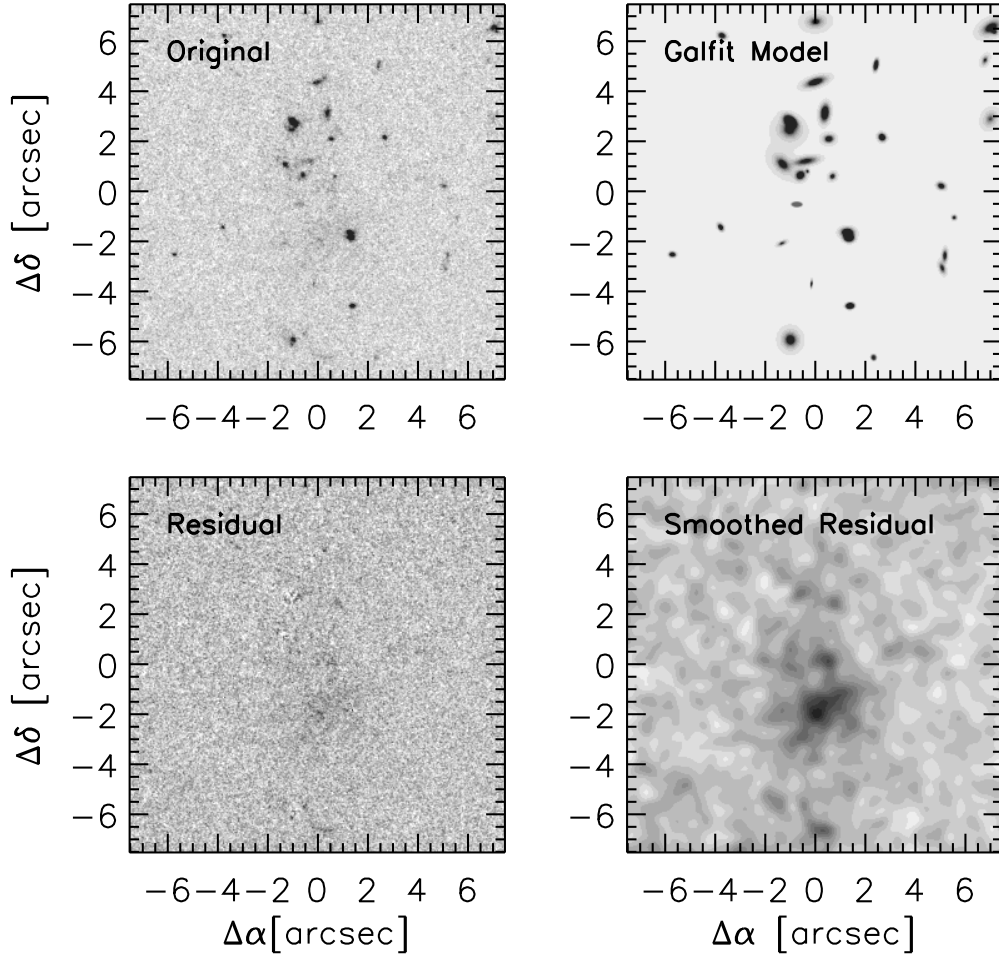


Figure 4.2 GALFIT parametric fit to the V_{606} imaging of LABd05. The top two panels show the original V_{606} image and GALFIT model. The residual image and smoothed residual image ($FWHM = 10 \text{ pix} = 0.5''$ Gaussian kernel) in the bottom two panels reveal a diffuse continuum component that is nearly coincident with the $\text{Ly}\alpha$ emission.

Table 4.3. Compact Sources within a Large Ly α Nebula at $z \approx 2.656$

ID	Right Ascension (hours)	Declination (degrees)	R_e (arcsec)	n	m_V^a (AB)	m_J^a (AB)	m_H^a (AB)
3	14:34:10.945	33:17:29.93	0.36	2.04	27.42 ± 0.05	26.71 ± 0.11	26.97 ± 0.23
6	14:34:10.854	33:17:30.05	0.10	0.96	27.46 ± 0.05	< 27.39	< 27.15
8	14:34:10.849	33:17:29.85	0.16	0.44	27.53 ± 0.06	26.77 ± 0.11	< 27.15
10	14:34:11.063	33:17:29.61	0.29	0.97	26.96 ± 0.04	26.61 ± 0.10	26.45 ± 0.15
11	14:34:10.902	33:17:32.28	0.22	0.74	26.75 ± 0.04	26.53 ± 0.09	26.49 ± 0.15
12	14:34:11.015	33:17:31.16	0.15	0.86	25.61 ± 0.02	25.80 ± 0.05	25.63 ± 0.07
13	14:34:10.987	33:17:32.89	0.34	1.64	26.32 ± 0.03	26.13 ± 0.07	25.99 ± 0.10
15	14:34:11.061	33:17:32.78	0.09	1.00	27.06 ± 0.05	26.89 ± 0.12	26.19 ± 0.12
16	14:34:11.004	33:17:32.33	0.12	1.48	27.16 ± 0.05	27.15 ± 0.16	26.69 ± 0.18
17	14:34:10.981	33:17:32.49	0.34	0.65	27.48 ± 0.06	27.20 ± 0.16	26.17 ± 0.12
18	14:34:11.036	33:17:34.48	0.32	2.87	26.73 ± 0.04	26.22 ± 0.07	25.27 ± 0.05
19	14:34:11.040	33:17:34.14	0.12	0.80	26.99 ± 0.04	26.28 ± 0.07	25.09 ± 0.05
20	14:34:10.926	33:17:34.82	0.10	1.39	27.94 ± 0.08	< 27.39	26.63 ± 0.18
21	14:34:10.913	33:17:33.79	0.11	0.72	27.68 ± 0.06	< 27.39	< 27.15
22	14:34:10.956	33:17:36.06	0.16	0.11	27.85 ± 0.07	< 27.39	< 27.15
23	14:34:10.956	33:17:38.48	0.07	0.54	< 28.88	< 27.39	< 27.15
24	14:34:11.255	33:17:37.92	0.09	0.88	27.83 ± 0.07	26.41 ± 0.08	24.83 ± 0.04
25	14:34:10.763	33:17:36.74	0.14	1.00	26.14 ± 0.03	26.36 ± 0.08	26.26 ± 0.12
26	14:34:10.743	33:17:33.85	0.10	0.85	25.72 ± 0.02	25.92 ± 0.05	26.05 ± 0.10
27	14:34:10.554	33:17:31.90	3.11	1.10	28.41 ± 0.10^b	< 27.39	< 27.15
28	14:34:10.512	33:17:30.64	0.17	0.73	28.00 ± 0.07	< 27.39	< 27.15
29	14:34:10.542	33:17:29.11	0.08	0.74	27.73 ± 0.06	< 27.39	26.99 ± 0.24
30	14:34:10.551	33:17:28.62	0.17	0.84	27.97 ± 0.07	< 27.39	< 27.15
31	14:34:11.259	33:17:30.25	0.10	0.91	28.33 ± 0.09	< 27.39	< 27.15
33	14:34:11.413	33:17:29.16	0.10	0.53	26.95 ± 0.04	26.76 ± 0.12	26.77 ± 0.22
34	14:34:10.968	33:17:27.99	0.23	1.51	26.83 ± 0.04	26.13 ± 0.08	25.53 ± 0.08
39	14:34:10.845	33:17:27.10	0.06	0.71	28.55 ± 0.12	26.78 ± 0.11	25.29 ± 0.05
40	14:34:11.036	33:17:25.74	0.14	0.88	28.16 ± 0.08	< 27.39	< 27.15

^aAperture magnitudes (0.4'' diameter apertures). The V_{606} and J_{110} images were smoothed to match the H_{160} PSF; no aperture corrections were applied. Magnitude upper limits are 3σ values.

^bDue to the large size of this source — the diffuse continuum component — the aperture magnitude listed here underestimates the total flux, $m_{V,total}=23.20 \pm 0.07$ (AB), as discussed in Section 4.3.4.

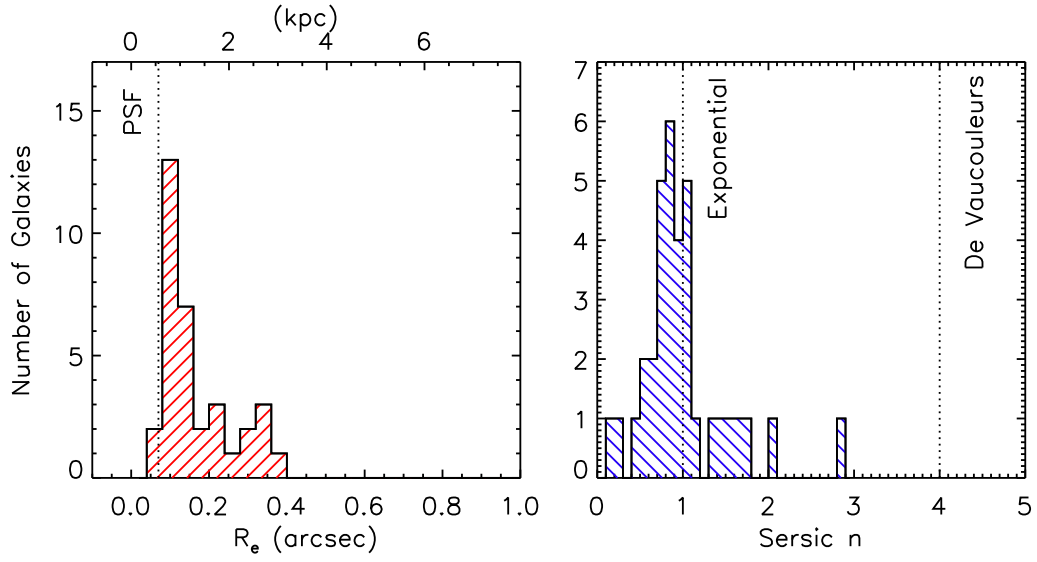


Figure 4.3 Half-light radii and morphologies derived by GALFIT for galaxies near a $\text{Ly}\alpha$ nebula. The left panel shows a histogram of galaxy half-light radii; the size of the ACS PSF is shown (dotted line). The right panel shows a histogram of Sérsic n values for all galaxies in the vicinity of LABd05, with the exception of the diffuse V_{606} continuum component (Section 4.3.4). For reference, the values for exponential ($n = 1$) and De Vaucouleurs ($n = 4$) profiles are shown (dotted lines).

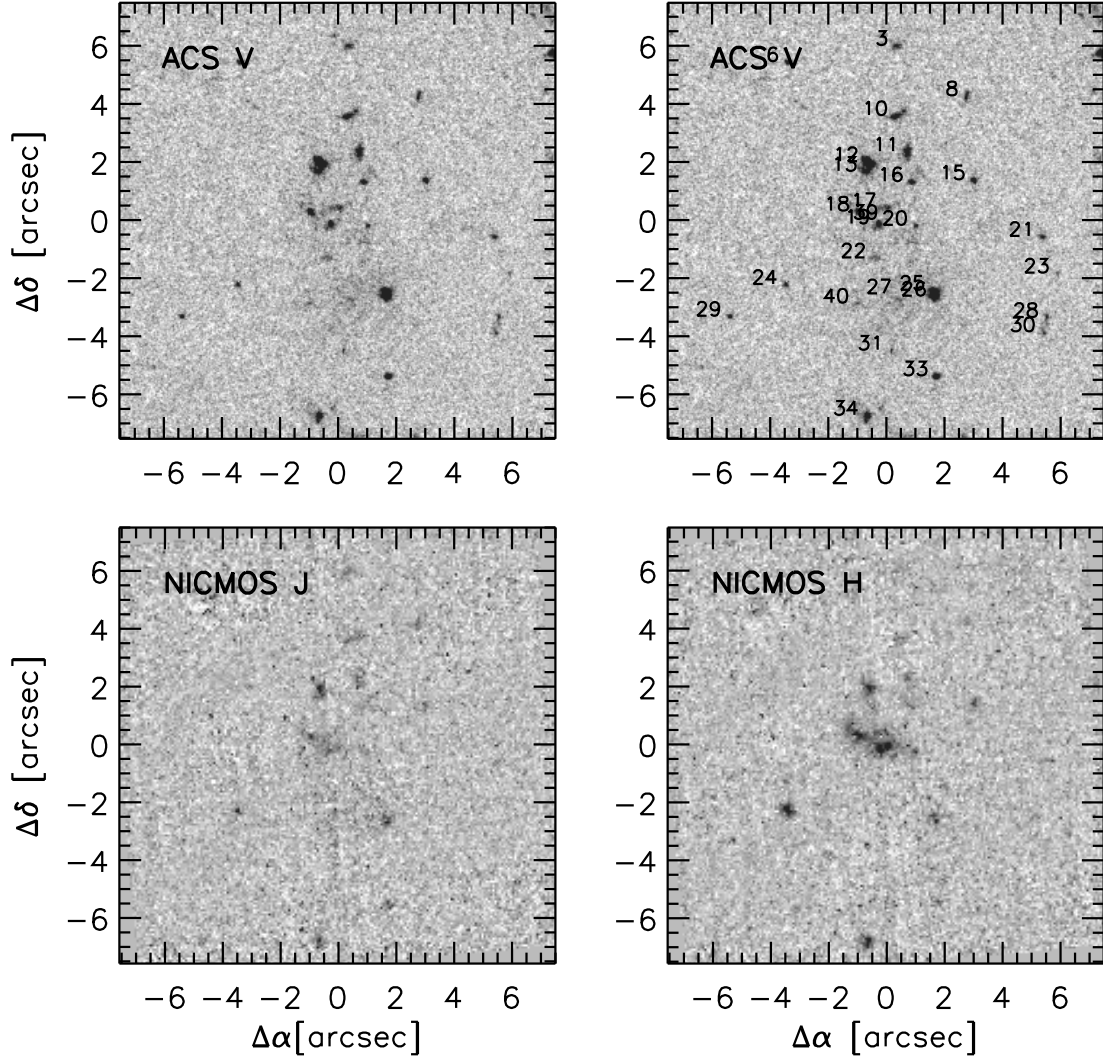


Figure 4.4 Compact sources within LABd05. (Upper panels) ACS V_{606} imaging is shown with and without source labels. All compact sources located within $7''$ of the obscured AGN at $[0'', 0'']$ are labeled with the ID number used in Table 4.3. (Lower panels) NICMOS J_{110} and H_{160} imaging.

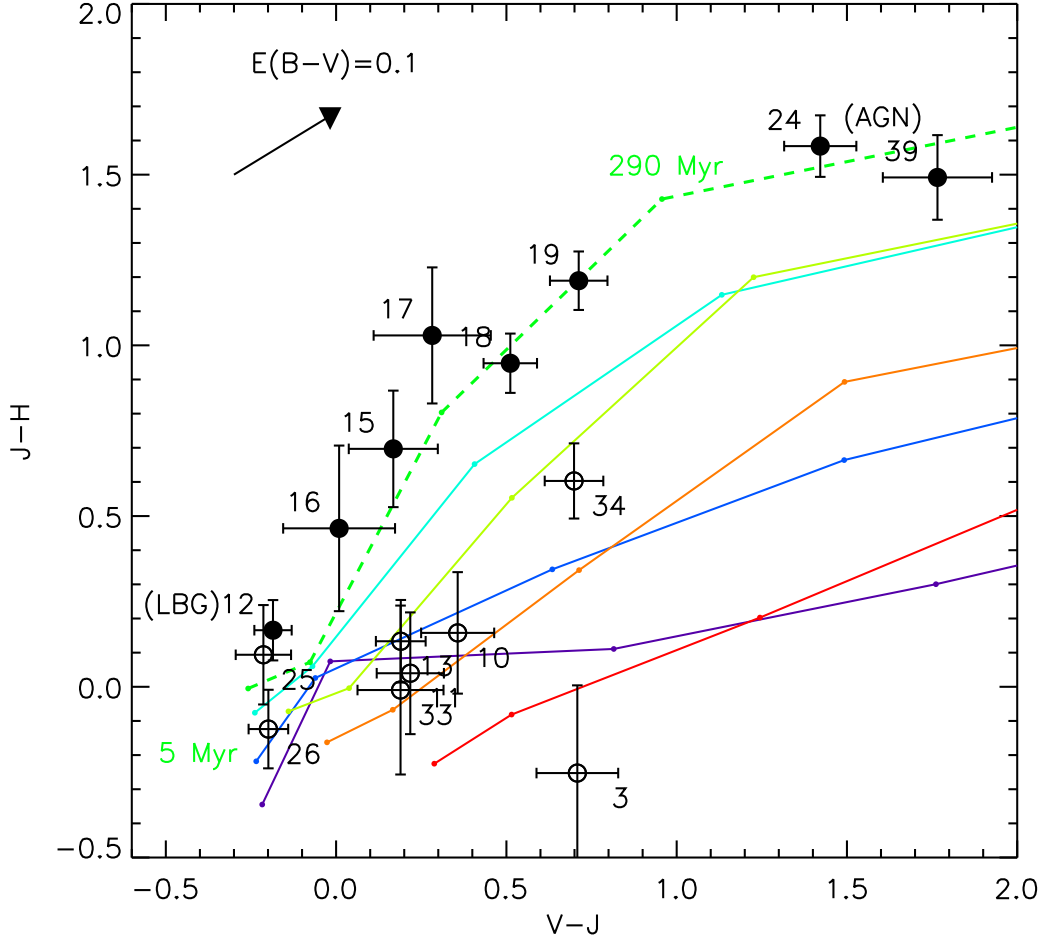


Figure 4.5 $J_{110} - H_{160}$ vs. $V_{606} - J_{110}$ color of compact sources in the vicinity of LABd05 (filled circles), with likely interlopers indicated (open circles). Upper and lower limits are 3σ values. A series of single stellar population model age tracks (unreddened burst, solar metallicity, spanning burst ages of 5, 25, 100, 290, and 640 Myr; Bruzual & Charlot, 2003) are overplotted for different redshifts (colors signify $z = [1.5, 2.0, 2.4, 2.656, 3.2, 3.5, 4.0]$ with red indicating high redshift). The dashed line corresponds to $z \approx 2.656$, the redshift of LABd05. The appropriate reddening vector is shown for $E(B - V) = 0.1$ computed at $z \approx 2.656$.

$1.7 \times 10^8 M_{\odot}$, assuming a 25 Myr single stellar population and a rest-frame $\text{Ly}\alpha$ equivalent width of 100\AA (Bruzual & Charlot, 2003). We can also rule out high surface brightness clumps within the cloud down to a peak surface brightness limit of $\approx 4.0 \times 10^{-16} \text{ erg s}^{-1} \text{ cm}^{-2} \text{ arcsec}^{-2} (3\sigma)$.

4.3.3 Diffuse He II Emission

LABd05 is known to have strong HeII and CIV emission ($F_{\text{HeII}} = 4.07 \pm 0.04 \times 10^{-17} \text{ erg s}^{-1}$, $F_{\text{CIV}} = 4.17 \pm 0.04 \times 10^{-17} \text{ erg s}^{-1}$; Keck/LRIS spectrum) near the center of the $\text{Ly}\alpha$ nebula $[0.08'', -2.5'']$. We obtained HeII imaging in order to localize the HeII-emitting region within the system; the depth of the imaging should have revealed a point source detection at $SNR \approx 10$. However, we find that the ACS HeII imaging showed no detection down to a 5σ point source limiting magnitude of $2.1 \times 10^{-17} \text{ erg s}^{-1} \text{ cm}^{-2}$ and a 3σ surface brightness limit of $3.27 \times 10^{-16} \text{ erg s}^{-1} \text{ cm}^{-2} \text{ arcsec}^{-2}$ ($0.4''$ diameter aperture). This non-detection puts a constraint on the size of the HeII-emitting region. We used a series of simulated HeII sources, modeled as Gaussian profiles with the measured HeII flux and a range of FWHM sizes of $0.1 - 1.5''$ and inserted them into the HeII image (Figure 4.7). For each of 100 Monte Carlo trials, we measured the SNR as a function of $FWHM$ and determined the $FWHM$ for which the model is detected at $SNR = 3$. We conclude that the source of HeII must be extended by at least $FWHM > 0.79''$ in order to be undetected in our HeII imaging. At the same time, the fact that the previous long-slit spectroscopy did not resolve the HeII line puts an upper limit of $1''$ on the size of the HeII-emitting region. This size range corresponds to $\sim 6.3 - 8.0 \text{ kpc}$ at the redshift of the nebula.

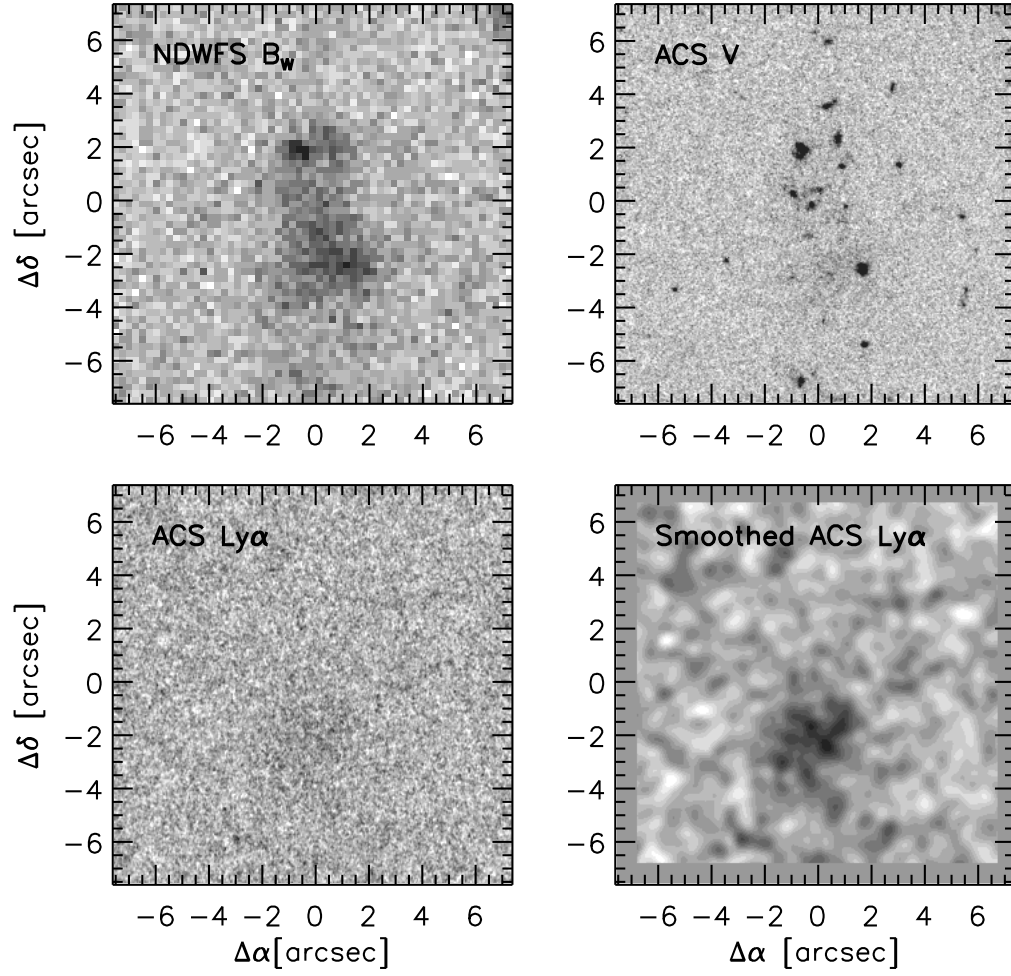


Figure 4.6 Ly α imaging of LABd05. The NDWFS B_W , the ACS V_{606} , and the ACS continuum-subtracted Ly α imaging along with a smoothed version (Gaussian FWHM=10 pix=0.5").

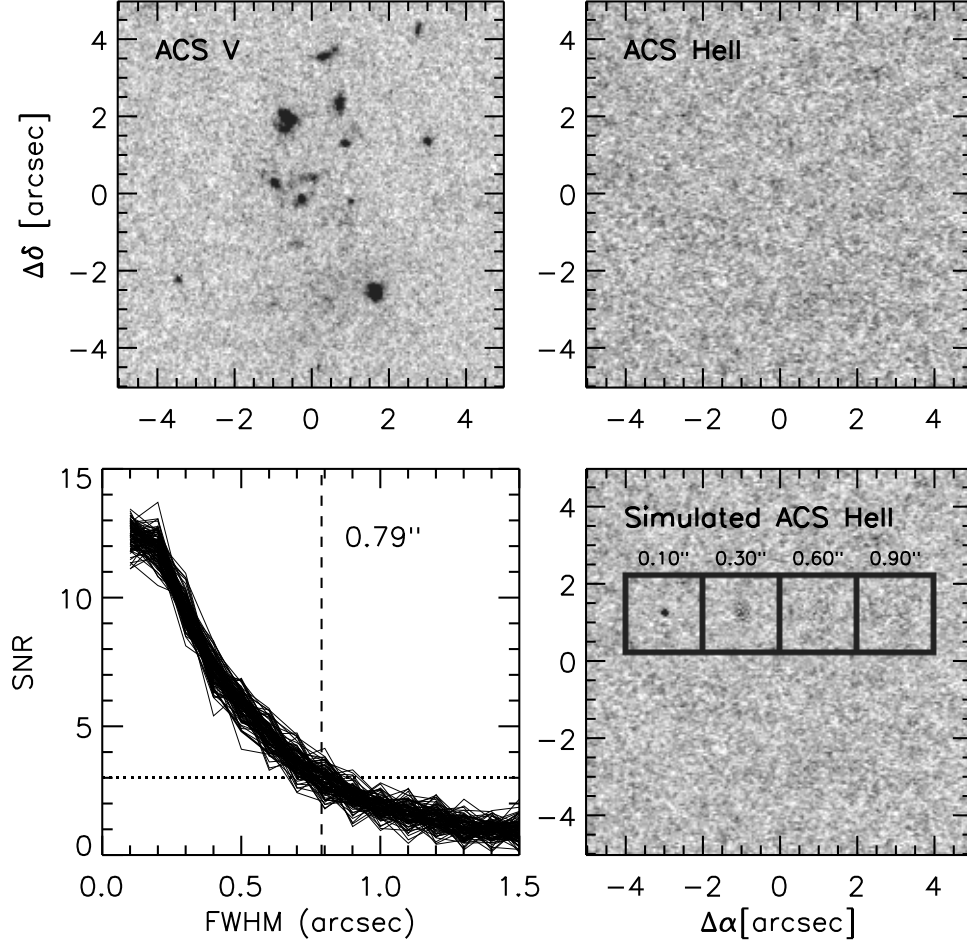


Figure 4.7 Limits on the size of the HeII-emitting region derived from the continuum-subtracted ACS HeII imaging. (Upper panels) ACS V_{606} and continuum-subtracted HeII imaging. (Lower left) The measured signal-to-noise ratio (SNR ; $0.4''$ diameter aperture) for a Gaussian model source with the known HeII flux as a function of FWHM; a $SNR = 3$ is shown (dotted line) as well as the derived lower limit on the size of the HeII-emitting region ($FWHM > 0.79''$; dashed line). (Lower right) A simulated HeII image containing a representative set of model sources ($FWHM = [0.1'', 0.3'', 0.6'', 0.9'']$).

4.3.4 Diffuse Continuum Emission

In addition to the population of compact sources, the broad-band ACS V_{606} data also revealed diffuse continuum emission located near the center of the Ly α nebula (Figure 4.2). To measure the size and luminosity of this component, we again used GALFIT (Peng et al., 2002). We took care to avoid contamination from nearby compact sources by fitting the diffuse component while constraining all compact sources to the previously-derived parametric fits. Table 4.3 gives the position, size, and Sérsic index of the diffuse component. As with the compact sources in the system, the diffuse continuum component is well-fit by an exponential disk profile. We find that the centroid is nearly coincident with the Ly α emission and derived a total flux using the GALFIT model fit of $m_{V,total}=23.20\pm0.07$ mag. (The aperture photometry listed in the table was measured using small $0.4''$ diameter aperture, and therefore substantially underestimates the flux in this extended component.) While there is no spatial coincidence between the continuum component and the compact sources, the diffuse continuum is nearly coincident with the Ly α emission.

4.4 Discussion

4.4.1 The Location of the Obscured AGN

Paper I postulated the existence of an embedded AGN at the position of the MIPS source due to strong $24\mu\text{m}$ emission and the fact that the source shows a power-law SED in the mid-infrared IRAC bands. The location of the AGN was more uncertain due to the low resolution of the IRAC and MIPS imaging (PSF $FWHM = 2.0 - 6.6''$). The addition of the HST/NICMOS imaging shows that there is a very red source (#39; Figure 4.4) at the centroid of the MIPS 24 micron

emission. The source shows a strong Balmer/4000Å break; it is barely detected in V_{606} and J_{110} but very bright in H_{160} . From the morphology estimate, the source appears unresolved ($< 0.07''$) in the V_{606} imaging with a Sérsic index of $n \approx 0.7$ (approaching the value for a Gaussian, $n = 0.5$). All of these pieces of evidence are consistent with this source being the rest-frame optical counterpart of an obscured AGN. Assuming that this is correct, the measured projected offset between the AGN and the centroid of the $\text{Ly}\alpha$ emission and diffuse continuum emission is $\approx 2.6''$ (≈ 21 kpc).

4.4.2 Sources of Ionization

The high resolution HST imaging provides a census of all of the compact sources of emission in the region. In addition to the obscured AGN, there are a large number of galaxies in the vicinity, more than expected for a region of this size in the field. The observed number counts in the Hubble Deep Field for sources with $F606W = 27 \pm 0.5$ translate into a number density of $\sim 4 \times 10^5 \text{ AB mag}^{-1} \text{ deg}^{-2}$ (Metcalf et al., 2001; Marín-Franch & Aparicio, 2003). Within a $7''$ radius of the AGN, we would expect $3.98 \times 10^5 \text{ AB mag}^{-1} \text{ deg}^{-2} \times \pi(7/3600)^2 = 4.7$ galaxies with $F606W = 27 \pm 0.5$. By contrast, in the vicinity of this $\text{Ly}\alpha$ nebula, we find 10 galaxies in this magnitude range, an overdensity of at least a factor of 2.

The ACS and NICMOS photometry allow us to determine which sources are likely to be associated with the $\text{Ly}\alpha$ nebula system. We do not attempt to do sophisticated SED-fitting using the limited data presented here, but instead compare to simple stellar population model tracks spanning a range of ages and redshifts (Figure 4.5; 5-640 Myr single unreddened bursts, solar metallicity; Bruzual & Charlot, 2003). Of the sources that are detected in all three bands, we find 8 that hug the color locus for single burst models at the redshift of LABd05 (#12,

15, 16, 17, 18, 19, 24, 39) and are easily understood as being associated with the $\text{Ly}\alpha$ nebula system. One of these sources is the spectroscopically-confirmed LBG (#12) and another is the rest-frame optical counterpart of the AGN (#39). These 8 well-detected compact sources that we believe to be associated with the system are located 2.4-5.0'' (19-39 kpc) away from the peak of the $\text{Ly}\alpha$ emission. The rest of the continuum sources, i.e. those with colors to the lower right in $J_{110} - H_{160}$ vs. $V_{606} - J_{110}$ color space, are consistent with galaxies at significantly lower or higher redshift, so we flag these cases as interlopers (#3, 10, 11, 13, 33, 34) along with those previously identified as a $\text{Ly}\alpha$ -emitting system at $z \approx 3.2$ (#25 and 26).

Under the naive assumption that dust properties do not vary strongly across the system, it is tempting to interpret the distribution of the 8 continuum sources in color-color space as an age gradient across the system. In this simplified picture, the LBG and nearby systems are consistent with young 25-100 Myr models (#12, 15, 16), sources in the center of the system surrounding the AGN have intermediate ages of 100-290 Myr ages (#17, 18, 19), and a source to the East of the system (#24) and the rest-frame optical counterpart to the AGN (#39) appear to be older than 290 Myr. In reality, these estimates should be treated with caution as we know that the system contains both strong $\text{Ly}\alpha$ and strong dust emission and that the AGN is highly obscured, although we note that the fact that these galaxies do seem to closely follow the unreddened track may be indicative that the dust properties of the compact galaxies are relatively uniform.

The fact that the ACS $\text{Ly}\alpha$ imaging shows that the $\text{Ly}\alpha$ emission is smooth and diffuse, with no significant knots of high surface brightness clumps, and that the $\text{Ly}\alpha$ emission is nearly coincident with both diffuse continuum emission ($R_e \approx 3.0''$) and spatially extended HeII emission ($0.76 < FWHM < 1.0''$) suggests that

there may be an additional spatially extended source of ionization within the nebula. We discuss this possibility in Section 4.4.3.

4.4.3 The Energy Budget of LABd05

A detailed energetic model is beyond the scope of this work, but it is already clear from the high resolution imaging that compact continuum sources are a minor contribution to the ionization of the Ly α nebula. The total ionizing photon flux needed to power the Ly α is 1.7×10^{55} photons s $^{-1}$. Even if we assume that all 8 well-detected nearby galaxies at the system redshift have escape fraction of 100% and ignore the effects of distance, the total ionizing luminosity ($L_{200-912\text{\AA}}$) of the entire system (excluding the AGN) is $3.4 \times 10^{53} - 4.4 \times 10^{51}$ photons s $^{-1}$ (unreddened, 5-25 Myr single bursts Bruzual & Charlot, 2003). Furthermore, since all the compact continuum sources lie tens of kiloparsecs away from the Ly α nebula and there are no compact sources seen within the core of the Ly α nebula itself, the system is inconsistent with a scenario in which the Ly α emission is powered via outflows from a central starburst. By contrast, Dey et al. (2005) found that the total ionizing luminosity of the AGN was $> 1.8 \times 10^{54}$ photons s $^{-1}$, estimated from an extrapolation of the mid-infrared SED, at least an order of magnitude larger than the contribution from the compact continuum sources. Taken at face value, however, the AGN can still only contribute about 18% of the necessary ionizing photons, unless the geometry is such that the AGN is obscured to the line of sight, but unobscured in the direction of the nebula (hence it is quoted as a lower limit).

The presence of both diffuse HeII and diffuse V_{606} continuum emission within the Ly α nebula itself may either be due to scattering processes, gravitational cooling radiation, or a spatially extended population of lower luminosity ionizing

sources below the detection limits of the HST imaging. We know that one other $\text{Ly}\alpha$ nebula does show evidence for a spatially extended stellar population (Matsuda et al., 2007). If the diffuse continuum is due to a stellar population, the mass of the population would need to be roughly $3.4 \times 10^9 M_\odot$ to match the observed V_{606} flux, assuming a 5-25 Myr single stellar population (solar metallicity; Bruzual & Charlot, 2003), and the corresponding ionizing photon flux from this stellar population would be 1×10^{52} photons s^{-1} . For solar metallicities, only in the case of a very young (5 Myr) stellar population with a mass of $3.7 \times 10^8 M_\odot$ would the ionizing photon flux begin to approach that required to explain the $\text{Ly}\alpha$ (1.3×10^{54} photons s^{-1}). In addition, Dey et al. (2005) point out that a spatially extended stellar population would need to be very young and very metal poor in order to explain the HeII emission as well (< 2 Myr, $Z < 10^{-7}$ Schaerer, 2003).

It does not seem likely that gravitational cooling dominates the ionization of this system. While the fact that the $\text{Ly}\alpha$ is over 10 times more extended than the HeII emission fits the picture of gravitational cooling radiation (Fardal et al., 2001; Yang et al., 2006), the lack of a central massive galaxy is inconsistent (Fardal et al., 2001; Furlanetto et al., 2005) and the $\text{HeII}/\text{Ly}\alpha = 0.13$ is higher than expected (Haiman et al., 2000; Yang et al., 2006). We note, however, that gravitational cooling may play a larger role in the outskirts of the system.

It is difficult to quantify the contribution of scattering to the diffuse continuum emission given the uncertainty in dust content, densities, and temperatures within this complex system. We do not attempt a detailed calculation here, but we note that the scattered light cannot exceed the total V_{606} continuum from all of the compact sources within the system. The flux of the diffuse V_{606} continuum

component ($2.2 \times 10^{44} \text{ erg s}^{-1}$) is a factor of 4 more than the total V_{606} continuum flux from the 8 well-detected compact sources thought to be at the redshift of the system ($6.0 \times 10^{43} \text{ erg s}^{-1}$) plus that from the AGN ($> 1.6 \times 10^{42} \text{ erg s}^{-1}$). While scattering likely contributes to the observed flux, it can only explain the entire diffuse continuum component if the flux from the AGN in the direction of the cloud is two orders of magnitude greater than that along the line of sight.

4.5 Conclusions

Using high resolution HST imaging we have taken a census of all the compact sources of ionization within a large $\text{Ly}\alpha$ nebula at $z \approx 2.656$. We find that the $\text{Ly}\alpha$ nebula system is surrounded by numerous compact galaxies with small sizes ($\approx 1 - 3 \text{ kpc}$) and disk-like morphologies, of which at least 8 are associated with the system. However, these continuum sources are all located tens of kiloparsecs from the peak of the $\text{Ly}\alpha$ emission and provide a negligible contribution to the ionization of the nebula. The $\text{Ly}\alpha$ nebula itself is smooth and shows no evidence for central knots or clumps that could explain the ionization. The source of HeII emission seen in a ground-based spectrum is likely spatially extended by 6-8 kpc. The diffuse $\text{Ly}\alpha$ and HeII emission is accompanied by diffuse V_{606} continuum emission which may be due to scattering or a spatially extended stellar population. At the conclusion of this study, the energetics of the system appear to be dominated either by an obscured AGN that is directed towards the cloud or by a combination of the AGN and a spatially extended stellar population. Understanding the full energetics of this complex system will require improved measurements of the color of the diffuse continuum emission and performing detailed photoionization modeling of the system.

CHAPTER 5

THE DISCOVERY OF A LARGE $\text{Ly}\alpha$ +HeII NEBULA AT $z \approx 1.67$: A CANDIDATE
LOW METALLICITY REGION?

We have discovered a ≈ 45 kpc $\text{Ly}\alpha$ nebula (or $\text{Ly}\alpha$ “blob”) at $z \approx 1.67$ which exhibits strong, spatially extended HeII emission and very weak CIV and CIII] emission. This is the first spatially extended $\text{Ly}\alpha$ +HeII emitter observed and the lowest redshift $\text{Ly}\alpha$ blob yet found. Strong $\text{Ly}\alpha$ and HeII $\lambda 1640$ emission in the absence of metal lines has been proposed as a unique observational signature of primordial galaxy formation (e.g., from gravitational cooling radiation or Population III star formation), but no convincing examples of spatially extended $\text{Ly}\alpha$ +HeII emitters have surfaced either in $\text{Ly}\alpha$ -emitting galaxy surveys at high redshifts ($z > 4$) or in studies of $\text{Ly}\alpha$ nebulae at lower redshifts. From comparisons with photoionization models, we find that the observed line ratios in this nebula are consistent with low metallicity gas ($Z \lesssim 10^{-2} - 10^{-3} Z_{\odot}$), but that this conclusion depends on the unknown ionization parameter of the system. The large HeII equivalent width ($\approx 37 \pm 10 \text{\AA}$) and the large HeII/ $\text{Ly}\alpha$ ratio (0.12 ± 0.04) suggest that the cloud is being illuminated by a hard ionizing continuum, either an active galactic nucleus (AGN) or very low metallicity stars, or perhaps powered by gravitational cooling radiation. Thus far there is no obvious sign of a powerful AGN in or near the system, so in order to power the nebula while remaining hidden from view even in the mid-infrared, the AGN would need to be heavily obscured. Despite the strong $\text{Ly}\alpha$ +HeII emission, it is not yet clear

This chapter originally appeared in Prescott, M. K. M., Dey, A., & Jannuzi, B. T. 2009, ApJ, 702, 554.

what is the dominant power source for this nebula. The system therefore serves as an instructive example of how the complexities of true astrophysical sources will complicate matters when attempting to use a strong $\text{Ly}\alpha + \text{HeII}$ signature as a unique tracer of primordial galaxy formation.

5.1 Introduction

Understanding primordial galaxy formation is a major science driver for the next generation of large space- and ground-based telescopes and has inspired a substantial amount of theoretical literature due to the potential contribution of the first generations of stars to reionization and the early stages of galaxy evolution. According to theoretical predictions, the observational signpost of primordial galaxy formation is the presence of strong $\text{Ly}\alpha\lambda 1216$ and $\text{HeII}\lambda 1640$ emission lines, either due to photoionization by very low metallicity and Population III (Pop III, i.e., zero metallicity) star formation (e.g., Tumlinson et al., 2001; Schaerer, 2003, 2008) or due to gas cooling during gravitational collapse (e.g., Haiman et al., 2000; Yang et al., 2006). In the case of Pop III stars, the strong $\text{Ly}\alpha$ and HeII is a direct consequence of the low metallicities, where, in the absence of metals, H and He become the dominant line coolants for the gas, and of the hot effective temperatures of Pop III stellar clusters, which are predicted to show a top-heavy initial mass function (IMF) and low stellar atmospheric opacity due to the lack of metals (e.g., Ezer & Cameron, 1971; Bromm et al., 2001). In the case of gravitational cooling radiation, $\text{Ly}\alpha$ and HeII are the primary ways for pristine gas to cool as it is collisionally excited during gravitational collapse; the predicted $\text{HeII}/\text{Ly}\alpha$ ratios may be as high as 10% (e.g., Haiman et al., 2000; Yang et al., 2006). Strong $\text{Ly}\alpha$ and HeII emission lines are commonly seen in other astro-

physical sources with hard ionizing continua, but at normal metallicities they are generally accompanied by strong metal lines such as C III] and C IV, as seen for example, in active galactic nuclei (AGN), radio galaxy halos, Wolf-Rayet (W-R) galaxies, or cases of shock ionization (e.g., Reuland et al., 2007; Leitherer et al., 1996; Dopita & Sutherland, 1996). The presence of strong Ly α and He II emission in the absence of strong metal lines has been put forward as a potentially unique observational signature of primordial galaxy formation.

Although theoretical studies suggest that Pop III and very low metallicity star formation may persist down to lower redshifts, this depends on the feedback efficiency, i.e., the ability of a Pop III stellar population to pollute the large-scale surroundings with metals (e.g., Tornatore et al., 2007). Searches for Pop III stars have understandably pushed to higher redshift ($z > 4$), where the Pop III star formation rate (SFR) density should increase dramatically relative to that found in the local universe (Scannapieco et al., 2003). Thus far, no unambiguous case of a Pop III stellar population has been observed. Several Ly α -emitting galaxy studies at $z \sim 4 - 5$ have uncovered sources with unusually high Ly α equivalent widths ($W_{rest} > 240 \text{ \AA}$) — larger than that expected from a normal stellar population — suggesting either a top-heavy IMF, a very low metallicity, and/or a very young age (Malhotra & Rhoads, 2002; Rhoads et al., 2003). However, the complicated radiative transfer of Ly α in a clumpy interstellar medium (ISM) could also be responsible for boosting the Ly α (Finkelstein et al., 2008), and in these studies, no corroborating evidence for the Pop III scenario in the form of a strong He II detection was found in either the individual or stacked LAE spectra, leaving the matter unresolved (Dawson et al., 2004; Ouchi et al., 2008). Deep spectroscopic observations of a strong Ly α -emitting galaxy at $z \approx 6.33$ showed no evidence for

HeII emission (Nagao et al., 2005), and a more recent Ly α +HeII dual emitter survey at $z \sim 4 - 5$ found no convincing candidates (Nagao et al., 2008). The limits from each of these studies suggest that Pop III star formation does not dominate in these $z \sim 4 - 5$ samples, prompting the authors to encourage searches at ever higher redshifts ($z \gtrsim 7$). Additional high redshift Ly α +HeII surveys are underway (e.g., di Serego Alighieri et al., 2008).

In this paper we report on the discovery of a $z \approx 1.67$ Ly α nebula with strong, spatially extended HeII emission and very weak C IV and C III] emission. This is the first spatially extended source that resembles the predicted Ly α +HeII signature of primordial galaxy formation. However, the system is more complex than it first appears. The observed line ratios suggest that the nebula may contain low metallicity gas, but this depends on the unknown ionization parameter of the system. Detailed analysis of the spectra along with extensive multiwavelength data reveals that the source of ionization is uncertain: the nebula is either an H II region ionized by a hard spectrum source, i.e., an AGN or a very low metallicity stellar population, or a gravitationally cooling cloud. The fact that multiwavelength follow-up observations are required in order to better constrain the source(s) of ionization and metallicity of the nebula has implications for Ly α +HeII searches at higher redshift. In Section 5.2, we summarize the systematic search for Ly α nebulae that led to this discovery and our observations and reductions. Section 5.3 contains a discussion of the observational results, and Section 5.4 details our analysis of the physical properties of the nebula. In Section 5.5, we discuss the implications of this discovery for the ongoing high redshift Ly α +HeII surveys, and we summarize our conclusions in Section 5.6.

We assume the standard Λ CDM cosmology ($\Omega_M=0.3$, $\Omega_\Lambda=0.7$, $h=0.7$); 1'' cor-

responds to a physical scale of 8.47 kpc at $z = 1.671$. All magnitudes are in the AB system. Unless otherwise stated, He II refers to He II $\lambda 1640 \text{ \AA}$, C IV to C IV $\lambda \lambda 1549, 1550$, C III] to C III] $\lambda 1909$, and Ne IV] to Ne IV] $\lambda 2424$.

5.2 Observations & Reductions

In this section, we discuss the observations that led to the discovery of this Ly α +He II nebula and the methods used to process the imaging and spectroscopic data.

5.2.1 The Search

Large Ly α nebulae (or Ly α “blobs”) — large (~ 100 kpc) clouds of gas emitting strongly in Ly α — are thought to be sites of ongoing galaxy formation and have been found in small numbers, primarily at $2 < z < 3$. Early theoretical work suggested that these nebulae could be examples of gravitationally cooling clouds (Haiman et al., 2000), and more recent cosmological hydrodynamic simulations indicated that cooling clouds should be detectable as Ly α +He II nebulae, although the specific predictions proved uncertain due to the treatment of star-forming gas (Yang et al. 2006; Y. Yang 2008, private communication). Several of the largest Ly α nebulae, including one with strong He II and C IV emission (Dey et al., 2005), have since been shown to be powered instead by AGN, spatially extended star formation, or some combination (e.g., Dey et al., 2005; Matsuda et al., 2007; Geach et al., 2007). Two groups claim to have discovered Ly α nebulae that are powered by gravitational cooling radiation (Nilsson et al., 2006; Smith & Jarvis, 2007; Smith et al., 2008), but neither case shows strong He II emission.

Ly α nebulae are extremely rare objects and have often been found using deep narrow-band imaging surveys of known galaxy overdensities. As such, their space density, particularly at the bright end of the luminosity function, is largely

unconstrained. In order to carry out an efficient but unbiased survey of a large cosmic volume, we have designed a systematic morphological search for spatially extended Ly α nebulae using the *broad-band* imaging from the NOAO Deep Wide-Field Survey (NDWFS; Jannuzi & Dey, 1999) Boötes Field. This field has been imaged in the B_W , R , and I band with median 5σ point-source depths of ≈ 27.1 , 26.3, and 25.8 mag (AB), respectively. In the sub-field relevant to this paper, the B_W , R , and I -band 5σ point-source depths are 27.5, 26.1, and 26.0 mag for 2.3, 1.7, and 2.8 hrs of integration, respectively. Candidates were selected from the broad-band data using a morphological and color selection algorithm, and spectroscopic follow-up was used to rule out low-redshift interlopers. The advantage of using broad-band data to search for line-emitting sources, a seemingly crude approach, is the enormous comoving volumes ($\sim 10^8 h_{70}^{-3} \text{ Mpc}^3$) that can be surveyed efficiently using publicly available data over wide fields. The success of the present survey relied heavily on the depth of the broad-band NDWFS imaging and the darkness of the sky within the B_W -band, against which strong line emission can dominate the flux even within the very broad B_W filter.

A full discussion of the search algorithm and results will be discussed elsewhere (Prescott et al. 2009, in preparation). Here we report on the discovery of a new Ly α +HeII nebula at $z \approx 1.67$ (hereafter denoted PRG1). Unlike the other Ly α sources found in our systematic search, the Ly α +HeII nebula presented here was selected by the search algorithm not because of its Ly α emission, which lies outside the B_W filter, but instead because of the strong and diffuse blue continuum emission ($\approx 92\%$) and spatially extended HeII emission ($\approx 8\%$) within the bandpass. Postage stamps from GALEX (FUV & NUV; *Galaxy Evolution Explorer*, Martin et al., 2005), NDWFS (B_W , R , and I), and the Spitzer Deep Wide-Field

Survey (SDWFS; IRAC $3.6\mu\text{m}$, $4.5\mu\text{m}$, $5.8\mu\text{m}$, and $8.0\mu\text{m}$; Ashby et al., 2009) are shown in Figure 5.1. The GALEX limits are $0.36\ \mu\text{Jy}$ in the NUV and FUV bands; the SDWFS limits are 3.2, 4.4, 25.5, and $25\ \mu\text{Jy}$ (5σ). The Spitzer MIPS coverage of this region shows no detection with a 1σ root-mean-square (rms) limit of $51\ \mu\text{Jy}$ (E. Le Floch 2008, private communication).

5.2.2 Spectroscopic Follow-up

We obtained spectroscopic follow-up observations using the MMT and the Blue Channel Spectrograph during UT 2008 June 8-9 as part of our systematic search for $\text{Ly}\alpha$ nebulae. We used a $1.5\times 120''$ (unvignetted) slit and the $300\ \text{l mm}^{-1}$ grating ($\lambda_c \approx 5713\text{\AA}$, $\Delta\lambda \approx 3100 - 8320\text{\AA}$). We chose a slit orientation that spanned the longest dimension of the diffuse emission (Position Angle= 81.2° , observed near transit), as shown in Figure 5.1, while also intersecting a nearby bright object. We moved the target along the slit by $\approx 5''$ in between exposures.

Conditions during the first night were clear and stable with $1''.0$ seeing; the second night was clear but with variable seeing ($\gtrsim 1''.3$) and high winds which caused shaking of the telescope pointing. We show in Section 3.2 that, due to a slight pointing offset and wind-shake, the data from the second night sample a different spatial region within the nebula and are contaminated at some level by sources nominally off the slit, in particular a red compact source to the West-Northwest (Source A in Figure 5.1). For this reason, data from the two nights were reduced and analyzed separately. The most robust $\text{Ly}\alpha$ and HeII flux measurements are from the first night, when conditions were excellent during the single half hour exposure. An additional 1.5 hr of integration were obtained during the second night. The $\text{Ly}\alpha$ flux measurement from Night 2 shows a 25% loss relative to that from Night 1. In the remainder of the paper, we use the $\text{Ly}\alpha$ and

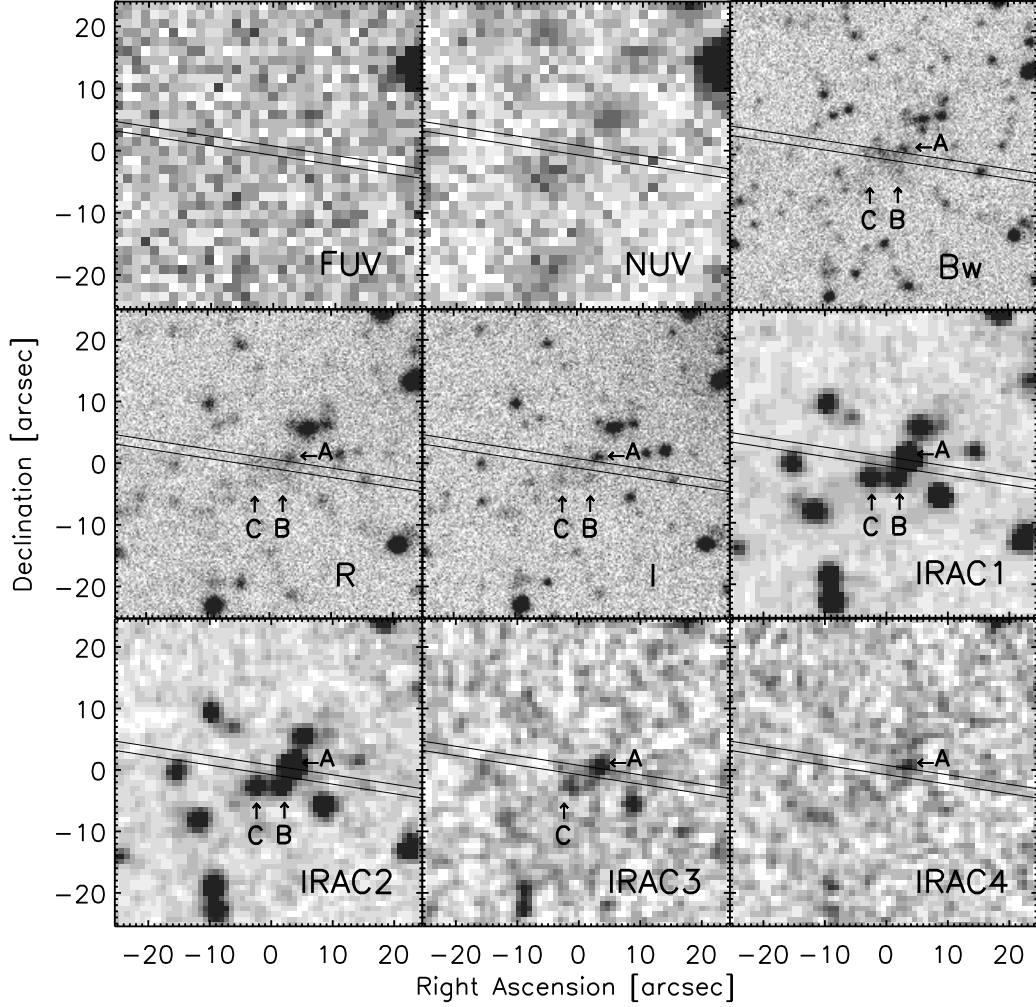


Figure 5.1 *GALEX* (*FUV* and *NUV*), NDWFS broad-band optical (B_W , R , and I), and IRAC ($3.6\mu\text{m}$, $4.5\mu\text{m}$, $5.8\mu\text{m}$, and $8.0\mu\text{m}$) postage stamps for PRG1. Images are all $1'$ on a side. The spectroscopic slit is shown with a position angle of 81.2° . PRG1 was selected as a $\text{Ly}\alpha$ nebula candidate due to the diffuse blue emission in the B_W imaging. However, in this case $\text{Ly}\alpha$ is in fact outside the B_W band; the B_W flux is instead dominated by diffuse continuum and HeII emission. The diffuse blue continuum emission is clearly visible in the NDWFS B_W -band imaging. Several compact sources in the near vicinity of the nebula have IRAC counterparts, labeled A, B, and C.

HeII flux measurements from Night 1 but include the line ratios derived from both nights.

The data were reduced using IRAF¹. After performing the overscan and bias subtraction, we corrected flat-field exposures for the response of the internal ‘Bright Continuum’ flat-field lamp by dividing out the median along columns and then applied the flat-field correction. We used twilight flats to determine the illumination correction for the science frames. Cosmic rays were removed using *xzap*². The wavelength solution was determined using HeArNe and HgCd comparison lamps, with an rms of $\approx 0.17 \text{ \AA}$. We corrected the data for a slight systematic offset in the night sky lines; the night sky line wavelengths in the final spectra are correct to $\pm 0.3 \text{ \AA}$. Flux calibration was based on observations of the standard stars BD+33 2642 and Wolf 1346³. We applied a grey shift ($\lesssim 0.08 \text{ mag}$) and fit the sensitivity function using extra care at the blue end of the spectrum because the Ly α line at $\approx 3250 \text{ \AA}$ lies only 56.3 pixels (109.7 \AA) from the edge of the chip. The instrumental resolution measured from the Hg I $\lambda 4047$ line is 3.6 \AA , and the tilt within the aperture is $\leq \pm 5.24 \text{ km s}^{-1}$ over the region of the nebula.

5.3 Results

5.3.1 Ly α and He II Emission

The final two-dimensional and one-dimensional spectra from the first and second night are shown in Figures 5.2 and 5.3. The spectra show strong Ly α and HeII emission lines, both of which exhibit similar kinematic structure in the two-

¹IRAF is distributed by the National Optical Astronomy Observatories, which are operated by the Association of Universities for Research in Astronomy, Inc., under cooperative agreement with the National Science Foundation.

²<http://iraf.noao.edu/iraf/ftp/iraf/extern/xdimsum020627>

³KPNO IRS Standard Star Manual

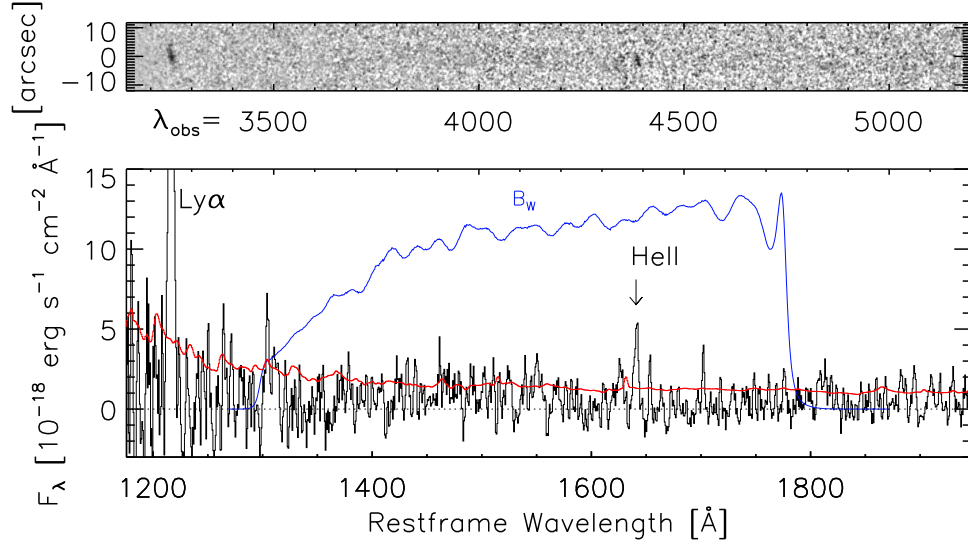


Figure 5.2 Night 1 (UT 2008 June 08) two-dimensional and one-dimensional spectra showing strong $\text{Ly}\alpha$ and HeII emission from a single half hour exposure ($1.5 \times 5.0''$ aperture). The spectra have been smoothed by $0.84''$ spatially and by 5.8 \AA in the spectra dimension. The filter curve is the B_W bandpass convolved with the atmospheric transmission (blue). The 1σ error spectrum is overlaid (red).

dimensional spectrum. The measured fluxes and flux limits were derived separately from each night's data using a $1.5 \times 5.0''$ aperture, chosen to maximize the signal-to-noise ratio of the HeII measurement (Table 5.1). Faint continuum emission is detected in the spectra (Figure 5.3). We scaled the spectra by a factor of 1.4 and 1.6, respectively, in order to match the continuum fluxes measured from the much deeper NDWFS broad-band data within the region covered by the slit (Table 5.2).

The $\text{Ly}\alpha$ and HeII luminosities from Night 1 are $L_{\text{Ly}\alpha} = L_{\text{Ly}\alpha,ap} \times f_{geo} \times f_{profile} \approx 5.4 \times 10^{43} \text{ erg s}^{-1}$ and $L_{\text{HeII}} = L_{\text{HeII},ap} \times f_{geo} \approx 4.0 \times 10^{42} \text{ erg s}^{-1}$.

Table 5.1. Spectroscopic Measurements of a Ly α +He II Nebula at $z \approx 1.67$

	Ly α λ 1216	Nv λ 1240	Siv λ 1398	Civ λ 1549	HeII λ 1640	CIII] λ 1909	NeIV λ 2424
Night 1 - UT 2008 June 08							
Flux[10^{-17} erg s $^{-1}$ cm $^{-2}$]	49.9 ± 5.7	$< 6.4^b$	$< 1.8^b$	$< 1.4^b$	6.2 ± 1.7	$< 1.2^b$	$< 1.4^b$
EW $_{rest}$ [Å]	294.1 ± 39.4	-	-	-	36.8 ± 10.1	-	-
λ_{obs} [Å]	3250.07 ± 0.56	-	-	-	4383.07 ± 1.25	-	-
Redshift	1.6735 ± 0.0005	-	-	-	1.6714 ± 0.0008	-	-
FWHM $_{obs}$ [Å]	10.20 ± 0.82	-	-	-	8.41 ± 3.23	-	-
FWHM [km s $^{-1}$]	941.5 ± 75.5	-	-	-	575.5 ± 221.1	-	-
Night 2 - UT 2008 June 09							
Flux[10^{-17} erg s $^{-1}$ cm $^{-2}$]	43.6 ± 4.0	$< 5.5^b$	$< 1.1^b$	2.1 ± 1.1	5.7 ± 0.9	4.7 ± 0.8	2.8 ± 1.0
EW $_{rest}$ [Å]	257.1 ± 29.4	-	-	12.4 ± 6.5	33.9 ± 6.1	28.0 ± 5.3	29.9 ± 11.3
λ_{obs} [Å]	3249.59 ± 0.38	-	-	4142.30 ± 1.46	4381.92 ± 0.76	5095.26 ± 0.10	6476.81 ± 1.83
Redshift	1.6731 ± 0.0003	-	-	1.6724 ± 0.0009	1.6707 ± 0.0005	1.6695 ± 0.0001	1.6720 ± 0.0008
FWHM $_{obs}$ [Å]	9.75 ± 0.71	-	-	-	6.36 ± 0.64	23.28 ± 1.94	-
FWHM [km s $^{-1}$]	900.4 ± 65.1	-	-	-	435.5 ± 44.1	1370.7 ± 114.5	-

^aFlux measured in a $1.5 \times 5.0''$ aperture. No correction has been applied for Ly α absorption.

^bQuoted upper limits are 1σ values.

Table 5.2. Photometric Measurements of a Ly α +He II Nebula at $z \approx 1.67$

	Nebula ^{a,b}	Source A ^c
	$10^{-30} \text{ erg s}^{-1} \text{ cm}^{-2} \text{ Hz}^{-1}$	$10^{-30} \text{ erg s}^{-1} \text{ cm}^{-2} \text{ Hz}^{-1}$
B_W	3.58 ± 0.24	2.07 ± 0.14
R	4.03 ± 0.49	4.60 ± 0.33
I	6.62 ± 0.88	8.35 ± 0.47
$3.6\mu\text{m}$	-	466.56 ± 34.13
$4.5\mu\text{m}$	-	488.70 ± 32.40
$5.8\mu\text{m}$	-	329.67 ± 31.40
$8.0\mu\text{m}$	-	194.13 ± 25.60

^aFlux measured within the same $1.5 \times 5.0''$ aperture as the spectroscopic measurements.

^bThe contribution of line emission for Night 1 (Night 2): He II contributes 8% (7%) and C IV < 2% (3%) of the B_W emission, and Ne IV] contributes < 2% (6.5%) of the R -band emission. We see no contribution from line emission out to the middle of the I -band (8300\AA , the extent of our spectroscopic coverage).

^cOptical B_W , R , and I fluxes were measured within $2.1''$ diameter apertures. Mid-infrared fluxes (3.6 , 4.5 , 5.8 , $8.0 \mu\text{m}$) were measured within $3.5''$ diameter apertures. Aperture corrections are discussed in the text.

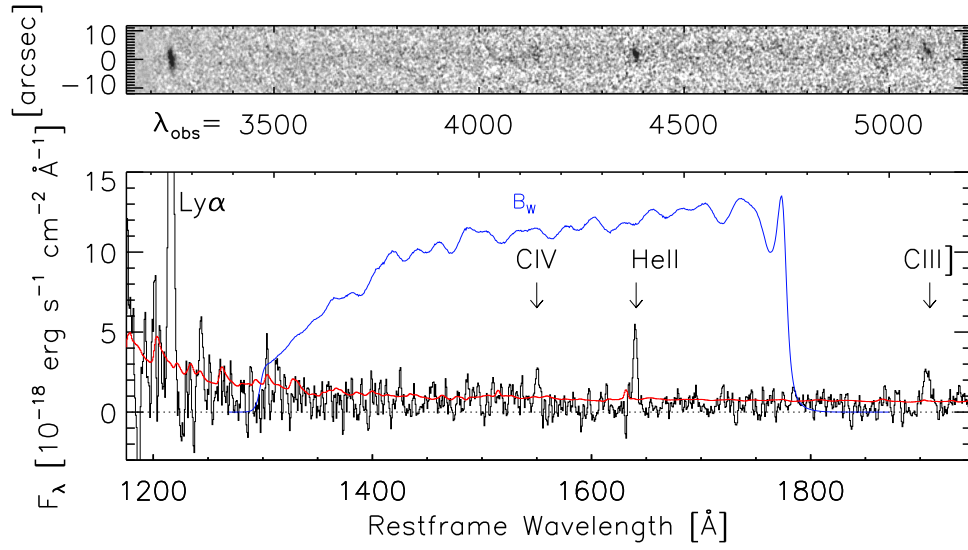


Figure 5.3 Night 2 (UT 2008 June 09) two-dimensional and one-dimensional spectra showing strong $\text{Ly}\alpha$ and HeII emission, weak $\text{CIII}]$, and marginally-detectable CIV from a combined 1.5 hour exposure ($1.5 \times 5.0''$ aperture). The spectra are smoothed by $0.84''$ spatially and by 5.8 \AA in the spectral dimension. The filter curve is the B_W bandpass convolved with the atmospheric transmission (blue). The 1σ error spectrum is overlaid (red). When comparing to Figure 5.2, note that a 180° change in the slit position angle between the two nights caused a flip in the angle of the spectral trace across the detector.

$L_{Ly\alpha,ap} = 9.3 \times 10^{42} \text{ erg s}^{-1}$ and $L_{HeII,ap} = 1.2 \times 10^{42} \text{ erg s}^{-1}$ are the luminosities measured within the spectroscopic aperture, f_{geo} is the geometric correction factor between the spectroscopic aperture and full extent of the nebula, and $f_{profile}$ corrects for asymmetry in the $Ly\alpha$ profile due to blue side absorption. We discuss the estimation of these correction factors below.

The geometric correction factor f_{geo} was derived from a comparison of the spatial extent of the nebula measured in the $Ly\alpha$ line versus the extent in the B_W imaging. In our best seeing Night 1 data, where we have accurate spatial information and low slit losses, the $Ly\alpha$ is extended by $\approx 5''$ (42.3 kpc) with a fairly sharp truncation at large radii, but with a possible extension toward the west (right of center, Figure 5.4). The HeII emission is weaker than the $Ly\alpha$ by a factor of 10, but it appears that at lower signal-to-noise the HeII nebula extends to roughly the same radius as the core of the $Ly\alpha$ nebula (no westward extension). The Night 2 data show a $Ly\alpha$ extent of $\approx 6''$ and a HeII extent of $\approx 5''$ but suffer from slit losses and degraded spatial resolution due to poor seeing and wind-shake. The extent of the $Ly\alpha$ nebula in the spectroscopic observations is in rough agreement with the spatial extent of the diffuse emission measured from the broad-band B_W data along the position of the slit ($\approx 6.6''$, ≈ 56 kpc above a B_W surface brightness of $4.5 \times 10^{-16} \text{ erg s}^{-1} \text{ cm}^{-2} \text{ arcsec}^{-2}$). The full area of the diffuse emission in the B_W imaging is ≈ 26 square arcseconds. Assuming that the $Ly\alpha$ emission is distributed similarly to the B_W continuum emission, we estimated that a geometric correction factor of $f_{geo} = 3.4$ is required to obtain the total $Ly\alpha$ flux from the nebula. This correction is very approximate; narrow-band imaging and/or spatially-resolved spectroscopy will be required to accurately account for the contributions of line and continuum emission to different portions of the neb-

ula.

We derived the $\text{Ly}\alpha$ blue side absorption correction f_{profile} using a comparison of the $\text{Ly}\alpha$ and HeII line centroids. The $\text{Ly}\alpha$ profile is fairly symmetric (Figure 5.5), but the center of the $\text{Ly}\alpha$ line is offset to the red from the systemic redshift, as determined from the centroid of the HeII emission line, likely due to absorption. We estimated the amount of blue side absorption of $\text{Ly}\alpha$ by mirroring the red side of the $\text{Ly}\alpha$ profile across the line centroid, and derived a factor of 1.7 (Night 1) and 1.8 (Night 2) increase in the $\text{Ly}\alpha$ flux. We therefore used a correction factor of $f_{\text{profile}} = 1.7$ to obtain the final Night 1 $\text{Ly}\alpha$ luminosity.

The nebula shows clear velocity structure in both the $\text{Ly}\alpha$ and HeII lines. The lines are resolved, showing $\text{Ly}\alpha$ and HeII velocity dispersions of $\sigma_v \approx 400$ and 250 km s^{-1} , respectively, corrected for the instrumental resolution. Figure 5.6 shows the velocity profile of the $\text{Ly}\alpha$ line from Night 1 and Night 2 derived using 2 pixel ($0.56''$) extractions. The profile is relatively smooth but flattens on the east (left) of center. The spatially-resolved $\text{Ly}\alpha$ velocity dispersion is essentially constant across the nebula.

5.3.2 C IV, C III], and Ne IV] Emission

Despite the strong $\text{Ly}\alpha$ and HeII emission seen in the Night 1 data, there is no detection of C III], C IV, or Ne IV]. The 1σ upper limits on the line ratios are $\text{CIV}/\text{HeII} < 0.23$, $\text{CIII}]/\text{HeII} < 0.19$, and $\text{NeIV}]/\text{HeII} < 0.23$. Due to the excellent and stable observing conditions during Night 1, the Night 1 spectrum provides the most accurate flux measurements for $\text{Ly}\alpha$ and HeII along with higher resolution kinematic information and the strongest limits on the C III], C IV, and Ne IV] emission from the source. In contrast, the Night 2 spectrum shows weak C III] and marginal C IV and Ne IV] emission at the same redshift. The resulting line ra-

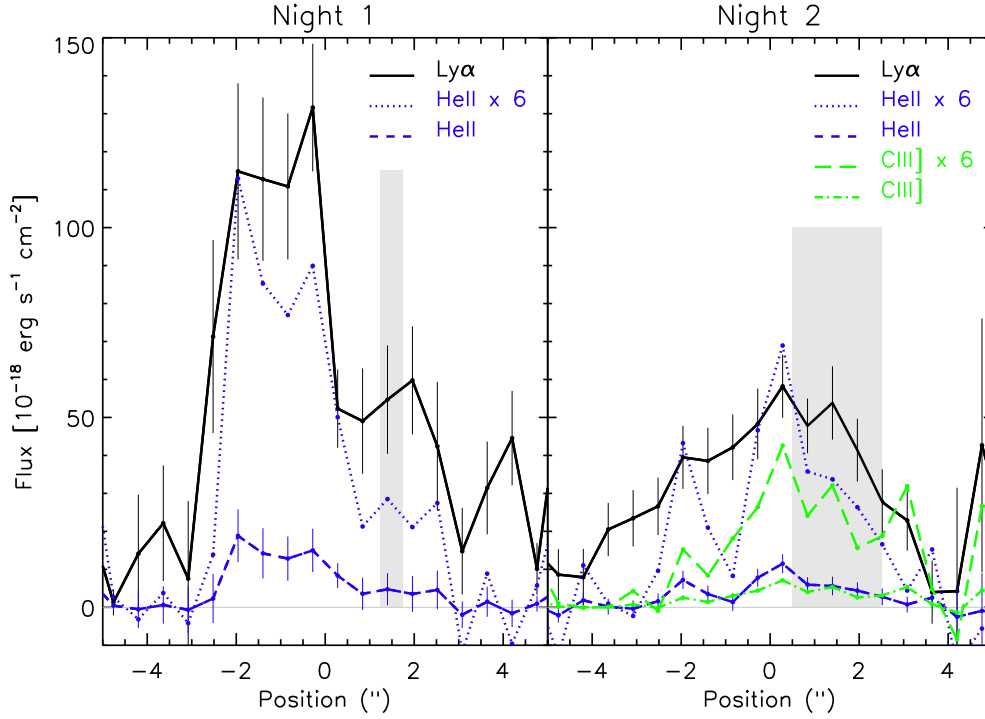


Figure 5.4 $\text{Ly}\alpha$ and HeII spatial profiles with errors as a function of position along the slit from the Night 1 (UT 2008 June 08) and Night 2 (UT 2008 June 09). As CIII] was not detected on Night 1, the CIII] profile is shown for Night 2 only. HeII and CIII] profiles scaled by a factor of 6 are also overplotted to allow easier comparison with the $\text{Ly}\alpha$ profile. The HeII region appears to be comparable in size to the $\text{Ly}\alpha$ region. The shaded area represents the approximate position of Source A, a source that was off-slit but that may have contaminated the Night 2 observations due to poor seeing and windy conditions. The discrepancy between the spatial profiles and the offset of the CIII] spatial profile relative to the $\text{Ly}\alpha$ are both consistent with the hypothesis that the Night 2 spectrum is contaminated by light from Source A and that Source A may be the primary source of the metal line emission.

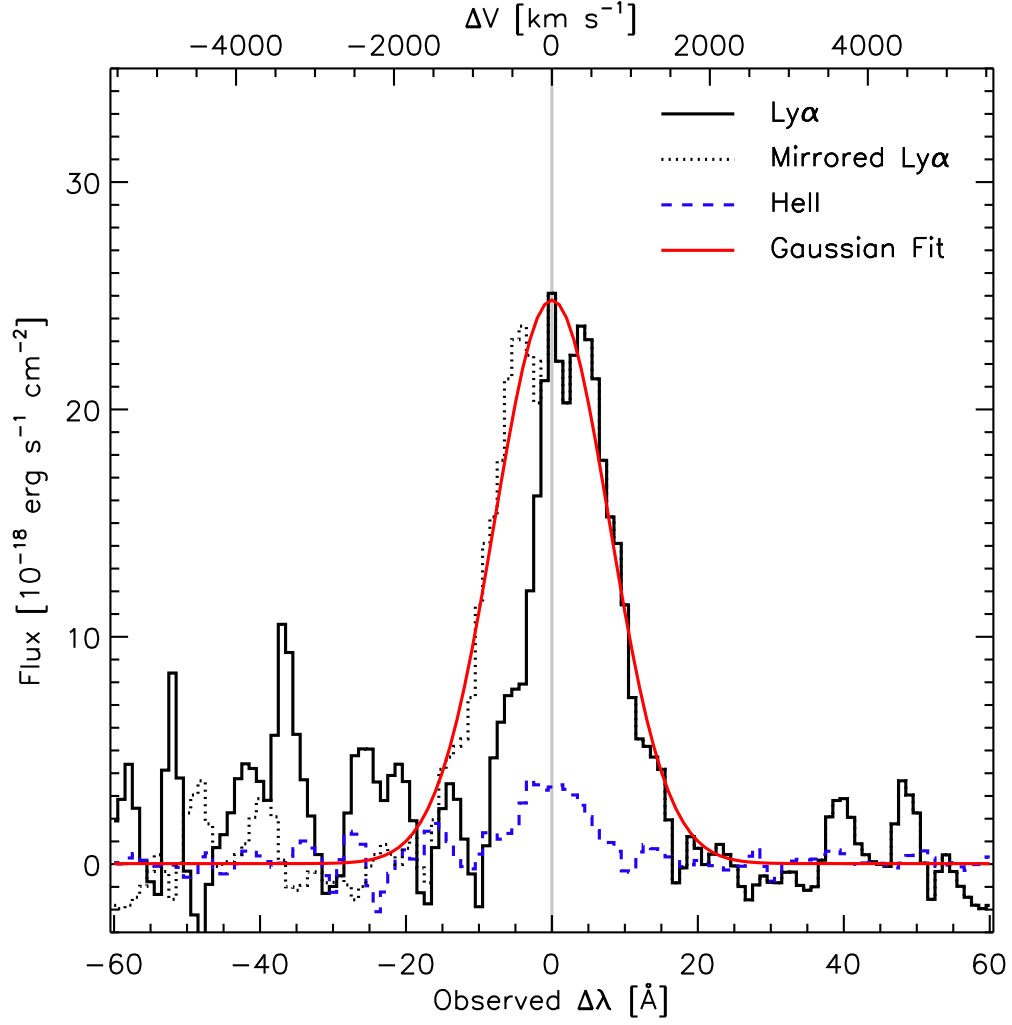


Figure 5.5 Ly α (black solid line) and HeII (blue dashed line) line profiles as a function of observed wavelength centered on the systemic redshift of the system, as measured from the HeII line. The observed Ly α is shown with the mirror image of the long-wavelength half of the line superimposed (black dotted line). A Gaussian fit (red solid line) indicates that the Ly α line may be absorbed by $\sim 41\%$. The corresponding velocity offsets for Ly α are given on the top axis.

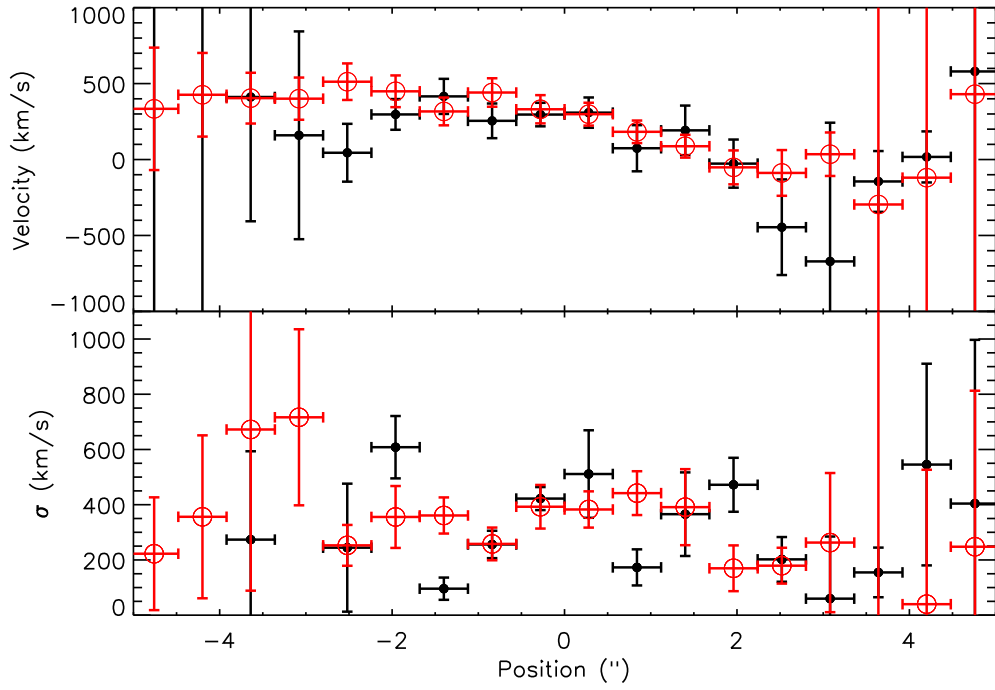


Figure 5.6 Velocity and velocity dispersion spatial profiles of the $\text{Ly}\alpha$ line for Night 1 (UT 2008 June 08; black filled circles) and Night 2 (UT 2008 June 09; red open circles) derived from spectra extractions taken in 2 pixel ($0.56''$) spatial bins and corrected for the instrumental resolution. The velocity zeropoint was set using the redshift calculated from the HeII line centroid in the full $5.0''$ aperture extraction.

tios are $\text{CIV}/\text{HeII} = 0.36$, $\text{CIII]}/\text{HeII} < 0.82$, and $\text{NeIV]}/\text{HeII} < 0.49$. The Night 2 data provide additional constraints on the line ratios but must be treated with care due to the Night 2 observing conditions. Due to the poor seeing and the wind-shake of the telescope, the Night 2 spectrum suffers from slit losses as well as contamination from nearby sources nominally off the slit, most importantly from a compact red source to the WNW of the target center (Source A; see Figure 5.1).

From a comparison of the line ratios derived from each night, we argue that the metal line emission is not from the same spatial location as the $\text{Ly}\alpha$ and HeII , and may instead be associated with the region closer to Source A. On Night 2, the $\text{CIII]}/\text{HeII}$ ratio was 0.82; thus if the emission were perfectly cospatial, we should have detected CIII] on Night 1 at $\approx 5.1 \times 10^{-17} \text{ erg s}^{-1} \text{ cm}^{-2}$, roughly the same significance as HeII . Instead, we can rule out CIII] emission at the 4.3σ level. For NeIV] , we should have detected it at $3.0 \times 10^{-17} \text{ erg s}^{-1} \text{ cm}^{-2}$ on Night 1, which disagrees at the 2.2σ level with our Night 1 result. We cannot make a robust comparison for CIV , as it is only detected at the 2σ level even on Night 2, but we make the assumption that all the metal line emission originates from the same source. In contrast, the $\text{HeII}/\text{Ly}\alpha$ line ratios are consistent between the two nights (0.12 ± 0.04 and 0.13 ± 0.02 , respectively), indicating that the $\text{Ly}\alpha$ and HeII are indeed cospatial within the region sampled by these observations even though the metal line emission varies spatially.

The offsets in the spatial profiles of the lines are consistent with the idea that the data from the two nights sampled different spatial regions. If the CIV , CIII] , and NeIV] lines are from the region around Source A and if the wind-shake was consistently perpendicular to the slit, there should be a ≈ 5.2 pixel ($1.5''$ West)

offset between the spatial centroid of these lines and that of $\text{Ly}\alpha$. However, this offset will vary by an estimated $\approx \pm 3.6$ pixels ($\approx 1''$) or more depending on the direction of the telescope wind-shake relative to the angle of the slit during a given exposure. We do see a difference between the two nights when we look at the spatial profiles extracted in 2 pixel spatial bins along the spatial direction (Figure 5.4); the Night 1 profile is skewed towards the East (left, away from Source A), whereas the Night 2 profile is peaked closer to the position of Source A, suggesting contamination. We use these spatial profiles to compute flux-weighted mean spatial centroids for each emission line separately. The HeII position is consistent with that of $\text{Ly}\alpha$ to within 1σ ($\Delta x = 1.41 \pm 1.54$ pixels, $0.40 \pm 0.43''$). The CIII] offset is 4.03 ± 2.07 pixels ($1.13 \pm 0.58''$) in the direction of Source A. (Due to the intrinsic faintness of the CIV and NeIV] lines, the computed offsets are not statistically significant.) Follow-up observations will be required to resolve this issue, but it appears that the CIII] line is offset from the spatial centroid of the $\text{Ly}\alpha$ at the 1.9σ level, in the right direction and at roughly the correct position to be explained by contamination from the region closer to Source A.

Given the pointing uncertainty and inevitability of contamination from sources off the slit due to the unstable conditions on Night 2, the discrepancy in the spatial profiles between the two nights, the evidence that the CIII] line shows a spatial offset consistent with the position of Source A, and the fact that the Night 1 data are inconsistent with the fluxes of NeIV] and CIII] measured on Night 2 at $\sim 2-4\sigma$, we argue that much of the metal line emission derives from the region around Source A. We cannot rule out that some is emitted further out in the nebula, but even if it does, it arises from a region spatially distinct from the region observed on Night 1. Combining the data from the two nights would not be appropri-

ate due to the different spatial sampling of the observations and these intrinsic spatial inhomogeneities. In the absence of more definitive data, we use the metal emission line measurements from both nights as independent upper limits on the emission coming from two possibly distinct regions of the nebula.

5.4 Discussion

In this section we derive estimates for the physical properties of PRG1 and use photoionization models to gain insight into the gas metallicity and the possible source(s) of ionization. Despite the strong $\text{Ly}\alpha + \text{HeII}$ signature and weak metal line emission often associated with primordial phenomena, we find that it is not possible to make an unambiguous determination of the source of ionization. The line ratios are consistent with a nebula comprised of low (but non-zero) metallicity gas, irrespective of the nature of the ionizing source, but this conclusion depends on the unknown ionization parameter of the system.

5.4.1 Physical Properties of the Nebula

Our discovery data can be used to put constraints on the physical properties of the nebula. Using the emission measure of $\text{Ly}\alpha$, we can estimate the electron density.

$$L_{\text{Ly}\alpha} = \frac{j_{\text{Ly}\alpha}}{j_{\text{H}\beta}} n_p n_e f V h \nu_{\text{H}\beta} \alpha_{\text{H}\beta}^{eff}, \quad (5.1)$$

$$\approx 1.2 \frac{j_{\text{Ly}\alpha}}{j_{\text{H}\beta}} n_e^2 f V h \nu_{\text{H}\beta} \alpha_{\text{H}\beta}^{eff}, \quad (5.2)$$

where $j_{\text{Ly}\alpha}$ and $j_{\text{H}\beta}$ are the emission coefficients for $\text{Ly}\alpha$ and $\text{H}\beta$, respectively, n_p and n_e are the proton and electron number densities with $n_e \approx 1.2 n_p$ (the factor of 1.2 accounts for the contribution of electrons from doubly ionized Helium), f is the volume filling factor of the nebula, V is the volume of the nebula, h is Planck's

constant, $\nu_{H\beta}$ is the frequency of $H\beta$, and $\alpha_{H\beta}^{eff}$ is the effective recombination coefficient for $H\beta$ (Osterbrock, 1989). We approximate the nebula as a sphere with radius $R \approx 28.0$ kpc. The $\text{Ly}\alpha$ luminosity extrapolated to the entire nebula and corrected for blue side absorption ($5.4 \times 10^{43} \text{ erg s}^{-1}$) corresponds to an electron number density of $n_e \approx 0.094f^{-0.5} \text{ cm}^{-3} \approx 29.7(f/10^{-5})^{-0.5} \text{ cm}^{-3}$, where we have used a typical value for f derived for the line-emitting regions in cluster cooling flows ($\sim 10^{-5}$; e.g., Heckman et al., 1989). This corresponds to an ionized gas mass of $M_{ion}=1.25m_p n_e fV = 8.4 \times 10^8 (f/10^{-5})^{0.5} M_\odot$.

Similarly, the HeII emission measure can be used to estimate the He^{++} and electron densities, assuming the cosmic mass fraction of He,

$$L_{\text{HeII}\lambda 1640} = \frac{j_{\lambda 1640}}{j_{\lambda 4686}} n_{\text{He}^{++}} n_e fV h\nu_{\lambda 4686} \alpha_{\lambda 4686}^{eff}, \quad (5.3)$$

$$\approx \frac{j_{\lambda 1640}}{j_{\lambda 4686}} (14) n_{\text{He}^{++}}^2 fV h\nu_{\lambda 4686} \alpha_{\lambda 4686}^{eff}, \quad (5.4)$$

where $j_{\lambda 1640}$ and $j_{\lambda 4686}$ are the emission coefficients, $n_{\text{He}^{++}}$ and n_e are the He^{++} and electron number densities with $n_e \approx 1.2n_p \approx 14n_{\text{He}^{++}}$, $\nu_{\lambda 4686}$ is the frequency of $\text{HeII}\lambda 4686$, and $\alpha_{\lambda 4686}^{eff}$ is the $\text{HeII}\lambda 4686$ effective recombination coefficient (Osterbrock, 1989). The HeII luminosity extrapolated to the whole nebula ($4.0 \times 10^{42} \text{ erg s}^{-1}$) corresponds to a He^{++} number density of $n_{\text{He}^{++}} \approx 1.0(f/10^{-5})^{-0.5} \text{ cm}^{-3}$ and an electron number density of $n_e \approx 14.5(f/10^{-5})^{-0.5} \text{ cm}^{-3}$. This corresponds to an ionized gas mass of $M_{ion}=1.25m_p n_e fV = 4.1 \times 10^8 (f/10^{-5})^{0.5} M_\odot$, roughly consistent with the $\text{Ly}\alpha$ estimate.

If we make the naive assumption that the velocity spread results from rotation with $V_c \approx \Delta V/2 = 350 \text{ km s}^{-1}$ at a radius of 28 kpc ($3.3''$), we estimate the mass interior to this radius to be $M_{rot} = 8.0 \times 10^{11} \sin^2 i M_\odot$, where i is the inclination of the system. If the velocity dispersion is due to random motions of small clouds

within the system, we estimate the dynamical mass (using the more kinematically robust HeII line; $\sigma_v = 245 \text{ km s}^{-1}$) to be $M_{rand} = 1.9 \times 10^{12} M_{\odot}$.

The spatial extent of the Ly α (H $^+$) and HeII (He $^{++}$) emitting regions appear to be similar in size, certainly within a factor of 2 ($R_{H^+}/R_{He^{++}} \lesssim 2$). This is somewhat surprising when we consider a simple Strömngren sphere argument. Assuming a hard central ionizing source (an AGN or a Pop III SED) embedded within an infinite spherical H+He cloud, the predicted size ratio of the H $^+$ and He $^{++}$ -emitting regions is $R_{H^+}/R_{He^{++}} \sim 9 - 17$, an order of magnitude higher than we observe. This suggests that either the H $^+$ region is density-bounded, that the sources of ionization are distributed throughout the nebula, or that the assumption of spherical symmetry is invalid (e.g., the cloud is illuminated from the outside).

The observed Ly α luminosity ($L_{Ly\alpha} = 5.4 \times 10^{43} \text{ erg s}^{-1}$) corresponds to a H-ionizing photon flux ($13.6 \text{ eV} \leq E_{\gamma} \leq 54.4 \text{ eV}$) of

$$Q(H) = \frac{L_{Ly\alpha}}{h\nu_{Ly\alpha}} \frac{1}{0.68} \approx 4.9 \times 10^{54} \text{ photons s}^{-1}, \quad (5.5)$$

where we have assumed that the fraction of H ionizing photons converted into Ly α is 0.68 (Spitzer, 1978). We note that this is likely a lower limit due to a number of considerations: Ly α is highly susceptible to resonant scattering and is easily destroyed by dust, and Ly α for this system is observed at $\approx 3250 \text{ \AA}$, a wavelength regime that suffers from very low atmospheric transmission and poor CCD sensitivity, making accurate flux calibration difficult.

From the observed HeII emission ($L_{HeII} = 4.0 \times 10^{42} \text{ erg s}^{-1}$), we calculate a He $^+$ -ionizing photon flux ($E_{\gamma} \geq 54.4 \text{ eV}$) of

$$Q(He^+) = \frac{L_{\lambda 1640}}{h\nu_{\lambda 1640}} \frac{\alpha_{HeII}^{eff}}{\alpha_{HeII}^{1640}} \approx 6.2 \times 10^{53} \text{ photons s}^{-1}, \quad (5.6)$$

where $\alpha_{HeII}^{eff} = 1.53 \times 10^{-12} \text{ cm}^3 \text{ s}^{-1}$ (case B; 100 cm^{-3} , 10^4 K ; Storey & Hummer, 1995) and $\alpha_{HeII}^{\lambda 1640} = \alpha_{HeII}^{4686} \frac{j_{\lambda 1640}}{j_{\lambda 4686}} \frac{\nu_{\lambda 4686}}{\nu_{\lambda 1640}} = 8.08 \times 10^{-13} \text{ cm}^3 \text{ s}^{-1}$ (case B; Osterbrock, 1989).

The large value of $Q(He^+)/Q(H)=0.13$ is strong evidence that the source is illuminated by a hard ionizing continuum. The prediction for a Pop II stellar population (instantaneous burst, Salpeter IMF, $1-100 M_{\odot}$, $Z = 0.001$; Schaerer, 2003) is $Q(He^+)/Q(H)= 0.0004$; while our $Ly\alpha$ measurement may be compromised by radiative transfer effects and poor flux calibration at the edge of the atmospheric cut-off, it would need to have been underestimated by more than a factor of 100 in order for the observed $Q(He^+)/Q(H)$ to match that of a normal Pop II stellar population. The observed $Q(He^+)/Q(H)$ is in the range expected for AGN or Pop III stars. A typical AGN template has a ratio of $Q(He^+)/Q(H)\sim 0.09$ (Elvis et al., 1994), more consistent with the observational constraint. While normal metallicity stellar populations will have very little flux above the He^+ ionization edge, Pop III stars are predicted to have much harder spectra due to high temperatures, low stellar atmospheric opacity, and a top-heavy IMF. Strong mass loss from these stars would cause higher effective temperatures, boosting the hard ionizing photons even further. Schaerer (2002) calculated a suite of Pop III models, both with and without strong mass loss. For individual high mass stars ($M \geq 80-300 M_{\odot}$) they predict $Q(He^+)/Q(H) \geq 0.022-0.11$. Models with mass loss yields ratios of $Q(He^+)/Q(H) \geq 0.06-0.17$ ($80-300 M_{\odot}$). However, such large $Q(He^+)/Q(H)$ ratios persists for only a few megayears for instantaneous burst models. Constant star-forming Pop III models (with no mass loss) integrated over a range of IMFs yield $Q(He^+)/Q(H) \leq 0.04$, and the value decreases with increasing metallicity (Schaerer, 2003). There are numerous uncertainties in these estimates, but

broadly speaking the observed $Q(\text{He}^+)/Q(\text{H})$ ratio is in the range populated only by AGN and the very lowest metallicity stellar populations.

5.4.2 Photoionization Modeling

The ubiquity of AGN, the association of AGN and extended emission line regions (EELRs), and the presence of spatially varying metal line emission suggest that an AGN is a plausible source of ionization. At the same time, the observed line ratios are highly unusual and have been tied in the theoretical literature to primordial galaxy formation processes (the presence of Pop III stars or gravitational cooling radiation). A comparison of the line ratios from PRG1 with those of radio galaxy EELRs and other $\text{Ly}\alpha$ nebulae is shown in Table 5.3. While the $\text{Ly}\alpha/\text{HeII}$ ratios are comparable, other than the $\text{CIII]}/\text{HeII}$ ratio on Night 2, all the metal line ratios from this source are at the low end or lower than the range seen in EELRs. Furthermore, this source shows very different line ratios than those seen in another large radio-quiet $\text{Ly}\alpha$ nebula at $z \approx 2.7$ (Dey et al., 2005).

In order to gain greater insight into the metallicity and possible ionization sources for the nebula, we used `CLOUDY`⁴ to model simple, constant density gas clouds being illuminated by AGN, Pop III, and Pop II SEDs and predict the resulting line ratios and continuum emission. The AGN template is taken from Mathews & Ferland (1987) ($F_\nu \propto \nu^{-1.0}$ at $26 < h\nu < 56$ eV, $F_\nu \propto \nu^{-3.0}$ at $56 < h\nu < 365$ eV), and the Pop III spectra are Tumlinson et al. (2006) 1 Myr models ($Z = 0$, a top-heavy IMF peaked around $10M_\odot$ with $\sigma=1.0$, i.e., their case A). The Pop II case is a 1 Myr, $Z = 0.001$, Salpeter IMF, instantaneous burst model from Starburst 99 (Leitherer et al., 1996).

⁴Calculations were performed with version 07.02.02 of `CLOUDY`, last described by Ferland et al. (1998).

Table 5.3. Emission Line Ratio Comparison

	$\text{Ly}\alpha/\text{HeII}^{\text{a}}$	CIV/HeII	$\text{CIII]}/\text{HeII}$	$\text{CIV}/\text{CIII]}$	Reference
Radio Galaxy Halos (Composite)	11.7	1.75	0.73	2.4	Humphrey et al. 2008 ^b
Radio Galaxy Halos (Mean)	9.80 ± 5.69	1.59 ± 0.56	1.06 ± 1.05	2.22 ± 1.17	Humphrey et al. 2008
Stacked Ly α Blobs at $z \approx 3$	11.11 ± 9.88	-	-	-	Saito et al. 2008
Ly α Blob at $z \approx 2.7$	7.62 ± 0.08	1.02 ± 0.01	0.12 ± 0.02	8.34 ± 1.67	Dey et al. 2005
PRG1 Night 1	8.00 ± 2.32	$< 0.22^{\text{c}}$	$< 0.19^{\text{c}}$	-	This study
PRG1 Night 2	7.59 ± 1.43	0.36 ± 0.20	0.83 ± 0.20	0.44 ± 0.24	This study

^aNo correction has been applied for $\text{Ly}\alpha$ absorption.

^bErrors on line ratios from composite spectrum not given.

^c 1σ upper limits.

The strong, spatially extended $\text{Ly}\alpha$ +HeII emission and weak, spatially variable CIII] and CIV emission in our discovery spectra and the blue, spatially extended continuum emission measured from deep broad-band imaging provide constraints on the metallicity of the gas and on the slope of the ionizing continuum in the system. He^+ and C^{+3} have similar ionization potentials (54.4 eV and 47.9 eV, respectively), so a comparison of HeII and CIV puts constraints on the metallicity that are less dependent on the ionizing continuum slope. The $\text{Ly}\alpha$ and CIII] emission lines (relevant ionization potentials of H and C^{+2} : 13.6 eV and 24.4 eV) provide additional constraints on the slope of the ionizing continuum.

The observed lines will also depend on the ionization parameter of the system. A very rough estimate based on our discovery data is $U = \phi(H)/(n_H c) \gtrsim 0.0002$, where $\phi(H)=Q(H)/(\pi R^2)$ is the surface flux of ionizing photons, n_H is the total

hydrogen gas density, and R is the radius of the cloud. We have assumed our observed quantities: $Q(\text{H})=4.9 \times 10^{54}$ photons s^{-1} , $n_{\text{H}} \sim n_{\text{e}} \sim 29.7 \text{ cm}^{-3}$, and $R \approx 28 \text{ kpc}$. However, this estimate is uncertain and most likely a lower limit. We have argued that the $\text{Ly}\alpha$ flux is likely underestimated and raised the possibility that the system is density-bounded, both of which will cause an underestimate of the ionizing photon flux (possibly by an order of magnitude). In addition, the geometry of the system is clearly complex, and the estimated density depends critically on the assumed value of the filling factor. The density estimates in Section 4.1 are larger than typical values for the ISM ($n_{\text{H}} \sim 1 \text{ cm}^{-3}$); if the cloud is in fact more similar to typical ISM densities, the ionization parameter would increase by over an order of magnitude. A more sophisticated treatment of the ionization parameter is beyond the scope of this analysis, so for the purposes of this paper we modeled a reasonable range of ionization parameters: $\text{Log } U = [-3, -1, 0]$.

5.4.3 Metallicity of the Gas

In order to explore the range of parameter space allowed by our observations, in Figure 5.7 we plot line diagnostics for models with a range of ionization parameters, metallicities, and ionizing SEDs, comparing them to our observed limits on the line ratios of the nebulosity from Night 1 and Night 2.

For low ionization parameters ($\text{Log } U < -1$), it is possible to produce the observed line ratios with an AGN spectral energy distribution (SED) illuminating solar metallicity gas (Figure 5.7; blue plus signs). For higher ionization parameter ($\text{Log } U \geq -1$), the observed ratios require low metallicity gas. In the case of an AGN SED, the CIV/HeII and CIII]/HeII limits imply $Z < 10^{-2} Z_{\odot}$. Models with Pop III ionization lead to lower metallicity estimates of $Z < 10^{-3} Z_{\odot}$. (For the Pop II model even lower metallicities would be required, but this case is

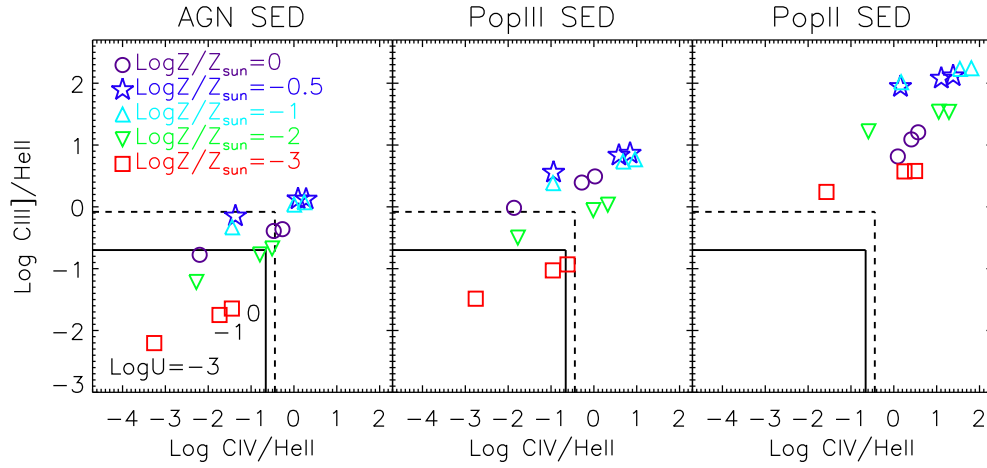


Figure 5.7 $\text{C III]}/\text{He II}$ vs. $\text{C IV}/\text{He II}$ line ratios for a grid of `Cloudy` models over a range of SEDs, ionization parameters, and gas metallicities. The models represent a cloud of gas with $\text{Log} Z/Z_{\odot} = [-3, -2, -1, -0.5, 0]$ being ionized with an ionization parameter of $\text{Log} U = [-3, -1, 0]$ by one of three SEDs: an AGN SED (left), a Tumlinson et al. (2006) Population III galaxy model SED (middle; $Z=0$, 1 Myr burst, moderately top-heavy IMF discussed in the text), and a Starburst99 Population II galaxy model SED (right; $Z=0.001$, Salpeter IMF, 1 Myr burst; Leitherer et al., 1996). The 1σ limits on the line ratios of the nebulosity are shown for Night 1 (solid line) and Night 2 (dashed line).

highly unlikely given the large $Q(\text{He}^+)/Q(\text{H})$ ratio, as discussed in Section 4.1.) To put this into context, these metallicity estimates are at or below the lowest limits for weak Mg II absorbers at $0.4 < z < 2.4$ ($>10^{-2}$ - $10^{-2.5}$; Lynch & Charlton, 2007). Studies of the most metal-poor damped Ly α absorbers have shown that none have metallicities lower than $[Fe/H] > -3$ (Pettini et al., 2008). Ly α forest clouds at $z \approx 3$ with $N(\text{HI}) > 10^{15} \text{ cm}^{-2}$ are uniformly metal-enriched with carbon abundances of $\approx 10^{-2} Z_{\odot}$, and observations of lower column density Ly α forest clouds indicate that there may be universal minimum metallicity of $3.5 \times 10^{-4} Z_{\odot}$ that is roughly constant from $z \approx 2 - 6$ (Songaila, 2001). If the metallicity of PRG1 is similar to the lowest metallicities measured from absorption-line studies, this would be the first time such a system has been seen in Ly α and HeII emission. As another comparison, Fosbury et al. (2003) have suggested that the emission line ratios observed in the Lynx Arc indicate a nebula of metallicity $Z/Z_{\odot} \approx 0.04$ ionized by an extremely low metallicity star cluster (see also Binette et al., 2003). The HeII/Ly α line ratio is 3.7 times smaller and the C IV,C III]/HeII line ratios nearly 30 times larger in the Lynx Arc than in PRG1.

While the weak metal line emission suggests a low metallicity system, the metallicity estimates are uncertain due to a variety of factors, none of which are well-constrained by the current data, e.g., the ionization parameter, the geometry of the cloud and ionizing source(s), and the intensity and spectrum of the source(s) of ionization. Putting stronger constraints on the metallicity of the nebula will require deeper spectroscopy and more detailed photoionization modeling, which is beyond the scope of the current paper.

5.4.4 Source of Ionization

The large HeII equivalent width and large HeII/Ly α ratio is strong evidence that the nebula is powered by a hard ionizing continuum. We discuss each of the possible ionization sources in turn: AGN, shock ionization, W-R stars, low metallicity (Pop II) and zero metallicity (Pop III) star formation, and gravitational cooling radiation.

5.4.4.1 AGN

An AGN can produce high HeII/Ly α ratios and weaker C IV and C III] emission lines, particularly if it is illuminating a low metallicity cloud. This scenario is certainly plausible, as emission line halos (e.g., Ly α , C III], HeII, C IV) around radio galaxies have been known for some time, arising predominantly from a combination of jet-ISM interactions and scattered light from the AGN or from spatially extended star formation (e.g., McCarthy et al., 1987; van Ojik et al., 1996; Dey et al., 1997; Villar-Martín et al., 2003; Reuland et al., 2003). Unlike our Ly α +HeII nebula, however, these gaseous haloes are predominantly metal-enriched, with strong C III] and C IV emission (e.g., Reuland et al., 2007; Maxfield et al., 2002).

While there is no compact source visible in the center of the nebula, there are several compact sources in the vicinity of the nebula that could in principle harbor an AGN (Figure 5.1). For two reasons we believe that if there is an AGN in the system, it must be at the position of Source A. First, we find that even if all the nearby sources were AGN, Source A would contribute the vast majority of the ionizing photon flux. When we scale the standard quasar template from Elvis et al. (1994) to match the measured B_W flux from each source and calculate the corresponding ionizing photon flux, the net contribution is only 2% of the

ionizing photon flux required to explain the $\text{Ly}\alpha$, with nearly all of that arising from Source A. Second, in Section 3.2 we argued that the metal line emission is not cospatial with the $\text{Ly}\alpha+\text{HeII}$ nebula, and that the observed metal lines likely derive from the region of Source A. Below we discuss the likelihood that an AGN at the position of Source A is powering the $\text{Ly}\alpha+\text{HeII}$ nebula.

If we assume that the Night 2 metal line emission stems primarily from Source A, we can compare the measured line ratios to those of well-studied galaxy populations. At face value, the CIII] and CIV emission lines associated with the region around Source A are suggestive of an AGN, however we find that the line ratios are more consistent with that seen in non-AGN Lyman Break Galaxies (LBGs, Shapley et al., 2003). The measured ratios of $\text{CIV}/\text{Ly}\alpha=0.05\pm0.03$ and $\text{CIII]}/\text{Ly}\alpha=0.11\pm0.02$ (uncorrected for $\text{Ly}\alpha$ absorption) are likely upper limits due to the uncertainties in the $\text{Ly}\alpha$ measurement. Even so, the $\text{CIV}/\text{Ly}\alpha$ ratio is a factor of 4-5 lower than what is seen in LBGs flagged as narrow-line AGNs ($\text{CIV}/\text{Ly}\alpha\approx0.25$; Shapley et al., 2003) and in local Seyfert galaxies ($\text{CIV}/\text{Ly}\alpha\approx0.21$; Ferland & Osterbrock, 1986). In addition, if $\text{Ly}\alpha$ is underestimated by a factor of 2, the corrected $\text{CIV}/\text{Ly}\alpha$ and $\text{CIII]}/\text{Ly}\alpha$ ratios would match those of non-AGN LBGs. Furthermore, the ratio of $\text{CIII]}/\text{CIV}=2.3\pm1.2$ is in agreement with that found for non-AGN LBGs ($\text{CIII]}/\text{CIV}\approx2.5$; Shapley et al., 2003) and is a factor of 4 higher than expected from a narrow-line AGN spectrum ($\text{CIII]}/\text{CIV}\approx0.05$; Shapley et al., 2003), suggesting Source A has a softer ionizing continuum.

There is currently no evidence from the multi-wavelength SED that Source A is an AGN. Existing X-ray coverage of the field reveals no X-ray detection at the position of the system ($F_X > 1.5\times10^{-14} \text{ erg s}^{-1} \text{ cm}^{-2}$ or $L_X > 2.7\times10^{44} \text{ erg s}^{-1}$, 2-7 keV observed; Kenter et al., 2005) but is too shallow to rule out lower luminosity

Seyfert galaxies. The typical luminosities of Seyfert galaxies: $L_{Ly\alpha} = 10^{42} - 2 \times 10^{44}$ erg s⁻¹ and L_X (0.5-4.5 keV) = $5 \times 10^{42} - 10^{45}$ erg s⁻¹, with $L_{Ly\alpha}/L_X$ ratios of $\sim 0.1 - 2$ (Kriss, 1984). If we combine the $L_{Ly\alpha}/L_X$ ratio as an upper limit (since the ratio for an extended nebula will be smaller due to the smaller covering fraction of the gas) with our measured Ly α luminosity (5.4×10^{43} erg s⁻¹), we should expect L_X (0.5-4.5 keV) $> 2.7 \times 10^{43} - 5.4 \times 10^{44}$ erg s⁻¹, which is at or below our current X-ray detection threshold.

The optical and mid-infrared (MIR) photometric measurements for Source A are listed in Table 5.2. We measured the broad-band optical fluxes of Source A from NDWFS using 2.1'' diameter apertures and applied aperture corrections of [1.06, 1.40, 1.07] in the B_W , R , and I bands. The Source A IRAC photometry comes from SDWFS (3.5'' diameter aperture with point source aperture corrections of [1.38, 1.38, 1.38, 1.42]). The IRAC colors of Source A lie outside the AGN color-color selection regions of Stern et al. (2005) and Lacy et al. (2004), and the probability that an X-ray AGN will have these IRAC colors is small (Gorjian et al., 2008). The IRAC colors of Source A are $[3.6] - [4.5] = 0.52 \pm 0.03$ (Vega) and $[5.8] - [8.0] = 0.131 \pm 0.11$ (Vega) (in "Region B" of Figure 4 of Gorjian et al., 2008). The percentage of X-ray sources down to the XBoötes limit with IRAC colors in this region is 4%. In a small portion of the survey with 10 times deeper X-ray coverage, the distribution of sources in IRAC color-color space is similar, i.e., there are very few X-ray sources with the IRAC colors of Source A (Gorjian et al., 2008). In contrast, these IRAC colors are consistent with star-forming galaxies at $z = 1.25 - 1.75$ (Donley et al., 2008), the redshift range of our source. Similarly, the IRAC SED of Source A shows the 1.6 μ m bump rather than the power-law typical of obscured AGN (Alonso-Herrero et al., 2006), indicating that the MIR SED

is dominated by stellar emission. All of the other sources in the vicinity show similar non-power-law SEDs.

PRG1 is also undetected at longer wavelengths: the MIPS 24 μm non-detection corresponds to an upper limit of 51 μJy (1σ), and the Westerbork 20 cm survey non-detection yields a 5σ limit at 3 GHz in the rest-frame of $6.4 \times 10^{23} \text{ W Hz}^{-1}$ (de Vries et al., 2002), well below the realm of high redshift radio galaxies ($\sim 10^{26} \text{ W Hz}^{-1}$; Seymour et al., 2007).

On the other hand, the energetics of the nebula suggest that an AGN at the projected position of Source A could explain the observed continuum emission if the AGN is highly obscured to our line of sight. If we make the assumption that an AGN at Source A is powering the HeII emission, we can estimate the amount of B_W continuum emission we expect from the nebula due to illumination by the AGN. Scaling a standard AGN template (Elvis et al., 1994) to match the ionizing photon flux implied by the HeII ($Q(\text{He}^+) \approx 6.2 \times 10^{53} \text{ photons s}^{-1}$), we estimate that the B_W luminosity from the AGN striking the cloud should be $L_{B_W, \text{incident}} \approx 1.9 \times 10^{41} \text{ erg s}^{-1} \text{ \AA}^{-1}$. This incident AGN continuum flux — the maximum possible contribution from the AGN to the observed continuum emission — is roughly the same as the measured B_W continuum emission from the nebula ($L_{B_W, \text{nebula}} \approx 1.1 \times 10^{41} \text{ erg s}^{-1} \text{ \AA}^{-1}$). In reality, the continuum observed within the nebula will arise solely from two-photon (2γ) continuum and scattering of AGN light with no contribution directly from the AGN itself. Given the predicted HeII equivalent width from our `CLOUDY` models of AGN illumination, we estimate the expected B_W 2γ continuum within the nebula to be $L_{B_W, 2\gamma} \approx 2.0 \times 10^{40} \text{ erg s}^{-1}$, roughly 18% of the observed B_W continuum of the nebula. Electron scattering of AGN light is expected to have a scattering op-

tical depth of $\tau = n_e l \sigma_T = 0.1-1.1$, where $n_e \approx 1-10 \text{ cm}^{-3}$ and $l = 56 \text{ kpc}$ is the approximate path through the nebula, corresponding to a Thompson scattering continuum of $L_{B_W, \text{Thompson}} \lesssim 1.9 \times 10^{41} \text{ erg s}^{-1} \text{ \AA}^{-1} \times (1 - e^{-\tau}) = 1.3 \times 10^{41} \text{ erg s}^{-1} \text{ \AA}^{-1}$, comparable to the observed B_W continuum emission. Although dust scattering, which is much more efficient than Thompson scattering, may contribute as well, large quantities of dust would be difficult to reconcile with the large observed $\text{Ly}\alpha$ and HeII luminosities. Questions remain, but given the limitations of our discovery data it appears that an AGN at the position of Source A that is unobscured along the line-of-sight to the nebula, but completely hidden from our viewpoint, could explain the observed B_W continuum emission. Correcting for the maximal (since we are assuming the projected separation) solid angle subtended by the cloud as seen from Source A ($d\Omega \approx 3.1 \text{ srs}$), we find that the minimum intrinsic AGN luminosity needed to produce this incident flux is $L_{B_W, \text{min(AGN)}} \gtrsim 1.9 \times 10^{41} \text{ erg s}^{-1} \times 4\pi/d\Omega \text{ erg s}^{-1} \text{ \AA}^{-1} \approx 7.6 \times 10^{41} \text{ erg s}^{-1} \times \text{\AA}^{-1}$. Source A has a B_W luminosity of $1.8 \times 10^{40} \text{ erg s}^{-1} \times \text{\AA}^{-1}$, which is over an order of magnitude fainter than this firm lower limit. The AGN would therefore need to be very highly obscured along our line-of-sight to match the existing observational constraints.

In conclusion, an AGN at the position of Source A is a plausible source of the hard ionizing radiation. However, there is no visible AGN in the vicinity of the nebula, so it would have to be highly obscured along our line of sight. An AGN in the vicinity of the nebula must be in a radio-quiet phase and so highly obscured that even the observed MIR SED is dominated by light from the host galaxy. Deep optical and near-infrared spatially resolved spectroscopy will be required to resolve this issue.

5.4.4.2 Shocks

The observed ratios are inconsistent with shock ionization in solar metallicity gas, which typically produces much higher C III]/He II and C IV/C III] ratios (e.g., ~ 3 -25 and ~ 1 -10 for shock velocities of 500-150 km s⁻¹; Dopita & Sutherland, 1996) along with strong NV λ 1240. Stronger shock velocities are inconsistent with the narrow width of the He II line ($v_{FWHM} \lesssim 500$ km s⁻¹).

5.4.4.3 Wolf-Rayet Stars

Strong He II emission is seen in both of the major classes of W-R stars (nitrogen dominant WN stars and carbon dominant WC stars), but it is accompanied by strong Si IV, NV, and/or other metal emission lines. WN stars show strong Si IV $\lambda\lambda$ 1393,1402 relative to He II, C IV, and C III], which we can rule out with our discovery spectra. WC stars usually show C IV/C III] ratios greater than 1, medium-strength Si IV, and a large number of other metal lines (e.g., Fe), all of which are inconsistent with our observations. The spectrum of a typical ‘W-R galaxy’ (a galaxy with spectrum dominated by W-R features) effectively averages over hundreds or thousands of W-R stars, but none the less typically shows Si IV, C IV, He II, and NV emission with P Cygni profiles due to the effects of strong stellar winds (e.g., Leitherer et al., 1996). The composite LBG spectrum measured at $z \sim 3$ also shows Si IV and C IV with P Cygni profiles from the stellar winds of massive stars, as well as broad He II ($v_{FWHM} \sim 1500$ km s⁻¹), which the authors argue is most likely due to the fast, dense winds of W-R stars (Shapley et al., 2003). In our case, the narrow width of the He II line ($v_{FWHM} \lesssim 500$ km s⁻¹) and the absence of other important W-R features (e.g., Si IV, NV) rules out the idea that the He II emission is coming from W-R stars.

5.4.4.4 Population II Star Formation

The existence of diffuse, blue continuum that is cospatial with the Ly α and HeII line emission (Figure 5.1) is suggestive of a distributed source of ionization such as spatially extended star formation. However, the observed HeII/Ly α line ratio is inconsistent with ionization by a standard Population II SED (e.g., $Z = 0.001 = 1/20Z_{\odot}$). The expected $Q(\text{He}^+)/Q(\text{H})$ ratio for a Pop II model is several orders of magnitude lower than observed (Schaerer, 2003). Predictions from our `CLOUDY` models indicate that the dearth of hard ionizing photons translates into negligible HeII emission and HeII/Ly α ratios that are a factor of 1000 lower than observed. Furthermore, the large observed HeII equivalent width can only be produced by very low metallicity stellar populations (Schaerer, 2003).

5.4.4.5 Population III Star Formation

The only way to explain strong HeII emission with ionization from a stellar population is to invoke very young ages and very low metallicities. The rest-frame equivalent width (EW) of Ly α ($\text{EW} \approx 294 \text{\AA}$) is higher than or comparable to what is expected from solar metallicity and Pop II stellar populations (Schaerer, 2003), but it is by no means the largest observed in Ly α -emitting galaxy surveys ($\text{EW}_{\text{max}} \gtrsim 300 \text{\AA}$; Dawson et al., 2007). The measured equivalent width of HeII, however, is very large ($\text{EW} \approx 37 \text{\AA}$) in the context of stellar populations and only consistent with the youngest ($\lesssim 2 \text{ Myr}$) and lowest metallicity stars ($\lesssim 10^{-7} Z_{\odot}$), in the absence of mass loss (Schaerer, 2003). Here, we chose a Pop III model with a moderately top-heavy IMF from Tumlinson et al. (2006) that has a peak at $10 M_{\odot}$ (their case A); a more top-heavy IMF will tend to boost the HeII/Ly α ratio due to the additional hard ionizing photons. The ionizing photon flux implied by the

Ly α and HeII measurements from PRG1 implies a Pop III cluster mass of 13-100 $\times 10^6 M_{\odot}$ and a B_W continuum flux of $L_{B_W,incident} \approx 1.7 \times 10^{41} \text{ erg s}^{-1} \text{ \AA}^{-1}$, roughly equal to the observed continuum ($L_{B_W,nebula} \approx 1.1 \times 10^{41} \text{ erg s}^{-1} \text{ \AA}^{-1}$). In comparing with our `CLOUDY` models, however, we find that the observed HeII/Ly α ratio (≈ 0.12) is much higher than expected from our Pop III model (≈ 0.004). However, it is important to keep in mind that model uncertainties, such as the assumed IMF and the effects of mass loss, could have a large effect on the predicted line luminosities. In addition, the possible underestimation of the Ly α flux discussed in Section 4.1 as well as a density-bounded geometry will tend to boost the observed HeII/Ly α ratio.

On the face of it, it would be surprising to find such low metallicity star formation at such a low redshift. However, we cannot conclusively rule out the Pop III scenario on this basis alone. While the mean metallicity of the universe increases with time, several theoretical models of Pop III star formation have suggested that significant metallicity inhomogeneities may exist even at low redshifts (Tornatore et al., 2007). These models predict that while the metallicity is quickly enriched at the center of collapsed structures, low metallicity regions can persist on the periphery over longer timescales, allowing Pop III star formation to proceed well after the epoch of reionization (Tornatore et al., 2007; Scannapieco et al., 2003). At $z \approx 2.3$ (roughly the redshift midpoint of our Ly α nebula survey), Tornatore et al. (2007) predict a Pop III SFR density of $1.3 \times 10^{-7} M_{\odot} \text{ yr}^{-1} \text{ Mpc}^{-3}$. If we were to assume that this Ly α +HeII nebula is powered by very low metallicity star formation, use the Ly α line emission (extrapolated to the entire nebula and corrected for absorption) to estimate a SFR ($\text{SFR} = L_{Ly\alpha} / 1.26 \times 10^{42} \approx 5.4 \times 10^{43} / 1.26 \times 10^{42} \text{ erg s}^{-1} \approx 42.9 M_{\odot} \text{ yr}^{-1}$; Kennicutt, 1998), and ignore any

incompleteness of our survey, we would calculate that one nebula of this kind within our survey volume ($1.3 \times 10^8 \text{ Mpc}^3$), corresponds to a Pop III SFR density of $\sim 3.3 \times 10^{-7} M_{\odot} \text{ yr}^{-1} \text{ Mpc}^{-3}$. This very rough estimate based on a single source is of the same order of magnitude as the model predictions (within a factor of 3) despite the large theoretical uncertainties in the conditions regulating Pop III star formation and intergalactic medium (IGM) enrichment at all redshifts.

In reality, the amount of low metallicity gas and Pop III star formation as a function of redshift will depend on the efficiency of star formation in different environments and the efficiency with which stars pollute their environment, i.e., the feedback efficiency. A more realistic treatment of galactic winds in cosmological simulations (e.g., momentum-driven winds; Oppenheimer & Davé, 2006) is shown to suppress the metallicity in all gas phases relative to the constant wind scenario similar to that used in Tornatore et al. (2007), which may in turn increase the fraction of Pop III star formation at any given redshift. On the other hand, only a few stellar generations would be required to produce the mass of carbon in the nebula. Assuming the derived ionized gas mass ($\sim 8 \times 10^8 M_{\odot}$), the simulated yields for Pop III supernovae ($\sim 0.2\text{--}1 M_{\odot} \text{ C}$ per $20\text{--}40 M_{\odot}$ supernova progenitor; Tominaga et al., 2007) and instantaneous mixing, enriching the cloud to $z \approx 10^{-3} Z_{\odot}$ would only require of order 750 supernovae ($2 - 4 \times 10^4 M_{\odot}$). This is several orders of magnitude lower than the fraction of the cluster mass implied by the $\text{Ly}\alpha$ and HeII luminosities that is in stars with $M > 20 M_{\odot}$ for the assumed top-heavy IMF: $f(M > 20 M_{\odot}) = 0.26$ or $3 - 27 \times 10^6 M_{\odot}$. Thus it is likely the nebula would be polluted to the observed levels over a relatively short timescale.

Large uncertainties remain in our understanding of Pop III star formation. The expected fraction of Pop III star formation at a give epoch is unclear, feed-

back efficiency of these first stars is largely unconstrained, and there are a wide range of possible $\text{Ly}\alpha/\text{HeII}$ ratios, depending on stellar mass loss, star formation history, and the complicated effects of $\text{Ly}\alpha$ radiative transfer. Despite the strong $\text{Ly}\alpha+\text{HeII}$ signature in this source, we cannot conclusively confirm or rule out Pop III star formation as a source of ionization with the current observations.

5.4.4.6 Gravitational Cooling Radiation

A number of theoretical papers have addressed the issue of gravitational cooling radiation, i.e., the cooling of gas as it collapses within the dark matter potential and heats to $T \approx 10^4$ K. Metal-line cooling is possible for gas with $T < 10^4$ K, but it is ~ 1000 times less efficient than cooling via $\text{Ly}\alpha$ emission, unless $Z > 0.1Z_{\odot}$ (Haiman et al., 2000). Thus for low metallicity gas, strong $\text{Ly}\alpha$ emission is expected to dominate the cooling (Fardal et al., 2001). HeII emission may be important as well, but its contribution relative to $\text{Ly}\alpha$ is unclear due to uncertainties in how much $\text{Ly}\alpha$ will escape the system. From a semi-analytic calculation assuming monolithic collapse, Haiman et al. (2000) suggested that a cloud that is sufficiently metal-poor will radiate 10% of the energy via $\text{HeII}\lambda 304\text{\AA}$; this corresponds to a $\text{HeII}\lambda 1640/\text{Ly}\alpha$ of ~ 0.01 , where we have followed Yang et al. (2006) and adopted a ratio of $\text{HeII}\lambda 1640/\text{HeII}\lambda 304} \approx 0.10$, i.e., the case B values of Storey & Hummer (1995) extrapolated to the low density limit. Using Parallel TreeSPH simulations, Yang et al. (2006) predicted ratios of $\text{HeII}\lambda 1640/\text{Ly}\alpha \lesssim 0.10 - 0.001$ for gravitationally cooling clouds, depending on the degree to which self-shielding of the gas reduces the $\text{Ly}\alpha$ flux. This range approaches the observed ratio for PRG1, but due to subsequent corrections to the treatment of star-forming gas in more recent simulations the predictions from Yang et al. (2006) are likely overestimates (Y. Yang 2008, private communication). Thus, the observed

HeII/Ly α ratio appears to be higher than predicted for gravitational cooling radiation, but again the uncertainties in both the theoretical predictions and in our Ly α measurement make it difficult to draw firm conclusions.

Some of the theoretical predictions for gravitationally cooling clouds are consistent with our observations. The observed HeII line width ($\sigma_v < 250 \text{ km s}^{-1}$) is more consistent with gravitational cooling radiation ($\sigma_v < 400 \text{ km s}^{-1}$; e.g., Yang et al., 2006) than with outflows. In addition, theoretical simulations of the redshift evolution predict a peak in the number density of gravitational cooling Ly α nebulae at $z \approx 2$, consistent with our discovery of a Ly α +HeII nebula at $z \approx 1.7$. While Dijkstra (2009) predicts rest-frame Ly α equivalent widths of $>1000 \text{ \AA}$ for gravitationally cooling clouds, he notes that the observed rest-frame equivalent width is likely to be reduced by a factor of 5-10 due to scattering of Ly α photons in the IGM, more in line with our measurements.

However, a number of other theoretical predictions of gravitational cooling radiation do not fit our observations. First, the simulations do not reproduce the relative sizes of the observed Ly α and HeII regions. Fardal et al. (2001) could not reproduce the sizes of the largest observed Ly α nebulae unless they invoked resonant scattering of the Ly α emission. In that case, the HeII emission should be more centrally-concentrated than the Ly α . Similarly, Yang et al. (2006) suggested that HeII regions would likely be too small to resolve with current observational facilities. In contrast, in our Ly α +HeII nebula the HeII region appears to be comparable in size to the Ly α region ($\approx 45 \text{ kpc}$). The theoretical papers also predict that Ly α nebulae will only be present as a halo around a massive galaxy (Fardal et al., 2001; Furlanetto et al., 2005). While there are a few faint sources around the edge of our nebula, and there may be unresolved low surface brightness clumps

within the cloud, the multi-wavelength imaging shows no evidence for a central massive galaxy in this system.

Given the uncertainties in the theoretical predictions and the limits of our discovery data it is difficult to assess the applicability of the gravitational cooling model. The weight of the current evidence disfavors gravitational cooling as the sole explanation for the line emission, but it is certainly possible that the nebula is powered by multiple processes, with gravitational cooling radiation playing a larger role on the outskirts and photoionization from stars or AGN dominating the ionization of the central regions.

5.5 Implications

Strong $\text{Ly}\alpha + \text{HeII}$ in the absence of strong metal lines has been championed as a unique observational signature of primordial galaxy formation (e.g., Pop III star formation or gravitationally cooling clouds), but the discovery of this $\text{Ly}\alpha + \text{HeII}$ nebula suggests that the situation can be much more complex in actual astrophysical sources. Occam's razor suggests that the most likely power source is an AGN at the position of Source A. An analysis of the existing data shows no obvious evidence of a powerful AGN in the vicinity, so to explain the ionization of the nebula, an AGN would need to be highly obscured even in the mid-infrared. The line ratios rule out ionization by shocks, W-R stars, and Pop II star formation. Pop III star formation would provide the necessary hard ionizing continuum to explain the observed line ratios along with a natural explanation for the spatially extended continuum emission, but this scenario appears unlikely given the low redshift. Despite the compelling $\text{Ly}\alpha + \text{HeII}$ signature, the complexity of this source and the large uncertainties in theoretical predictions preclude a more

definitive conclusion. The contribution from gravitational cooling radiation is similarly unclear, although the morphology of the nebula (with no central compact source) and relative sizes of the $\text{Ly}\alpha$ and HeII emitting regions disfavor this hypothesis as a dominant mechanism.

One of the most important implications of this discovery is that it demonstrates that we must be careful when using strong $\text{Ly}\alpha+\text{HeII}$ emission as a tracer of Pop III star formation. Surveys looking specifically for this $\text{Ly}\alpha+\text{HeII}$ signature are ongoing. While the low redshift of PRG1 allows for the detailed multi-wavelength follow-up necessary in order to understand the power source and the metallicity of the gas, the same cannot be said for ongoing $\text{Ly}\alpha+\text{HeII}$ emitter surveys at higher redshift that will lack longer wavelength coverage and be sensitivity challenged. It is extremely important to note that if this $\text{Ly}\alpha+\text{HeII}$ had been discovered at high redshift, it would have been easy to jump prematurely to the Pop III conclusion. The discovery of a $\text{Ly}\alpha+\text{HeII}$ nebula at $z \approx 1.67$ therefore provides an ideal opportunity to evaluate the extent to which strong $\text{Ly}\alpha+\text{HeII}$ emission can be used as a unique tracer of Pop III star formation and underscores the importance of using care when interpreting a strong $\text{Ly}\alpha+\text{HeII}$ signature in the absence of more extensive multi-wavelength data.

5.6 Conclusions

We have discovered a $\text{Ly}\alpha$ nebula at $z \approx 1.67$ (the lowest redshift $\text{Ly}\alpha$ nebula known) that shows strong, diffuse HeII emission and weak/negligible $\text{CIII}]$ and CIV emission. From the line ratios we derive evidence that this nebula may contain low metallicity ($Z < 10^{-2} - 10^{-3} Z_{\odot}$) gas, depending on the unknown ionization parameter, that is being illuminated by a hard ionizing continuum, either

due to an AGN or a very low metallicity stellar population (Pop III), by gravitational cooling, or some combination thereof. The softer continua of Pop I and II stars can be conclusively ruled out along with ionization by shocks and W-R stars. No obvious, unobscured, powerful AGN is seen in the system; thus if an AGN is responsible, it must be highly obscured along our line of sight. Despite the strong $\text{Ly}\alpha + \text{HeII}$ signature, our detailed analysis of the discovery data shows that dedicated follow-up observations will be required in order to draw firm conclusions about the dominant source of ionization for the nebula and better constrain the metallicity. This is the first time that the predicted observational signature of very low metallicity (Pop III) star formation — strong $\text{Ly}\alpha$ and HeII in the absence of strong metal lines — has been seen in a spatially extended source; however, the complex nature of the nebula and the fact that such complexity becomes increasingly difficult to discern with redshift suggest that studies at high redshift will need to use caution when interpreting future $\text{Ly}\alpha + \text{HeII}$ discoveries.

CHAPTER 6

CONCLUSIONS AND FUTURE DIRECTIONS

This thesis addresses the space density, large scale environment, and physical properties of large $\text{Ly}\alpha$ nebulae. In this final chapter, we summarize the main findings and discuss future directions for this work.

6.1 The Space Density of Large $\text{Ly}\alpha$ Nebulae

If $\text{Ly}\alpha$ nebulae represent a dramatic phase of massive galaxy formation, measuring the space density of $\text{Ly}\alpha$ nebulae tells us about the frequency with which these massive systems are forming. The very rarity of $\text{Ly}\alpha$ nebulae has made measuring the space density of $\text{Ly}\alpha$ nebulae in a systematic way a significant challenge due to the observational expense of wide-area narrow-band surveys. In Chapter 2, we presented a systematic search for large $\text{Ly}\alpha$ nebulae built on deep broad-band data. The technique is sensitive to the largest and brightest $\text{Ly}\alpha$ nebulae and is able to probe enormous comoving volumes using existing datasets. Our 9 square degree survey area over a redshift range of $z \approx 1.6 - 2.9$ — the largest $\text{Ly}\alpha$ nebula survey to date — recovered 1 previously known case and discovered 4 new $\text{Ly}\alpha$ nebulae. The brightest 4 $\text{Ly}\alpha$ nebulae have $\text{Ly}\alpha$ luminosities of $\sim 2 - 12 \times 10^{43} \text{ erg s}^{-1}$ and sizes $> 60 \text{ kpc}$. The results of this search provide the first strong lower limit on the $\text{Ly}\alpha$ nebula number density of $\approx 1.9 \times 10^{-7} h_{70}^3 \text{ Mpc}^{-3}$, a number density is comparable to that of $\sim 10^{14} M_{\odot}$ halos.

Our survey is complementary to the systematic $\text{Ly}\alpha$ nebula surveys carried out using narrow-band filters at $z \approx 2.3 - 6.5$. These surveys are unbiased in terms of $\text{Ly}\alpha$ morphology and probe to fainter luminosities and smaller sizes

(Saito et al., 2006; Smith & Jarvis, 2007; Ouchi et al., 2008; Yang et al., 2009), but they cover significantly smaller volumes ($10^6 - 10^7 h_{70}^{-3} \text{ Mpc}^3$). The number density estimates from these surveys ($1.2 \times 10^{-6} - 6.7 \times 10^{-6} h_{70}^3 \text{ Mpc}^{-3}$ for sources with $L_{\text{Ly}\alpha} > 1.5 \times 10^{43} \text{ erg s}^{-1}$) are roughly an order of magnitude larger than our result. The discrepancy likely stems from three sources. First, our survey is not sensitive to Ly α nebulae with morphologies dominated by a bright, central source, a morphology which may describe roughly half to two-thirds of Ly α nebulae. This estimate is highly uncertain, and at the same time it is unclear that Ly α nebulae with strong central, continuum sources should be grouped together with the diffuse Ly α nebulae found by our search. Second, due to cosmic variance, smaller volume surveys may overestimate the number density if they happen to land upon an overdense structure. The uncertainty due to cosmic variance in narrow-band surveys may be as much as a factor of 2 – 3. Finally, the measurement of Ly α sizes and total luminosities from our survey involves scaling from broad-band filter measurements and will tend to underestimate the actual Ly α properties. Our number density estimate therefore corresponds to a somewhat larger and more luminous set of Ly α nebulae, which would be expected to be rarer, than those found by the systematic narrow-band surveys

Ultimately, we need to understand whether Ly α nebulae represent a ubiquitous phase experienced by these most massive halos or whether they are merely a curiosity. Putting independent constraints on the mass of the overdense structures hosting Ly α nebulae will allow estimates of the duty cycle or filling factor appropriate for these sources. Future Ly α nebula surveys will also be crucial for providing larger samples these rare sources and for refining the estimate of the space density. A question that has only begun to be addressed is the evolution

of the $\text{Ly}\alpha$ nebulae with redshift. Zirm et al. (2009) find a strong decrease in the total luminosity of $\text{Ly}\alpha$ halos around radio galaxies from $z \approx 2$ to $z \approx 1$, possibly due to gas depletion and specific star formation rate around the massive central galaxy. Keel et al. (2009) carried out a survey of the outer regions of two clusters and found no $\text{Ly}\alpha$ nebulae, which they argue shows that the $\text{Ly}\alpha$ nebulae number density evolves at least as strongly as $(1 + z)^3$. We note, however, that our space density measurements at $z \approx 2 - 3$ are comparable to the upper limit of Keel et al. (2009), which suggests that the fall off in $\text{Ly}\alpha$ nebulae may not be as dramatic as it first appeared.

A key advantage of the broad-band approach is the ease with which we can apply our survey technique to other archival survey datasets. While traditional $\text{Ly}\alpha$ nebula surveys require devoted narrow-band observing time in addition to spectroscopic follow-up, our approach can be adapted to any wide-area deep (5σ depth of ~ 26 mag) broad-band dataset with U or B coverage, such as the CFHT Legacy Survey which achieved a 5σ depth of $u = 28.7$ mag over 4 square degrees and $u = 26.4$ mag over 170 square degrees. The technique could also be adapted to GALEX deep and all-sky surveys in order to search for $\text{Ly}\alpha$ nebulae at somewhat lower redshift ($z \approx 1.2 - 2.3$). Farther in the future, deep broad-band all-sky data will be coming online from surveys such as Pan-STARRS, with 5σ point source depth of 29.4 mag over several years¹, and LSST, which promises a depth of $r = 27.5$ mag over the 10 year lifetime of the program (Ivezic et al., 2008).

¹<http://pan-starrs.ifa.hawaii.edu/public/design-features/wide-field.html>

6.2 The Environments of Large $\text{Ly}\alpha$ Nebulae

The earliest examples of large $\text{Ly}\alpha$ nebulae were found in targeted narrow-band surveys of the neighborhood of quasars and galaxy overdensities (Francis et al., 1996; Keel et al., 1999; Steidel et al., 2000). The $\text{Ly}\alpha$ nebulae in these regions were found in portions of the field with a high density of $\text{Ly}\alpha$ -emitting galaxies, and the first blank-field survey uncovered no large $\text{Ly}\alpha$ nebulae. It was natural, therefore, to suspect that $\text{Ly}\alpha$ nebulae are a phenomenon of very dense environments, but the connection was by no means proven. The discovery of a large $\text{Ly}\alpha$ nebula at $z \approx 2.7$ due to its strong mid-infrared emission rather than via a targeted narrow-band survey provided a unique opportunity to test the association between these rare sources and galaxy overdensities in an unbiased manner. Chapter 3 presents a deep $\text{Ly}\alpha$ imaging of the environment surrounding this $\text{Ly}\alpha$ nebula. We identified 785 LAE candidates and found evidence for a factor of ~ 3 LAE overdensity spanning 20×50 Mpc (comoving). We ruled out a chance coincidence of the $\text{Ly}\alpha$ nebula and the overdense structure at the $\lesssim 1\%$ level. These results point conclusively to a strong association between the largest $\text{Ly}\alpha$ nebulae and overdense regions of the Universe.

Ours is the second survey to map out the large scale environment of a $\text{Ly}\alpha$ nebula and the first targeting a $\text{Ly}\alpha$ nebula that was found independent of its environment. The overdense structure is comparable to what was found in the vicinity of the well-known Steidel et al. (2000) $\text{Ly}\alpha$ nebula pair (Matsuda et al., 2005). Independent evidence is also mounting that $\text{Ly}\alpha$ nebulae are a highly clustered population. The pair of $\text{Ly}\alpha$ nebulae at $z \approx 3.1$ are separated by only 1.4 Mpc (Steidel et al., 2000), and out of 4 $\text{Ly}\alpha$ nebulae discovered within a 5 square degree systematic narrow-band survey (Yang et al., 2009), 2 were located

only 550 kpc apart and at nearly identical redshifts. Clustering estimates strongly suggest that these two Ly α nebulae must reside within the same dark matter halo, i.e., a massive proto-group or cluster (Yang et al., 2009).

The ultimate goal is to understand the large scale three-dimensional environment of Ly α nebulae. Since the original study, we have expanded our survey of the large scale environment to cover a full square degree using the Subaru telescope and SuprimeCam. By obtaining spectroscopic confirmation of the brighter Ly α -emitting galaxy candidates in the vicinity, we will be able to map out the large-scale environment of the Ly α nebula out to ~ 100 Mpc scales and probe the kinematics within this overdense region. This survey will provide observational constraints on these large filamentary structures by mapping out the full three dimensional environment of the overdensity that hosts this large Ly α nebula. As the Ly α nebula class appears to be fairly heterogeneous in its properties, further environmental studies of other Ly α nebulae will be needed to test whether all Ly α nebulae are confined to overdense regions.

6.3 The Anatomy of Large Ly α Nebulae

Ly α nebulae are highly complex systems. In Chapter 4 we used HST/ACS and NICMOS observations to map out the local environment of a large Ly α nebulae. We found that there are at least 8 compact galaxies within the system, and confirmed that a strong MIPS $24\mu\text{m}$ source, likely an obscured AGN, is offset by 21 (projected) kpc from the peak of the Ly α emission. The Ly α emission itself is smooth, showing no knots or high surface brightness clumps of emission, effectively ruling out the presence of compact ionizing sources of $M \gtrsim 10^8 M_\odot$ within the Ly α cloud. A HeII-emitting region discovered from ground-based

spectroscopy was found to be spatially extended by $0.8\text{--}1''$ (6–8 kpc). The system also contains a diffuse continuum component coincident with the diffuse HeII and $\text{Ly}\alpha$ emission, which suggests a spatially extended source of ionization or scattering processes. In terms of energetics, the galaxies in the system are a negligible contribution to the ionizing photon flux within the system, and previous work showed that the measured flux of the AGN is not powerful enough to ionize more than 20% of the nebula. The detection of a diffuse, rest-frame UV continuum component may be due to scattered light from the AGN or it may suggest a contribution from in situ young stars. The ionization of the nebula is likely dominated either by an AGN that is obscured to the line of sight but directed towards the cloud or by contributions from both the AGN and a spatially extended stellar population.

A lot of work remains to be done to understand the detailed energetics of this $\text{Ly}\alpha$ nebula and $\text{Ly}\alpha$ nebulae in general. In the case studied here, better measurements are needed on the color of the diffuse continuum using HST, and radio and submillimeter measurements are needed to constrain the peak of the SED and the size of the emitting region. More broadly, it remains unclear at this point whether the $\text{Ly}\alpha$ nebula class is in fact defined by a common ionization mechanism or whether we have thus far lumped together a heterogeneous mix of AGN, star formation, and cooling radiation powered cases. Only four other $\text{Ly}\alpha$ nebulae have been studied in as much multiwavelength detail; while the conclusions have ranged from AGN-powering to cooling radiation, it is not clear that other possibilities have been conclusively ruled out. In detailed follow-up, the $\text{Ly}\alpha$ nebula pair found by Steidel et al. (2000) were shown to be diverse in terms of the dominant ionization source. The first shows no X-ray detection but strong

submillimeter emission and is likely an obscured starburst; the second shows X-ray emission and is likely an AGN (Chapman et al., 2001, 2004; Basu-Zych & Scharf, 2004; Geach et al., 2007). In the case of the $\text{Ly}\alpha$ nebula found by Francis et al. (2001) at $z \approx 2.4$, the power source is assumed to be the AGN due to the detection of C IV, and the $\text{Ly}\alpha$ is smooth and not resolved into discrete clumps. Smith et al. (2008) argue they can rule out the AGN and star formation possibilities for a $\text{Ly}\alpha$ nebula at $z \approx 2.8$, which leaves only gravitational cooling as a viable scenario. (Geach et al., 2009) find that at least 20% of $\text{Ly}\alpha$ nebulae have detected X-ray counterparts implying that a large fraction of $\text{Ly}\alpha$ nebulae are associated with obscured AGN that are capable of powering the $\text{Ly}\alpha$ emission. Given the complexity of $\text{Ly}\alpha$ nebulae, we caution that the lack of evidence for an AGN is not conclusive proof of its absence and the presence of an AGN does not guarantee that it dominates the energetics. Developing a larger sample of well-studied $\text{Ly}\alpha$ nebulae will be important for determining the fraction of cases that fall into each category. The AGN hypothesis will always be the most straight-forward scenario and the one which is most difficult to rule out due to the possibility of highly non-isotropic obscuration, so it will be important to obtain deep observations even in cases without obvious AGN signatures.

Finally, we must come back to the question of how $\text{Ly}\alpha$ nebulae relate to the $\text{Ly}\alpha$ halos found around many radio galaxies. Other than the lack of radio emission and the absence of a central massive galaxy, these systems are strikingly similar in size and total $\text{Ly}\alpha$ luminosity (e.g., Villar-Martín, 2007; Hatch et al., 2008). Perhaps $\text{Ly}\alpha$ nebulae are an earlier or related phase of the same phenomenon, possibly occurring during a period of low or extinguished AGN activity. Much depends on understanding the processes that regulates the activ-

ity and radio emission in AGN. Deep radio observations of Ly α nebulae capable of detecting faint radio emission would bridge the gap between these two very similar populations.

6.4 The Physical Conditions within Large Ly α Nebulae

The internal complexity of Ly α nebulae makes it difficult to determine conclusively whether the Ly α emission is powered primarily by obscured AGN, spatially-extended star formation, starburst-driven superwinds, or gravitational cooling (e.g., Dey et al. (2005); Nilsson et al. (2006); Matsuda et al. (2007)). Determining the dominant source of ionization requires detailed analysis of the spectra of Ly α nebulae to disentangle the physical conditions within these regions. In Chapter 5, we report on a Ly α nebula at $z \approx 1.67$, the lowest redshift Ly α nebula known. This Ly α nebula is distinguished by strong, diffuse HeII emission and weak/negligible CIII] and CIV emission, a spectral signature long associated with primordial galaxy formation processes (Pop III stars or gravitational cooling radiation). Photoionization modeling shows that while the line ratios provide evidence that this nebula contains low metallicity ($Z < 10^{-2} - 10^{-3} Z_{\odot}$) gas, comparable to the lowest metallicities observed in damped Ly α absorbers (Pettini et al., 2008), the conclusion depends on the unknown ionization parameter. We can conclusively rule out the softer continua of Pop I and II stars along with ionization by shocks and W-R stars, but is more difficult to determine what is powering the nebula. The line ratios are strong evidence that the Ly α nebula is being illuminated by a hard ionizing continuum, either an AGN or a very low metallicity stellar population (Pop III), or that it is powered by gravitational cooling. Since no obvious, unobscured, powerful AGN is detected in the system,

an AGN would have to be highly obscured along our line of sight. Despite the strong $\text{Ly}\alpha + \text{HeII}$ signature, our detailed analysis of the discovery data shows large uncertainties about dominant source of ionization for the nebula and the metallicity. Improving on this work will require deep optical and near-infrared spectroscopy.

A fundamental question that has yet to be answered about $\text{Ly}\alpha$ nebulae is whether the surrounding gas is infalling, outflowing, or in rotation about the system. The answer bears directly on the starburst-driven superwind and cooling radiation models for powering the $\text{Ly}\alpha$ emission. However, understanding the kinematics using $\text{Ly}\alpha$ is a notoriously difficult challenge due to complex radiative transfer effects. For example, kinematic studies of a large $\text{Ly}\alpha$ nebula at $z \approx 3.1$ yielded completely different answers about the presence of infall versus outflow in the system (Wilman et al., 2005; Dijkstra et al., 2006b). Despite the disadvantages of $\text{Ly}\alpha$, in these high redshift $\text{Ly}\alpha$ nebulae, few alternatives are available. Targeting the new lower redshift $\text{Ly}\alpha$ nebulae ($z \approx [1.7, 1.9, 2.3, 2.5, 2.7]$) discovered as part of this thesis with deep, spatially-resolved spectroscopy will allow studies of the kinematics of $\text{Ly}\alpha$ nebulae using multiple kinematic tracers less prone to radiative transfer effects (e.g., HeII , $[\text{OII}]$, $[\text{OIII}]$, and $\text{H}\alpha$).

Equally important for determining the source of ionization is a detailed understanding of the physical conditions within $\text{Ly}\alpha$ nebulae. The $\text{Ly}\alpha$ nebula studied in Chapter 5 underscores the difficulty of conclusively identifying the source of ionization and physical conditions with shallow or incomplete data. It also raises a more general question about whether $\text{Ly}\alpha$ nebulae are regions of low metallicity, e.g., due to infalling pristine gas. Investigating whether other $\text{Ly}\alpha$ nebulae show hard line ratios, e.g. strong HeII relative to metal lines, and

performing more detailed photoionization modeling will be important for understanding this issue. Deep optical and near-infrared spectroscopy of the lower redshift Ly α nebulae discovered here provide an ideal opportunity to take advantage of reduced surface brightness dimming as well as shock and photoionization line diagnostics unavailable at higher redshifts to put strong constraints on the metallicity, temperature, and dust obscuration within these systems.

6.5 Ly α Nebulae and Galaxy Formation

Ly α nebulae show strong evidence of being sites of ongoing galaxy formation in the high redshift universe. To take advantage of these laboratories of galaxy formation, the next generation of Ly α nebula searches must cover enormous volumes in order to build up reasonable sample sizes. Measuring the kinematics will be important in assessing the relationship between individual components seen in Ly α nebulae. When analyzing the energetics of Ly α nebulae, moving beyond circumstantial arguments will require deep spectroscopy and more detailed photoionization modeling. It also will require taking a more sophisticated approach to the question of dust, as the common argument that the presence of strong Ly α rules out a dusty environment is clearly too simplistic in complex systems where strong submillimeter and mid-infrared sources are seen in close proximity to copious Ly α emission. Finally, understanding the connection between Ly α nebulae and radio galaxy systems may hold the key to understanding what this rare, energetic phenomenon is telling us about the process of massive galaxy formation.

APPENDIX A

WAVELET DECOMPOSITION

Searching for diffuse, spatially extended sources a challenge due to the fact that standard astronomical image contains object spanning a large range of sizes and brightnesses. A standard approach is to convolve the image with a filter of the appropriate size in order to accentuate features on a given scale. However, this method is ill-equipped to handle the very common situation in which objects of very different size are overlapping or in close proximity to each other. The basic idea behind wavelet decomposition is to decompose the image into a set of “wavelet planes”, each of which contains the flux of sources with power on that scale and the sum of which is the original image (ignoring losses). The power of the wavelet decomposition approach is to reduces the interference of small scale objects when looking for large scale structures.

The wavelet decomposition code used in this work — *wvdecomp* — was written by Alexey Vikhlinin as part of the *ZHTOOLS* package ¹. Here we give a brief description of the algorithm; a detailed discussion of the code is given in *ZHTOOLS* documentation. The *wvdecomp* algorithm uses an *à trous* wavelet kernel which is defined as the difference between two functions (f_i and f_{i+1}) that each roughly resemble a Gaussian of width 2^{i-1} . On each scale, the kernel is sensitive to objects of the same size ($\approx 2^{i-1}$).

The algorithm begins by convolving the image with the smallest wavelet kernel. Any features that are insignificant in the convolved image are zeroed and the result is subtracted from the original image. The majority of the flux from small

¹ZHTOOLS documentation and source code: <http://heawww.harvard.edu/RDzhtools>.

features comparable in size to the smallest wavelet kernel have therefore been removed. The process is repeated with larger and larger wavelet kernels, and the results from each step are saved as wavelet power maps or “wavelet planes.” To minimize the loss of information at each step, two thresholds are specified in running the code: a detection threshold, t_{max} , and a filtering threshold, t_{min} , both defined in terms of the image noise. A source detected on a given scale above t_{min} is counted as significant only if the source local maximum also exceeds t_{max} .

REFERENCES

- Adelberger, K. L., Steidel, C. C., Pettini, M., Shapley, A. E., Reddy, N. A., & Erb, D. K. 2005, *ApJ*, 619, 697
- Alonso-Herrero, A., et al. 2006, *ApJ*, 640, 167
- Antonucci, R. 1993, *ARA&A*, 31, 473
- Ashby, M. L. N., et al. 2009, arXiv:0906.0024
- Atek, H., Kunth, D., Hayes, M., Östlin, G., & Mas-Hesse, J. M. 2008, *A&A*, 488, 491
- Atek, H., Kunth, D., Schaerer, D., Hayes, M., Deharveng, J.-M., Ostlin, G., & Mas-Hesse, J. M. 2009, arXiv:0906.5349
- Basu-Zych, A., & Scharf, C. 2004, *ApJL*, 615, L85
- Baum, S. A., & Heckman, T. 1989, *ApJ*, 336, 702
- Bertin, E., & Arnouts, S. 1996, *A&AS*, 117, 393
- Binette, L., Groves, B., Villar-Martín, M., Fosbury, R. A. E., & Axon, D. J. 2003, *A&A*, 405, 975
- Blanc, G. A., et al. 2008, *ApJ*, 681, 1099
- Boroson, T. A., & Oke, J. B. 1982, *Nature*, 296, 397
- Bower, R. G., Benson, A. J., Malbon, R., Helly, J. C., Frenk, C. S., Baugh, C. M., Cole, S., & Lacey, C. G. 2006, *MNRAS*, 370, 645

- Bromm, V., Kudritzki, R. P., & Loeb, A. 2001, *ApJ*, 552, 464
- Brown, M. J. I., Dey, A., Jannuzi, B. T., Brand, K., Benson, A. J., Brodwin, M., Croton, D. J., & Eisenhardt, P. R. 2007, *ApJ*, 654, 858
- Bruzual, G., & Charlot, S. 2003, *MNRAS*, 344, 1000
- Bundy, K., Ellis, R. S., & Conselice, C. J. 2005, *ApJ*, 625, 621
- Calzetti, D., Kinney, A. L., & Storchi-Bergmann, T. 1994, *ApJ*, 429, 582
- Chambers, K. C., & Miley, G. K. 1990, *Evolution of the Universe of Galaxies*, 10, 373
- Chapman, S. C., Lewis, G. F., Scott, D., Richards, E., Borys, C., Steidel, C. C., Adelberger, K. L., & Shapley, A. E. 2001, *ApJL*, 548, L17
- Chapman, S. C., Scott, D., Windhorst, R. A., Frayer, D. T., Borys, C., Lewis, G. F., & Ivison, R. J. 2004, *ApJ*, 606, 85
- Charlot, S., & Fall, S. M. 1993, *ApJ*, 415, 580
- Colbert, J. W., Teplitz, H., Francis, P., Palunas, P., Williger, G. M., & Woodgate, B. 2006, *ApJL*, 637, L89
- Cowie, L. L., & Hu, E. M. 1998, *AJ*, 115, 1319
- Curtis, H. D. 1917, *PASP*, 29, 206
- Daddi, E., Cimatti, A., Renzini, A., Fontana, A., Mignoli, M., Pozzetti, L., Tozzi, P., & Zamorani, G. 2004, *ApJ*, 617, 746
- Daddi, E., et al. 2005, *ApJ*, 626, 680

- Davis, M., & Wilkinson, D. T. 1974, *ApJ*, 192, 251
- Dawson, S., et al. 2004, *ApJ*, 617, 707
- Dawson, S., Rhoads, J. E., Malhotra, S., Stern, D., Wang, J., Dey, A., Spinrad, H., & Jannuzi, B. T. 2007, *ApJ*, 671, 1227
- Dey, A., van Breugel, W., Vacca, W. D., & Antonucci, R. 1997, *ApJ*, 490, 698
- Dey, A., Spinrad, H., Stern, D., Graham, J. R., & Chaffee, F. H. 1998, *ApJL*, 498, L93
- Dey, A., et al. 2005, *ApJ*, 629, 654
- Dey, A., et al. 2008, *ApJ*, 677, 943
- Dijkstra, M., Haiman, Z., & Spaans, M. 2006, *ApJ*, 649, 14
- Dijkstra, M., Haiman, Z., & Spaans, M. 2006, *ApJ*, 649, 37
- Dijkstra, M. 2009, *ApJ*, 690, 82
- di Serego Alighieri, S., Kurk, J., Ciardi, B., Cimatti, A., Daddi, E., & Ferrara, A. 2008, *IAU Symposium*, 255, 75
- Djorgovski, S., Spinrad, H., McCarthy, P., & Strauss, M. A. 1985, *ApJL*, 299, L1
- Donley, J. L., Rieke, G. H., Pérez-González, P. G., & Barro, G. 2008, *ApJ*, 687, 111
- Dopita, M. A., & Sutherland, R. S. 1996, *ApJS*, 102, 161
- de Vries, W. H., Morganti, R., Röttgering, H. J. A., Vermeulen, R., van Breugel, W., Rengelink, R., & Jarvis, M. J. 2002, *AJ*, 123, 1784

- Eisenhardt, P. R., et al. 2004, *ApJS*, 154, 48
- Elston, R., Rieke, G. H., & Rieke, M. J. 1988, *ApJL*, 331, L77
- Elvis, M., et al. 1994, *ApJS*, 95, 1
- Ezer, D., & Cameron, A. G. W. 1971, *Ap&SS*, 14, 399
- Fardal, M. A., Katz, N., Gardner, J. P., Hernquist, L., Weinberg, D. H., & Davé, R. 2001, *ApJ*, 562, 605
- Ferland, G. J., & Osterbrock, D. E. 1986, *ApJ*, 300, 658
- Ferland, G. J., Korista, K. T., Verner, D. A., Ferguson, J. W., Kingdon, J. B., & Verner, E. M. 1998, *PASP*, 110, 761
- Finkelstein, S. L., Rhoads, J. E., Malhotra, S., Pirzkal, N., & Wang, J. 2007, *ApJ*, 660, 1023
- Finkelstein, S. L., Rhoads, J. E., Malhotra, S., Grogan, N., & Wang, J. 2008, *ApJ*, 678, 655
- Fosbury, R. A. E., et al. 2003, *ApJ*, 596, 797
- Francis, P. J., et al. 1996, *ApJ*, 457, 490
- Francis, P. J., et al. 2001, *ApJ*, 554, 1001
- Furlanetto, S. R., Schaye, J., Springel, V., & Hernquist, L. 2005, *ApJ*, 622, 7
- Gawiser, E., et al. 2007, *ApJ*, 671, 278
- Geach, J. E., Smail, I., Chapman, S. C., Alexander, D. M., Blain, A. W., Stott, J. P., & Ivison, R. J. 2007, *ApJL*, 655, L9

- Geach, J. E., et al. 2009, *ApJ*, 700, 1
- Giavalisco, M. 2002, *ARA&A*, 40, 579
- Gorjian, V., et al. 2008, *ApJ*, 679, 1040
- Greve, T. R., Stern, D., Ivison, R. J., De Breuck, C., Kovács, A., & Bertoldi, F. 2007, *MNRAS*, 382, 48
- Gronwall, C., et al. 2007, *ApJ*, 667, 79
- Guhathakurta, P., Tyson, J. A., & Majewski, S. R. 1990, *ApJL*, 357, L9
- Haberzettl et al. 2007, *A&A*, in press (astro-ph/0701797)
- Haiman, Z., Spaans, M., & Quataert, E. 2000, *ApJL*, 537, L5
- Hansen, M., & Oh, S. P. 2006, *MNRAS*, 367, 979
- Hatch, N. A., Overzier, R. A., Röttgering, H. J. A., Kurk, J. D., & Miley, G. K. 2008, *MNRAS*, 383, 931
- Hatch, N. A., Overzier, R. A., Kurk, J. D., Miley, G. K., Röttgering, H. J. A., & Zirm, A. W. 2009, *MNRAS*, 395, 114
- Hayashino, T., et al. 2004, *AJ*, 128, 2073
- Hayes, M., Östlin, G., Mas-Hesse, J. M., Kunth, D., Leitherer, C., & Petrosian, A. 2005, *A&A*, 438, 71
- Hayes, M., Östlin, G., Atek, H., Kunth, D., Mas-Hesse, J. M., Leitherer, C., Jiménez-Bailón, E., & Adamo, A. 2007, *MNRAS*, 382, 1465

- Heckman, T. M., Baum, S. A., van Breugel, W. J. M., & McCarthy, P. 1989, *ApJ*, 338, 48
- Henry, A. L., Malkan, M. A., Colbert, J. W., Siana, B., Teplitz, H. I.
- Hu, E. M., & Cowie, L. L. 1987, *ApJL*, 317, L7
- Hu, E. M., & McMahon, R. G. 1996, *Nature*, 382, 231
- Hu, E. M., Cowie, L. L., & McMahon, R. G. 1998, *ApJL*, 502, L99
- Hubble, E. P. 1926, *ApJ*, 63, 236
- Hubble, E. P. 1929, *ApJ*, 69, 103
- Hughes, D., & Dunlop, J. 1998, *Observational Cosmology with the New Radio Surveys*, 226, 259
- Humphrey, A., Villar-Martín, M., Vernet, J., Fosbury, R., di Serego Alighieri, S., & Binette, L. 2008, *MNRAS*, 383, 11
- Ivezic, Z., et al. 2008, *arXiv:0805.2366*
- Jannuzi, B. T., & Dey, A. 1999, in *ASP Conf. Ser. 191, Photometric Redshifts and the Detection of High Redshift Galaxies*, ed. R. Weymann et al. (San Francisco: ASP), 111
- Shimasaku, K., Ouchi, M., Furusawa, H., Yoshida, M., Kashikawa, N., & Okamura, S. 2005, *PASJ*, 57, 447
- Keel, W. C., Cohen, S. H., Windhorst, R. A., & Waddington, I. 1999, *AJ*, 118, 2547

- Keel, W. C., White, R. E., III., Chapman, S., & Windhorst, R. A. 2009, arXiv:0907.2201
- Kennicutt, R. C., Jr. 1998, *ApJ*, 498, 541
- Kenter, A., et al. 2005, *ApJS*, 161, 9
- Kewley, L. J., Geller, M. J., & Jansen, R. A. 2004, *AJ*, 127, 2002
- Koo, D. C., & Kron, R. T. 1980, *PASP*, 92, 537
- Kriss, G. A. 1984, *ApJ*, 277, 495
- Lacy, M., et al. 2004, *ApJS*, 154, 166
- Lai, K., et al. 2008, *ApJ*, 674, 70
- Leitherer, C., Vacca, W. D., Conti, P. S., Filippenko, A. V., Robert, C., & Sargent, W. L. W. 1996, *ApJ*, 465, 717
- Loeb, A., & Rybicki, G. B. 1999, *ApJ*, 524, 527
- Lowenthal, J. D., Hogan, C. J., Leach, R. W., Schmidt, G. D., & Foltz, C. B. 1990, *ApJ*, 357, 3
- Lowenthal, J. D., Hogan, C. J., Green, R. F., Caulet, A., Woodgate, B. E., Brown, L., & Foltz, C. B. 1991, *ApJL*, 377, L73
- Ly, C., et al. 2009, *ApJ*, 697, 1410
- Lynch, R. S., & Charlton, J. C. 2007, *ApJ*, 666, 64
- Madau 1995, *ApJ*, 441, 18

- Malhotra, S., & Rhoads, J. E. 2002, *ApJL*, 565, L71
- Marín-Franch, A., & Aparicio, A. 2003, *ApJ*, 594, 63
- Martin, D. C., et al. 2005, *ApJL*, 619, L1
- Mas-Hesse, J. M., Kunth, D., Tenorio-Tagle, G., Leitherer, C., Terlevich, R. J., & Terlevich, E. 2003, *ApJ*, 598, 858
- Mathews, W. G., & Ferland, G. J. 1987, *ApJ*, 323, 456
- Matsuda, Y., et al. 2004, *AJ*, 128, 569
- Matsuda, Y., et al. 2005, *ApJ*, 634, 125
- Matsuda, Y., Iono, D., Ohta, K., Yamada, T., Kawabe, R., Hayashino, T., Peck, A. B., & Petitpas, G. R. 2007, *ApJ*, 667, 667
- Maxfield, L., Spinrad, H., Stern, D., Dey, A., & Dickinson, M. 2002, *AJ*, 123, 2321
- McBride, J., Fakhouri, O., & Ma, C.-P. 2009, *arXiv:0902.3659*
- McCarthy, P. J., Spinrad, H., Djorgovski, S., Strauss, M. A., van Breugel, W., & Liebert, J. 1987, *ApJL*, 319, L39
- McCarthy, P. J. 1993, *ARA&A*, 31, 639
- McCarthy, P. J., Baum, S. A., & Spinrad, H. 1996, *ApJS*, 106, 281
- Metcalf, N., Shanks, T., Campos, A., McCracken, H. J., & Fong, R. 2001, *MNRAS*, 323, 795
- McCarthy, P. J., et al. 2004, *ApJL*, 614, L9

- Miley, G., & De Breuck, C. 2008, *A&A Rev.*, 15, 67
- Miyazaki, S., et al. 2002, *PASJ*, 54, 833
- Mori, M., Umemura, M., & Ferrara, A. 2004, *ApJL*, 613, L97
- Moustakas, J., Kennicutt, R. C., Jr., & Tremonti, C. A. 2006, *ApJ*, 642, 775
- Nagao, T., Motohara, K., Maiolino, R., Marconi, A., Taniguchi, Y., Aoki, K., Ajiki, M., & Shioya, Y. 2005, *ApJL*, 631, L5
- Nagao, T., et al. 2008, *ApJ*, 680, 100
- Neufeld, D. A. 1991, *ApJL*, 370, L85
- Nilsson, K. K., Fynbo, J. P. U., Møller, P., Sommer-Larsen, J., & Ledoux, C. 2006, *A&A*, 452, L23
- Ohyama, Y., et al. 2003, *ApJL*, 591, L9
- Oke, J. B. 1974, *ApJS*, 27, 21 i
- Opik, E. 1922, *ApJ*, 55, 406
- Oppenheimer, B. D., & Davé, R. 2006, *MNRAS*, 373, 1265
- Osterbrock, D. E. 1989, Research supported by the University of California, John Simon Guggenheim Memorial Foundation, University of Minnesota, et al. (Mill Valley, CA, University Science Books), 422 pp.
- Ouchi, M., et al. 2004, *ApJ*, 611, 660
- Ouchi, M., et al. 2008, *ApJS*, 176, 301

- Ouchi, M., et al. 2008, *ApJS*, 176, 301
- Ouchi, M., et al. 2009, *ApJ*, 696, 1164
- Overzier, R. A., et al. 2008, *ApJ*, 673, 143
- Palunas, P., Teplitz, H. I., Francis, P. J., Williger, G. M., & Woodgate, B. E. 2004, *ApJ*, 602, 545
- Partridge, R. B., & Peebles, P. J. E. 1967, *ApJ*, 147, 868
- Partridge, R. B., & Peebles, P. J. E. 1967, *ApJ*, 148, 377
- Partridge, R. B. 1974, *ApJ*, 192, 241
- Peng, C. Y., Ho, L. C., Impey, C. D., & Rix, H.-W. 2002, *AJ*, 124, 266
- Pentericci, L., Roettgering, H. J. A., Miley, G. K., Carilli, C. L., & McCarthy, P. 1997, *A&A*, 326, 580
- Pentericci, L., Röttgering, H. J. A., Miley, G. K., McCarthy, P., Spinrad, H., van Breugel, W. J. M., & Macchetto, F. 1999, *A&A*, 341, 329
- Pettini, M., Zych, B. J., Steidel, C. C., & Chaffee, F. H. 2008, *MNRAS*, 385, 2011
- Prescott, M. K. M., Kashikawa, N., Dey, A., & Matsuda, Y. 2008, *ApJL*, 678, L77
- Prescott, M. K. M., Dey, A., & Jannuzi, B. T. 2009, *ApJ*, 702, 554
- Reddy, N. A., Steidel, C. C., Pettini, M., Adelberger, K. L., Shapley, A. E., Erb, D. K., & Dickinson, M. 2008, *ApJS*, 175, 48
- Reuland, M., et al. 2003, *ApJ*, 592, 755

- Reuland, M., et al. 2007, *AJ*, 133, 2607
- Rhoads, J. E., et al. 2003, *AJ*, 125, 1006
- Saito, T., Shimasaku, K., Okamura, S., Ouchi, M., Akiyama, M., & Yoshida, M. 2006, *ApJ*, 648, 54
- Rybicki, G. B., & Loeb, A. 1999, *ApJL*, 520, L79
- Saito, T., Shimasaku, K., Okamura, S., Ouchi, M., Akiyama, M., Yoshida, M., & Ueda, Y. 2008, *ApJ*, 675, 1076
- Scannapieco, E., Schneider, R., & Ferrara, A. 2003, *ApJ*, 589, 35
- Schaerer, D. 2002, *A&A*, 382, 28
- Schaerer, D. 2003, *A&A*, 397, 527
- Schaerer, D. 2008, *IAU Symposium*, 255, 66
- Schmidt, M. 1963, *Nature*, 197, 1040
- Schneider, D. P., Gunn, J. E., Turner, E. L., Lawrence, C.
- Seymour, N., et al. 2007, *ApJS*, 171, 353
- Shapley, A. E., Steidel, C. C., Pettini, M., & Adelberger, K. L. 2003, *ApJ*, 588, 65
- Shimasaku, K., et al. 2006, *PASJ*, 58, 313
- Smail, I., Ivison, R. J., & Blain, A. W. 1997, *ApJL*, 490, L5
- Smith, D. J. B., & Jarvis, M. J. 2007, *MNRAS*, 378, L49

- Smith, D. J. B., Jarvis, M. J., Lacy, M., & Martínez-Sansigre, A. 2008, *MNRAS*, 389, 799
- Songaila, A. 2001, *ApJL*, 561, L153
- Spinrad, H., Filippenko, A. V., Wyckoff, S., Stocke, J. T., Wagner, R. M., & Lawrie, D. G. 1985, *ApJL*, 299, L7
- Spitzer, L. 1978, *Physical processes in the interstellar medium*, SAO/NASA ADS Astronomy Abstract Service (New York; Wiley-Interscience), 333 pp.
- Springel, V., et al. 2005, *Nature*, 435, 629
- Stark, D. P., Ellis, R. S., Richard, J., Kneib, J.-P., Smith, G. P., & Santos, M. R. 2007, *ApJ*, 663, 10
- Stark, D. P., Ellis, R. S., Bunker, A., Bundy, K., Targett, T., Benson, A., & Lacy, M. 2009, *ApJ*, 697, 1493
- Steidel, C. C., Sargent, W. L. W., & Dickinson, M. 1991, *AJ*, 101, 1187
- Steidel, C. C., Pettini, M., & Hamilton, D. 1995, *AJ*, 110, 2519
- Steidel, C. C., Giavalisco, M., Pettini, M., Dickinson, M., & Adelberger, K. L. 1996, *ApJL*, 462, L17
- Steidel, C. C., Adelberger, K. L., Shapley, A. E., Pettini, M., Dickinson, M., & Giavalisco, M. 2000, *ApJ*, 532, 170
- Stern, D., & Spinrad, H. 1999, *PASP*, 111, 1475
- Stern, D., et al. 2005, *ApJ*, 631, 163

- Storey, P. J., & Hummer, D. G. 1995, MNRAS, 272, 41
- Taniguchi, Y., & Shioya, Y. 2000, ApJL, 532, L13
- Taniguchi, Y., Shioya, Y., & Kakazu, Y. 2001, ApJL, 562, L15
- Thommes, E., Meisenheimer, K., Fockenbrock, R., Hippelein, H., Roeser, H.-J., & Beckwith, S. 1998, MNRAS, 293, L6
- Tominaga, N., Umeda, H., & Nomoto, K. 2007, ApJ, 660, 516
- Tornatore, L., Borgani, S., Dolag, K., & Matteucci, F. 2007, MNRAS, 382, 1050
- Tremonti, C. A., et al. 2004, ApJ, 613, 898
- Trenti, M., & Stiavelli, M. 2008, ApJ, 676, 767
- Tumlinson, J., Giroux, M. L., & Shull, J. M. 2001, ApJL, 550, L1
- Tumlinson, J. et al. 2006, ApJ, 641, 1
- van Breugel, W., De Breuck, C., Stanford, S. A., Stern, D., Röttgering, H., & Miley, G. 1999, ApJL, 518, L61
- van Dokkum, P. G., et al. 2004, ApJ, 611, 703
- van Ojik, R., Roettgering, H. J. A., Carilli, C. L., Miley, G. K., Bremer, M. N., & Macchetto, F. 1996, A&A, 313, 25
- Venemans, B. P., et al. 2007, A&A, 461, 823
- Verhamme, A., Schaerer, D., & Maselli, A. 2006, A&A, 460, 397

- Villar-Martín, M., Vernet, J., di Serego Alighieri, S., Fosbury, R., Humphrey, A., Pentericci, L., & Cohen, M. 2003, *New Astron. Rev.*, 47, 291
- Villar-Martín, M. 2007, *New Astronomy Review*, 51, 194
- White, S. D. M., & Rees, M. J. 1978, *MNRAS*, 183, 341
- Wilman, R. J., Gerksen, J., Bower, R. G., Morris, S. L., Bacon, R., de Zeeuw, P. T., & Davies, R. L. 2005, *Nature*, 436, 227
- Yagi, M., Kashikawa, N., Sekiguchi, M., Doi, M., Yasuda, N., Shimasaku, K., & Okamura, S. 2002, *AJ*, 123, 66
- Yang, Y., Zabludoff, A. I., Davé, R., Eisenstein, D. J., Pinto, P. A., Katz, N., Weinberg, D. H., & Barton, E. J. 2006, *ApJ*, 640, 539
- Yang, Y., Zabludoff, A., Tremonti, C., Eisenstein, D., & Davé, R. 2009, *ApJ*, 693, 1579
- Zirm, A. W., et al. 2005, *ApJ*, 630, 68
- Zirm, A. W., Dey, A., Dickinson, M., & Norman, C. J. 2009, *ApJL*, 694, L31